


8-2011

## Raman Spectroscopic Study of Solid Solution Spinel Oxides

Brian D. Hosterman  
University of Nevada, Las Vegas

Follow this and additional works at: <https://digitalscholarship.unlv.edu/thesesdissertations>

 Part of the [Condensed Matter Physics Commons](#), [Materials Science and Engineering Commons](#), and the [Mineral Physics Commons](#)

---

### Repository Citation

Hosterman, Brian D., "Raman Spectroscopic Study of Solid Solution Spinel Oxides" (2011). *UNLV Theses, Dissertations, Professional Papers, and Capstones*. 1087.  
<https://digitalscholarship.unlv.edu/thesesdissertations/1087>

This Dissertation is protected by copyright and/or related rights. It has been brought to you by Digital Scholarship@UNLV with permission from the rights-holder(s). You are free to use this Dissertation in any way that is permitted by the copyright and related rights legislation that applies to your use. For other uses you need to obtain permission from the rights-holder(s) directly, unless additional rights are indicated by a Creative Commons license in the record and/or on the work itself.

This Dissertation has been accepted for inclusion in UNLV Theses, Dissertations, Professional Papers, and Capstones by an authorized administrator of Digital Scholarship@UNLV. For more information, please contact [digitalscholarship@unlv.edu](mailto:digitalscholarship@unlv.edu).

RAMAN SPECTROSCOPIC STUDY OF SOLID SOLUTION SPINEL OXIDES

by

Brian D. Hosterman

Bachelor of Science  
Denison University  
2001

Master of Science  
University of Nevada, Las Vegas  
2006

A dissertation submitted in partial fulfillment  
of the requirements for the

**Doctor of Philosophy in Physics**  
**Department of Physics**  
**College of Sciences**

**Graduate College**  
**University of Nevada, Las Vegas**  
**August 2011**



THE GRADUATE COLLEGE

We recommend the dissertation prepared under our supervision by

**Brian D. Hosterman**

entitled

**Raman Spectroscopic Study of Solid Solution Spinel Oxides**

be accepted in partial fulfillment of the requirements for the degree of

**Doctorate of Philosophy in Physics**

Department of Physics

John Farley, Committee Chair

Allen Johnson, Committee Member

Michael Pravica, Committee Member

Oliver Tschauner, Committee Member

Clemens Heske, Graduate College Representative

Ronald Smith, Ph. D., Vice President for Research and Graduate Studies  
and Dean of the Graduate College

**August 2011**

## ABSTRACT

### Raman Spectroscopic Study of Solid Solution Spinel Oxides

by

Brian D. Hosterman

Dr. John Farley, Examination Committee Chair

Professor of Physics

University of Nevada, Las Vegas

Solid solution spinel oxides of composition  $\text{Mg}_x\text{Ni}_{1-x}\text{Cr}_2\text{O}_4$ ,  $\text{NiFe}_x\text{Cr}_{2-x}\text{O}_4$ , and  $\text{Fe}_x\text{Cr}_{3-x}\text{O}_4$  were synthesized and characterized using x-ray diffraction and Raman spectroscopy. Frequencies of the Raman-active modes are tracked as the metal cations within the spinel lattice are exchanged. This gives information about the dependence of the lattice vibrations on the tetrahedral and octahedral cations. The highest-frequency Raman-active mode,  $A_{1g}$ , is unaffected by substitution of the divalent tetrahedral cation, whereas the lower frequency vibrations are more strongly affected by substitution of the tetrahedral cation. The change in wavenumber of many phonons is nonlinear upon cation exchange. All detected modes of  $\text{Mg}_x\text{Ni}_{1-x}\text{Cr}_2\text{O}_4$  and  $\text{Fe}_x\text{Cr}_{3-x}\text{O}_4$  exhibit one-mode behavior. Additional modes are detected in the  $\text{NiFe}_x\text{Cr}_{2-x}\text{O}_4$  series due to cation inversion of the spinel lattice.

Results from the  $\text{Fe}_x\text{Cr}_{3-x}\text{O}_4$  spinels are then applied to identifying the corrosion layers of three stainless steel samples exposed to lead-bismuth eutectic in a high-temperature, oxygen-controlled environment. The Raman spectrum of the outer cor-

rosion layer in all steels is identified as  $\text{Fe}_3\text{O}_4$ . The wavenumber of the  $A_{1g}$  mode for the inner corrosion layer indicates an iron chromium spinel oxide. Micro-Raman spectroscopy proves capable of determining structural and compositional differences between complex corrosion layers of stainless steels.

## ACKNOWLEDGMENTS

I would like to thank the following people whose assistance and support in this dissertation has been invaluable and much appreciated: John Farley, Allen Johnson, Michael Pravica, Oliver Tschauner, Clemens Heske, Ning Li, Dale Perry, Amadeo Sanchez, James Norton, David Hatchett, Thomas Hartmann, Clay Crow, David Shelton, Daniel Koury, Peter Faught, Thao Ho Trung, John Kilburg, Bill O'Donnell, Sandip Thanki, Marcus Vasquez, Luke Wilson, Alexandra Léandre, Michael Rodriguez, Joseph Lussier, and Brittany Morgan. Funding is provided through the University of Nevada, Las Vegas Transmutation Research Program, administered through the Harry Reid Center for Environmental Studies, and is gratefully acknowledged.

## TABLE OF CONTENTS

ABSTRACT .....	iii
ACKNOWLEDGMENTS.....	v
LIST OF TABLES .....	ix
LIST OF FIGURES .....	x
CHAPTER 1 INTRODUCTION .....	1
Corrosion .....	3
Transmutation .....	4
CHAPTER 2 CRYSTAL STRUCTURE AND VIBRATIONS .....	7
Vibrations.....	7
Phonons .....	11
Spinel structure .....	11
Corundum structure .....	15
Solid solutions.....	16
The Jahn-Teller effect .....	17
X-ray diffraction .....	19
CHAPTER 3 RAMAN SCATTERING AND INFRARED ABSORPTION ..	22
Raman Scattering .....	23
Polarizability tensor .....	25
Infrared absorption .....	26
Wavenumbers .....	27
CHAPTER 4 PREVIOUS WORK .....	28
LBE-corroded steels .....	28
Identifying corrosion layers using Raman spectroscopy.....	31
Theoretical work of the spinel system.....	32
Assignment of the vibrations of spinel .....	33

Experimental work on the spinel vibrations . . . . .	36
Experimental work on solid solution spinels . . . . .	44
CHAPTER 5 EXPERIMENTAL SETUP . . . . .	48
Spinel synthesis . . . . .	49
X-ray diffraction . . . . .	55
Determination of lattice parameters . . . . .	57
Infrared photoacoustic spectroscopy . . . . .	58
Raman microscope . . . . .	60
Software and calibration . . . . .	65
Peak fitting . . . . .	66
Error analysis . . . . .	69
CHAPTER 6 OXIDE STANDARDS . . . . .	71
Hematite, $\alpha$ -Fe <sub>2</sub> O <sub>3</sub> . . . . .	71
Magnetite, Fe <sub>3</sub> O <sub>4</sub> . . . . .	72
Chromium oxide, Cr <sub>2</sub> O <sub>3</sub> . . . . .	77
CHAPTER 7 CHROMITES & FERRITES . . . . .	79
FeCr <sub>2</sub> O <sub>4</sub> . . . . .	79
MgCr <sub>2</sub> O <sub>4</sub> . . . . .	81
NiCr <sub>2</sub> O <sub>4</sub> . . . . .	83
NiFe <sub>2</sub> O <sub>4</sub> . . . . .	87
CHAPTER 8 SOLID SOLUTION SPINELS . . . . .	91
Mg <sub>x</sub> Ni <sub>1-x</sub> Cr <sub>2</sub> O <sub>4</sub> . . . . .	91
NiFe <sub>x</sub> Cr <sub>2-x</sub> O <sub>4</sub> . . . . .	98
Fe <sub>x</sub> Cr <sub>3-x</sub> O <sub>4</sub> . . . . .	106
Discussion on solid solutions . . . . .	113
CHAPTER 9 LBE-CORRODED STAINLESS STEELS . . . . .	118
CHAPTER 10 CONCLUSIONS . . . . .	124
APPENDIX A RIETVELD REFINEMENT RESULTS . . . . .	127
NiCr <sub>2</sub> O <sub>4</sub> . . . . .	128
Mg <sub>x</sub> Ni <sub>1-x</sub> Cr <sub>2</sub> O <sub>4</sub> . . . . .	129



NiFe <sub>x</sub> Cr <sub>2-x</sub> O <sub>4</sub> . . . . .	130
Fe <sub>x</sub> Cr <sub>3-x</sub> O <sub>4</sub> . . . . .	131
REFERENCES . . . . .	132
VITA . . . . .	144

## LIST OF TABLES

Table 1	C <sub>2v</sub> Character table . . . . .	10
Table 2	O <sub>h</sub> character table . . . . .	12
Table 3	Compiled Raman data on AB <sub>2</sub> O <sub>4</sub> II-III spinels . . . . .	37
Table 4	316L, D9, and HT9 stainless steels . . . . .	49
Table 5	Silicon standard XRD spectrum . . . . .	57
Table 6	Lattice parameters of synthesized spinels . . . . .	59
Table 7	Neon calibration lines . . . . .	66
Table 8	Argon emission lines . . . . .	68
Table 9	Raman-active phonons of α-Fe <sub>2</sub> O <sub>3</sub> . . . . .	73
Table 10	Raman-active phonons of Fe <sub>3</sub> O <sub>4</sub> . . . . .	75
Table 11	Raman-active phonons of Cr <sub>2</sub> O <sub>3</sub> . . . . .	77
Table 12	Raman-active phonons of FeCr <sub>2</sub> O <sub>4</sub> . . . . .	80
Table 13	Raman-active phonons of MgCr <sub>2</sub> O <sub>4</sub> . . . . .	83
Table 14	Lattice parameters of NiCr <sub>2</sub> O <sub>4</sub> . . . . .	86
Table 15	Raman-active phonons of NiCr <sub>2</sub> O <sub>4</sub> . . . . .	88
Table 16	Raman-active phonons of NiFe <sub>2</sub> O <sub>4</sub> . . . . .	90
Table 17	Rietveld refinements for NiCr <sub>2</sub> O <sub>4</sub> . . . . .	128
Table 18	Rietveld refinements for Mg <sub>x</sub> Ni <sub>1-x</sub> Cr <sub>2</sub> O <sub>4</sub> . . . . .	129
Table 19	Rietveld refinements for NiFe <sub>x</sub> Cr <sub>2-x</sub> O <sub>4</sub> . . . . .	130
Table 20	Rietveld refinements for NiFe <sub>x</sub> Cr <sub>2-x</sub> O <sub>4</sub> . . . . .	131

## LIST OF FIGURES

Figure 1	Radiotoxicity of nuclear waste . . . . .	6
Figure 2	Spinel unit cell . . . . .	12
Figure 3	Raman scattering from a molecule . . . . .	23
Figure 4	Rayleigh and Raman scattering . . . . .	24
Figure 5	SEM image of a stainless steel sample . . . . .	29
Figure 6	EDS elemental map of a stainless steel sample . . . . .	30
Figure 7	Raman-active modes of chromites vs. $1/m^2$ . . . . .	40
Figure 8	Wavenumber of $A_{1g}$ mode for Zn and Mg spinels $A_{1g}$ vs. $1/m^2$ . . . . .	41
Figure 9	Chromite Raman frequencies vs. ionic radius . . . . .	44
Figure 10	Combustion synthesis schematic . . . . .	50
Figure 11	Synthesized spinel . . . . .	51
Figure 12	Weak XRD spectrum of an iron chromite . . . . .	53
Figure 13	Iron chromite showing corundum phase . . . . .	54
Figure 14	Schematics of the reduction furnace . . . . .	55
Figure 15	Spinel diffraction pattern containing Si standard . . . . .	58
Figure 16	Rietveld refinement of $MgCr_2O_4$ . . . . .	59
Figure 17	Schematic of the micro-Raman spectrometer . . . . .	61
Figure 18	Photograph of the micro-Raman spectrometer . . . . .	62
Figure 19	Micro-Raman focused spot size . . . . .	63
Figure 20	Uncalibrated neon emission spectrum . . . . .	67
Figure 21	Calibrated argon emission spectrum . . . . .	68
Figure 22	Raman spectrum of $Cr_2O_3$ . . . . .	70
Figure 23	Raman spectrum of $\alpha\text{-Fe}_2O_3$ . . . . .	72
Figure 24	Peak fit of $\alpha\text{-Fe}_2O_3$ . . . . .	73
Figure 25	Raman spectrum of $Fe_3O_4$ . . . . .	74
Figure 26	Raman spectra of $Fe_3O_4$ as a function of laser power . . . . .	76
Figure 27	Raman spectrum of $Cr_2O_3$ . . . . .	78
Figure 28	Raman spectrum of $FeCr_2O_4$ . . . . .	80
Figure 29	X-ray diffraction spectrum of $MgCr_2O_4$ . . . . .	81

Figure 30 Raman spectrum of $\text{MgCr}_2\text{O}_4$ . . . . .	82
Figure 31 XRD spectrum of $\text{NiCr}_2\text{O}_4$ . . . . .	85
Figure 32 $c/a$ of tetragonal $\text{NiCr}_2\text{O}_4$ . . . . .	87
Figure 33 Raman spectrum of $\text{NiCr}_2\text{O}_4$ . . . . .	88
Figure 34 Raman spectrum of $\text{NiFe}_2\text{O}_4$ . . . . .	89
Figure 35 Mixed versus synthesized spinel . . . . .	92
Figure 36 Lattice constants of $\text{Mg}_x\text{Ni}_{1-x}\text{Cr}_2\text{O}_4$ . . . . .	93
Figure 37 Raman spectra of $\text{Mg}_x\text{Ni}_{1-x}\text{Cr}_2\text{O}_4$ . . . . .	94
Figure 38 Raman peak positions of $\text{Mg}_x\text{Ni}_{1-x}\text{Cr}_2\text{O}_4$ . . . . .	95
Figure 39 B-O bond distance of $\text{Mg}_x\text{Ni}_{1-x}\text{Cr}_2\text{O}_4$ . . . . .	97
Figure 40 IR peak positions of $\text{Mg}_x\text{Ni}_{1-x}\text{Cr}_2\text{O}_4$ . . . . .	98
Figure 41 Lattice parameters of $\text{NiFe}_x\text{Cr}_{2-x}\text{O}_4$ . . . . .	100
Figure 42 Raman spectra of $\text{NiFe}_x\text{Cr}_{2-x}\text{O}_4$ . . . . .	101
Figure 43 Raman peak positions of $\text{NiFe}_x\text{Cr}_{2-x}\text{O}_4$ . . . . .	102
Figure 44 Vibrational peak positions of $\text{NiFe}_x\text{Cr}_{2-x}\text{O}_4$ . . . . .	103
Figure 45 B-O bond distance of $\text{NiFe}_x\text{Cr}_{2-x}\text{O}_4$ . . . . .	105
Figure 46 Lattice constants of $\text{Fe}_x\text{Cr}_{3-x}\text{O}_4$ . . . . .	109
Figure 47 $A_{1g}$ and $F_{2g}(3)$ positions of $\text{Fe}_x\text{Cr}_{3-x}\text{O}_4$ . . . . .	112
Figure 48 Raman spectra of HT9 corrosion layers . . . . .	119
Figure 49 Raman spectra of outer corrosion layer . . . . .	120
Figure 50 $A_{1g}$ position from LBE-corroded steels . . . . .	121
Figure 51 Raman spectra of inner corrosion layer . . . . .	123

## CHAPTER 1

### INTRODUCTION

The term “spinel” originated as a name for a typically red gemstone, though the gem also occurs in varying shades of pink, purple and blue. Spinel with a deep red color were often mistaken for rubies, and many large red gemstones in medieval jewelry and crowns are actually spinel instead of ruby. Although ruby and spinel look similar to the eye, the periodic arrangement of the atoms within these crystals are very different. Spinel,  $\text{MgAl}_2\text{O}_4$ , exists as a crystal lattice that has now simply been termed the spinel structure, which many compounds of the form  $\text{AB}_2\text{X}_4$  share. Ruby,  $\text{Al}_2\text{O}_3$ , with chromium impurities, exhibits the crystal structure known as corundum. The common red rust,  $\alpha\text{-Fe}_2\text{O}_3$ , also crystallizes into the corundum structure [1].

Metal oxides having the spinel structure,  $\text{AB}_2\text{O}_4$ , are important materials of technological and geological interest. Many varieties of spinels appear within the Earth’s crust, whose properties must be understood for geological considerations [2,3].  $\text{MgCr}_2\text{O}_4$ ,  $\text{MgAl}_2\text{O}_4$ ,  $\text{FeCr}_2\text{O}_4$ , and  $\text{Fe}_3\text{O}_4$  are all common minerals of the Earth’s crust. The low solubility of chromium within basaltic magma leads to the crystallization of chromite [4]. Olivine,  $(\text{Mg, Fe})_2\text{SiO}_4$ , belonging to another class of crystal structures related to spinel, is the most abundant mineral within the upper mantle, and at high pressure undergoes a phase transition to the spinel structure [5–7]. This high-pressure phase of olivine is known as Ringwoodite. Olivine can also contain small amounts of other elements such as nickel and manganese [8].

Spinel oxides have been discovered in Martian meteorites [9]. The iron oxide spinel

magnetite,  $\text{Fe}_3\text{O}_4$ , named for its magnetic properties, provides evidence for magnetism on the red planet [10].

Spinel also holds much interest for technological applications.  $\text{MgCr}_2\text{O}_4$  and  $\text{MgAl}_2\text{O}_4$  are stable at high temperatures and have low coefficients of expansion, making them effective refractory materials, important to the steel, cement, and copper industries [11–13]. Recently, there has been much interest in the  $\text{LiMn}_2\text{O}_4$  spinel as a low cost, safer cathode material for lithium batteries [14–16]. In addition to magnetite, many spinels have many interesting magnetic properties. Nickel and zinc ferrites have been studied for use as transformer cores and components in radio frequency coils [17]. Ultra-fine particles of  $\text{ZnFe}_2\text{O}_4$  possess larger magnetism than bulk  $\text{ZnFe}_2\text{O}_4$  [18].

In many circumstances, natural spinels are solid solutions of two or more  $\text{AB}_2\text{O}_4$  spinels, where the mixing happens within the crystal structure. These are called solid solutions and are also of interest for their technological applications and geological relevance. The common mineral iron chromite, from which metallic chromium is extracted, is found in peridotite within the Earth’s mantle. Chromite ore is rarely pure  $\text{FeCr}_2\text{O}_4$  and instead contains significant amounts of magnesium and aluminum to create a solid solution  $(\text{Fe,Mg})(\text{Cr,Al})_2\text{O}_4$  [4, 9, 19]. The opposite end of this solid solution leads again towards the  $\text{MgAl}_2\text{O}_4$  mineral, while containing minor inclusions of iron and chromium.

Many solid solution series are interesting to study because of magnetic or electrochemical properties of the ionic systems that arise from cation substitution. Magnetic properties of  $\text{Zn}_{1-x}\text{Ni}_x\text{Fe}_2\text{O}_4$  are sensitive to atomic composition [17, 20]. Other metals, such as cobalt and nickel, have been examined as substitutes for manganese in  $\text{LiMn}_2\text{O}_4$  and for alternative materials in rechargeable lithium batteries [15, 16].

$\text{NiFe}_x\text{Cr}_{2-x}\text{O}_4$  has been considered for use as a cheap cathodic material for the

reduction of  $\text{NO}_x$  gases [21]. This series is also an interesting case to study ferrimagnetism effects and the differences between the magnetic properties of ferrites and chromites [22]. Ferrites exhibit strong ferrimagnetic ordering between the octahedral and tetrahedral sites, but the addition of chromium leads to antiferromagnetic interactions [23].

### Corrosion

Corrosion is the oxidation reaction of a metal to form a metal oxide. Most people are familiar with corrosion and the damage this process causes to metals. A piece of unprotected iron develops flaky red spots and degrades over time. This occurs because the pure iron reacts with oxygen in air to create the common red rust known as hematite,  $\alpha\text{-Fe}_2\text{O}_3$ .  $\alpha\text{-Fe}_2\text{O}_3$  has little structural integrity, and crumbles away to expose fresh iron underneath to the same oxidation conditions. Over time, the entire piece of iron will oxidize and fail.

Fewer people realize that oxidation is also necessary to protect materials. The addition of chromium to iron led to the development of the stainless steels. Chromium reacts with air much faster than the iron-air reaction and forms  $\text{Cr}_2\text{O}_3$ , which, unlike  $\alpha\text{-Fe}_2\text{O}_3$ , is strong and protective in normal conditions. This surface chromium oxide layer acts as a passivation layer that protects the underlying alloy from further oxidation. Unfortunately though, in extreme conditions such as high temperatures, even this chromium oxide layer can fail, and non-protective oxides begin to form, leading to the eventual failure of the alloy.

Spinel structured metal oxides are a major product formed during corrosion. Magnetite,  $\text{Fe}_3\text{O}_4$ , is often reported during the corrosion of high-iron stainless steels [24, 25].  $\text{NiCr}_2\text{O}_4$  is a common product formed from high-nickel alloys in oxidizing environments [26–28].  $\text{MnCr}_2\text{O}_4$  has also been reported to be produced on nickel-

based and high-nickel alloys in corrosive environments, [29], and even as an agent for further corrosion [30].

Hemmi et al. report that a  $\text{NiFe}_2\text{O}_4$  layer passivates the surface of a nickel and cobalt alloy by restricting the dissolution of metals [31]. A protective layer containing  $\text{MnCr}_2\text{O}_4$  is found during the corrosion of nickel-based alloys in a high-temperature steam environment [32].

Corrosion of complicated alloys is not completely understood. Alloys are often developed via “cook and look” methods, where many different alloys are created and the alloys with desirable properties are selected without a complete understanding of the mechanics of corrosion. To fully understand the corrosion process, it is necessary to know the chemical species of the oxides within the corrosion layers. Corrosion is also a large concern for the nuclear industry, and materials must be engineered to maximize the lifetime of reactors, where high temperatures lead to corrosive environments.

#### Transmutation

Even if the public recovers from the recent nuclear catastrophe in Japan, in order for a nuclear power revival to occur, public fear regarding nuclear waste must be addressed. Projects such as Yucca Mountain were proposed to deal with long term storage of radioactive nuclear waste. Because the Yucca project is indefinitely abandoned, other methods of dealing with the long term dangers of nuclear waste storage need to be developed. A facility designed to store untreated nuclear waste must protect against radiation from the nuclear waste products, which can have very long lifetimes. If a full nuclear revival does happen, a single site such as Yucca mountain will be inadequate, and many more storage facilities will be required to store the increasing amount of waste. The negative attitude that the public holds towards such storage facilities is an enormous roadblock that will be difficult, if not impossible, to



overcome.

Only about one percent of the fission products within spent nuclear waste creates issues with long term storage. The majority of nuclear waste is in the form of uranium, which can be recycled or disposed of as low level waste. The storage problem arises with plutonium and other minor actinides (neptunium, americium, curium), which have half-lives on the order of hundreds of thousands of years. Engineering containment vessels, in addition to a storage facility to house these vessels, that are safe for such a long period of time, is very difficult.

Transmutation provides an alternative solution for dealing with radioactive waste. Transmutation is the process of changing one element into another via nuclear reactions. The problematic, long-lived actinides can be transmuted into elements with much shorter half-lives. This is achieved in high-Z materials via neutron bombardment. The absorption of neutrons by the nucleus of an atom leads to instability, and the atom decays to a more stable, less radioactive isotope. As evident from Figure 1, the toxicity of these dangerous transuranics are reduced by several orders of magnitude via transmutation [33].

Lead-bismuth eutectic (LBE) has been proposed as both a spallation target for the production of neutrons, and as a coolant in nuclear reactors. LBE is an alloy containing 45 percent lead and 55 percent bismuth by weight. LBE is classified as an eutectic because its melting point (124°C) is less than the melting point of either pure lead (327°C) or pure bismuth (271°C), and is the lowest melting point for any mixture of lead and bismuth. This low melting point, along with its boiling point (1670°C) gives the material a wide range of operating temperatures. LBE is also inert to both air and water, giving it an advantage over other available liquid-metal coolants, such as sodium, which violently reacts with water. However, in a nuclear environment, the LBE will be heated to a high temperature and can potentially corrode the stainless

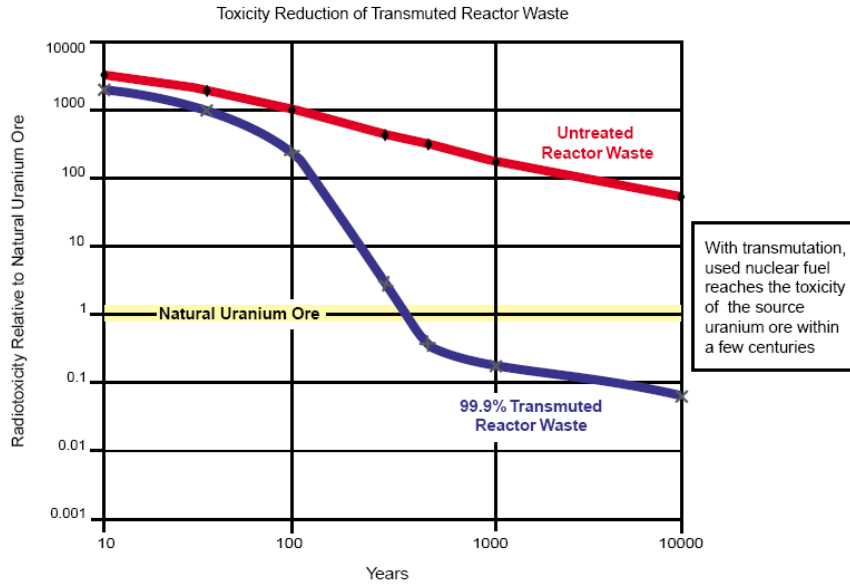


Figure 1. Radiotoxicity of nuclear waste with and without transmutation [33].

steel pipes through which the liquid metal flows.

Metallics such as iron will dissolve in the liquid LBE at the operational temperatures of the nuclear facility. This dissolution corrosion can be mitigated by the formation of a passivating, protective oxide layer. If small amounts of oxygen are added to the LBE, oxide layers are formed that inhibit the dissolution corrosion. However, the mechanics of the corrosion, and the actual oxides produced, is not completely understood. The present work will examine these corrosion layers formed on three grades of stainless steel exposed to lead-bismuth eutectic in a high-temperature, oxygen-controlled environment.

## CHAPTER 2

### CRYSTAL STRUCTURE AND VIBRATIONS

The arrangement of atoms into molecules or crystal lattices is fundamentally important to the physical, electronic, and chemical properties of a material. A crystal is a solid constructed from a periodic array of atoms. A lump of pure iron has a crystal structure, as the iron atoms organize into a periodic arrangement to minimize free energy.

#### Vibrations

The vibrational properties of different molecules and crystal structures are unique, and can also be used to identify the composition and structure of a material. Group theory provides a mathematical tool for studying vibrational properties of crystal structures. A group is a set of elements and an operation, such that the operation combines two elements of the group into an element of the group. A complete discussion on group theory is unnecessary here, but a few concepts need to be presented as relevant terms will be used during the discussion of theory and data. Other authors have presented detailed introductions of group theory and its application to vibrations [34–36].

Molecules and crystals have geometries with varying degrees of symmetry. Symmetry operations, such as rotations, are geometric transformations that leave a molecule indistinguishable from its original orientation. For example, if one rotates a cube with 6 identical surfaces 90 degrees about any axis normal to, and in the center of a square surface, the new position is equivalent to the original orientation. However,

if one dimension of the cube is lengthened, creating rectangles out of four of the six sides, some of the symmetry elements of the cubic system are lost. The system is now indistinguishable from the original orientation when rotated 90 degrees about an axis normal to the two remaining square faces and 180 degrees when rotated about an axis normal to the rectangular face.

There are seven basic crystal systems: cubic, hexagonal, rhombohedral, tetragonal, orthorhombic, monoclinic, and triclinic. These systems are constructed from characteristic symmetry elements, created by a periodic arrangement of identical particles. The cubic system is created by translating a particle along the  $x$ ,  $y$ ,  $z$  axes at a periodic distance. The tetragonal system is created similarly, except that the distance along one axis differs from the other two. Some of the crystal systems have different arrangements that still obey the same symmetry elements. For example, a cube constructed with a particle at each corner, can also have a particle in the center of each face. This face-centered system still obeys all the symmetry elements of the cubic system. There are 14 distinct geometries, associated with arrangement of identical particles, distributed among the seven crystal systems called the Bravais lattices.

Most natural occurring crystal systems are not Bravais lattices. Instead of a single particle at each lattice site, the system contains an identical group of particles at each lattice site. These systems are constructed using the basis vectors of the Bravais lattice.

A total of five symmetry elements lead to 32 crystallographic point groups. The identity operator,  $E$ , leaves the structure unchanged. The rotation operator,  $C_n$ , rotates the structure through an angle of  $360^\circ/n$  about an axis, where  $n$  is an integer. Vertical and horizontal mirror plane operators,  $\sigma_v$  and  $\sigma_h$ , reflect all atoms in the structure about a plane. A center of inversion operator,  $i$ , reflects all points in the

structure across a center of symmetry. The rotation reflection operator,  $S_n$ , also known as an improper rotation, involves both a rotation and a reflection.

The symmetry elements of a point group may be combined into classes. The ammonia molecule has both a rotation of  $120^\circ$  and a rotation of  $240^\circ$  around its principal axis as symmetry elements. It also has three mirror planes that intersect the principal axis. These elements form two separate classes.

The symmetry operations can be represented by matrices. A set of matrices that describe the symmetry operations is known as a representation. A representation will depend upon the choice of basis coordinates. To prevent confusion as to which representation is being used, irreducible representations are introduced. Any arbitrary representation can be described by a linear combination of these irreducible representations. The trace of a matrix is the sum of its diagonal elements and is called a character. The character of a representation is independent of the choice of basis coordinates. The number of irreducible representations belonging to a point group is equal to the number of symmetry classes of the point group. This allows the construction of a square character table that lists the characters of each symmetry class for every irreducible representation. There are the same amount of irreducible classes as there are symmetry classes of the point group.

As an example, the character table of the  $C_{2v}$  point group is shown in Table 1. Water,  $H_2O$ , belongs to this point group and thus, all vibrational modes of gas phase water are well known. The top header row of the character table labels the point group and identifies which, and how many, symmetry elements belong to the group. The  $C_{2v}$  point group contains the identity element, a rotation of 180 degrees, and two orthogonal vertical mirror planes. The remaining four rows identify the characters of the orthogonal irreducible representation matrices.  $A$  and  $B$  are one-dimensional representations. Other point groups may have two and three dimensional representations,

$C_{2v}$	$E$	$C_2$	$\sigma_v(xz)$	$\sigma_v(yz)$		
$A_1$	+1	+1	+1	+1	$T_z$	$\alpha_{xx}, \alpha_{yy}, \alpha_{zz}$
$A_2$	+1	+1	-1	-1	$R_z$	$\alpha_{xy}$
$B_1$	+1	-1	+1	-1	$T_x, R_y$	$\alpha_{xz}$
$B_2$	+1	-1	-1	+1	$T_y, R_x$	$\alpha_{yz}$

Table 1. The character table for the  $C_{2v}$  point group.

which are identified by the  $E$  and  $F$  labels, respectively. Any normal vibration of the molecule can be represented by one of these irreducible representations. Herzberg's equations and knowledge of the atoms within the molecule can be used to determine the number of vibrations in each representation [35]. Using the equation for the  $C_{2v}$  group, water has two  $A_1$  vibrations and a single  $B_2$  vibration.

The two rightmost columns of Table 1 give the infrared and Raman activity of the representations. A vibration is infrared-active if the vibration species contains a translational motion ( $T_x, T_y, T_z$ ) and Raman-active if the vibration species contains an element of the polarizability tensor,  $\alpha_{ij}$ . For the water molecule example, the  $A_1$  and  $B_2$  species have both translational and polarizability elements. Therefore, all three vibrational modes of water are infrared and Raman-active. If the structure contains the center of inversion symmetry element, then modes can only be Raman-active or infrared-active, but not both. These selection rules will be discussed in more detail in the following chapter.

Factor group analysis is another common approach for determining the vibrational modes of a crystal [37]. The factor group is isomorphic to the point group. This analysis examines how many times an irreducible representation is contained in the general reducible representation for the crystal. White and DeAngelis utilize this analysis for the spinel lattice to identify the normal modes of the lattice [38].

The five symmetry elements discussed above completely describe molecular symmetry. However, to describe an infinite crystal lattice, two additional symmetry elements are required. A particle can also be translated along an axis of the crystal. The two extra symmetry elements that result are the screw axis and the glide plane. A screw axis is a translation along an axis, followed by a rotation about that axis. The glide plane also involves a translation along an axis, but is instead followed by a reflection about a plane parallel to the axis. This leads to a total of 230 space groups required to describe the structural symmetry of crystals [39].

### Phonons

The quantized modes of vibrations in a crystal lattice are called phonons. A phonon represents the collective motion of the entire lattice from one normal mode of vibration, which can be represented by one of the irreducible representations. Phonons can interact with other particles, such as photons and electrons. The photon-phonon interaction is the basis for vibrational spectroscopy techniques used to study crystals, such as Raman scattering and infrared absorption. Phonons contribute to the specific heat of crystals, as the energy added to a crystal can create phonons. The phonon density of states of different materials has been extensively studied and reported.

### Spinel structure

The spinel class of oxides,  $AB_2O_4$ , where A and B represent differing cations and O is oxygen, belongs to space group  $Fd\bar{3}m$  ( $O_h^h$ ), a cubic lattice consisting of 8 molecules within the unit cell, for a total of 56 atoms. This space group belongs to the  $O_h$  point group, having the character table shown in Table 2. The unit cell of spinel is shown in Figure 2.

Because of the large number of atoms within the spinel unit cell, it is common to

	E	8C <sub>3</sub>	6C <sub>2</sub>	6C <sub>4</sub>	3C <sub>2</sub>	i	6S <sub>4</sub>	8S <sub>6</sub>	3σ <sub>h</sub>	6σ <sub>d</sub>	
A <sub>1g</sub>	1	1	1	1	1	1	1	1	1	1	$x^2 + y^2 + z^2$
A <sub>2g</sub>	1	1	-1	-1	1	1	-1	1	1	-1	
A <sub>1u</sub>	1	1	1	1	1	-1	-1	-1	-1	-1	
A <sub>2u</sub>	1	1	-1	-1	1	-1	1	-1	-1	1	
E <sub>g</sub>	2	-1	0	0	2	2	0	-1	2	0	$(2z^2 - x^2 - y^2, x^2 - y^2)$
E <sub>u</sub>	2	-1	0	0	2	-2	0	1	-2	0	
F <sub>1g</sub>	3	0	-1	1	-1	3	1	0	-1	-1	$(R_x, R_y, R_z)$
F <sub>1u</sub>	3	0	-1	1	-1	-3	-1	0	1	1	$(x, y, z)$
F <sub>2g</sub>	3	0	1	-1	-1	3	-1	0	-1	1	$(xz, yz, xy)$
F <sub>2u</sub>	3	0	1	-1	-1	-3	1	0	1	-1	

Table 2. The character table of the the  $O_h$  point group, to which the spinel system belongs.

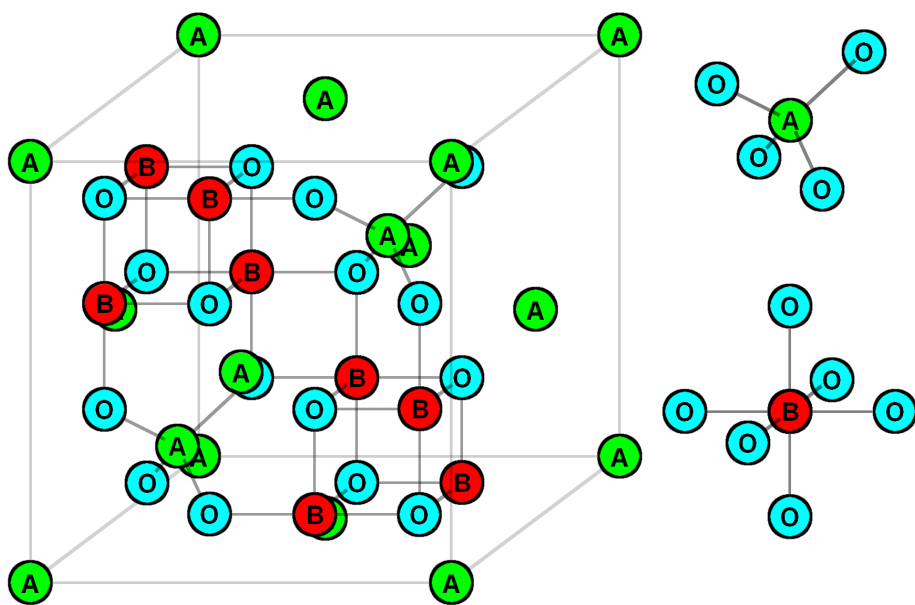


Figure 2. The unit cell of a normal  $AB_2O_4$  spinel contains 8 molecules. The  $A^{2+}$  and  $B^{3+}$  cations occupy the tetrahedral and octahedral sites, respectively. To simplify the image, only the front half of the unit cell's interior is shown. The tetrahedral cations are bonded to four oxygen atoms, whereas the octahedral cations are bonded to six oxygen atoms, shown to the right of the unit cell.



identify sub-units within the spinel unit cell, also displayed in Figure 2. A tetrahedral unit,  $\text{AO}_4$  is comprised of the cation at the center of a cube and four oxygen atoms in the nonadjacent corners. The octahedral unit consists of a cation surrounded by six oxygen atoms, two along each dimensional axis, to form a  $\text{BO}_6$  octahedron.

The tetrahedra within the spinel lattice are isolated from one another. No sides of a tetrahedron are in contact with other tetrahedra. The octahedral units, on the other hand, do share a single edge. Two oxygen atoms are shared between adjacent octahedra.

Atoms other than oxygen can occupy the anion position of the spinel lattice. Sulfur and selenium belong to the same periodic group as oxygen and many spinels are composed of these elements. A class of compounds known as the “cyanospinel” with formula,  $\text{A}_2\text{M}(\text{CN})_4$ , also exist. Spinel containing oxygen are exclusively examined in the present work, though work on spinels composed of sulfur and selenium will be referenced.

In a normal spinel, shown in Figure 2, the  $\text{A}^{2+}$  cations occupy the tetrahedral positions, and the  $\text{B}^{3+}$  cations occupy the octahedral positions. A completely inverse spinel places one half of the  $\text{B}^{3+}$  cations onto all of the tetrahedral positions and the remaining half on the octahedral sites, while the  $\text{A}^{2+}$  cations fill up the remaining half of the octahedral positions. Spinel systems may exist in a state between completely normal and inverse, and thus an inversion parameter is defined,  $\xi$ , which indicates the fraction of  $\text{A}^{2+}$  cations occupying octahedral positions.

Spinel often have cations with valences other than +2 or +3. Different classes of spinels are often defined by the valences of the spinel’s cations. The spinels in the present work belong to the normal and inverse class of II-III spinels, as they contain cations with valences of +2 and +3.  $\gamma\text{-Ni}_2\text{SiO}_4$ , containing  $\text{Ni}^{2+}$  and  $\text{Si}^{4+}$ , is an example of a II-IV spinel.  $\text{LiMn}_2\text{O}_4$  is constructed with  $\text{Li}^{1+}$  occupying the

tetrahedral sites of the lattice, and  $\text{Mn}^{3+}$  and  $\text{Mn}^{4+}$  occupying the octahedral sites. Many cation deficient spinels also exist, such as  $\gamma\text{-Fe}_2\text{O}_3$ , having octahedral vacancies.

Inversion of the spinel lattice leads to the existence of  $\text{BO}_4$  tetrahedra and  $\text{AO}_6$  octahedra. Inversion occurring in usually normal spinels is often referred to as cation disorder. Cation disorder has been reported to cause discrepancies in the vibrational spectra of spinels. The extra observed peak in synthetic spinels has often been attributed to aluminum cations occupying the tetrahedral position [2, 7, 40]. Many of the extra peaks in the inverse spinel  $\text{NiAl}_2\text{O}_4$  are reported to be a result of the random distribution of the divalent nickel within the octahedral sites, where each cation configuration contributes locally to the additional peaks [41].

Although 56 atoms are present within the spinel's unit cell, only 14 atoms are necessary to construct the simplest primitive cell. The factor group analysis presented first by White and DeAngelis [38] shows that the 42 normal modes of spinel, 3 acoustic modes and 39 optical modes, belong to the symmetry species

$$A_{1g}(\text{R}) + E_g(\text{R}) + F_{1g} + 3F_{2g}(\text{R}) + 2A_{2u} + 2E_u + 5F_{1u}(\text{IR}) + 2F_{2u}. \quad (2.1)$$

The (R) and (IR) identify Raman- and infrared-active vibrational species, respectively. The  $E_g$  and  $F_{2g}$  modes are doubly and triply degenerate, respectively. The three acoustic modes belong to a single  $F_{1u}$  species. A common notation exists in most of the literature to distinguish between the Raman and IR modes belonging to the same representation, and will be used in the present work. The three Raman-active  $F_{2g}$  modes are labeled  $F_{2g}(1)$ ,  $F_{2g}(2)$ , and  $F_{2g}(3)$ , where  $F_{2g}(1)$  is the lowest-frequency  $F_{2g}$  mode and  $F_{2g}(3)$  is the highest-frequency mode of this vibrational species. Conversely, the four IR-active  $F_{1u}$  modes are labeled  $\nu_1$ ,  $\nu_2$ ,  $\nu_3$ , and  $\nu_4$  in descending value of frequency.  $\nu_1$  is the highest-frequency  $F_{1u}$  mode, whereas  $\nu_4$  is the lowest-frequency mode.

Because the spinel structure has an inversion symmetry element, the active modes are mutually exclusive. Thus, the vibrational modes are either infrared- or Raman-active, but not both.

The atomic positions within a crystal can be defined as a fraction of the lattice parameter of the unit cell,  $a$ . The ideal spinel lattice assumes that the oxygen atoms are arranged as a cubic close-packed array. However, the oxygen position of many spinels deviates slightly from this ideal geometry, and instead are displaced along a direction perpendicular to the diagonal of the cube, and an oxygen parameter,  $u$ , is defined, where  $u = 3/8$  for the ideal structure. Hill et al. list the mathematical expressions for calculating distances between neighboring atoms within the spinel lattice. The A-O and B-O bond distances are given by

$$\text{A-O} : a\sqrt{3}(u - 0.125) \quad (2.2)$$

$$\text{B-O} : a\sqrt{3u^2 - 2u + 0.375}, \quad (2.3)$$

where  $a$  is the lattice parameter, and  $u$  is the oxygen parameter [42].

### Corundum structure

Corundum is the name originally given to  $\text{Al}_2\text{O}_3$ , which, though similar to the term spinel describing the structure adopted by many  $\text{AB}_2\text{O}_4$  compounds, is also the generic term that applies to isomorphous compounds of  $\text{Al}_2\text{O}_3$ , having the general formula  $\text{B}^2\text{O}^3$ .  $\alpha\text{-Fe}_2\text{O}_3$  and  $\text{Cr}_2\text{O}_3$  adopt the corundum structure, a hexagonal lattice belonging to the  $R\bar{3}c$  space group. The structure is a hexagonal close-packed array of oxide ions with two-thirds of the octahedral sites being filled with the  $\text{B}^{3+}$  cations.

The vibrational spectra of corundum-structured oxides are well known [1, 43, 44], and will not be studied in depth here. Two corundum-structured oxides,  $\alpha\text{-Fe}_2\text{O}_3$  and  $\text{Cr}_2\text{O}_3$ , will be discussed when relevant to discussions on oxides. Several authors have reported data on the  $\text{Fe}_x\text{Cr}_{2-x}\text{O}_3$  solid solution series [45, 46].

## Solid solutions

Solid solutions are mixtures of different pure compounds where the mixing occurs within the crystal lattice as opposed to crystals of one pure spinel mixed with crystals of the other pure spinel. A solid solution of  $\text{Mg}_{0.5}\text{Ni}_{0.5}\text{Cr}_2\text{O}_4$  is a normal spinel lattice with one half of the tetrahedral sites occupied by nickel and the remaining half occupied by magnesium. A solid solution is very different from a simple 50-50 physical mixture of pure  $\text{MgCr}_2\text{O}_4$  and  $\text{NiCr}_2\text{O}_4$ , as the latter contains two different normal spinel lattices: one with all of the tetrahedral sites occupied by nickel, and the other with all of the tetrahedral sites occupied by magnesium.

Vibrational data on spinels and solid solution spinels of the form  $\text{A}_x\text{B}_{1-x}\text{C}_y\text{D}_{2-y}\text{O}_4$  can give a tremendous amount of information regarding phonon dependencies on different elemental composition of the spinel lattice. Experimental data may support or refute current vibrational models.

Three different spinel solid solution series were synthesized and examined in the present work.  $\text{Mg}_x\text{Ni}_{1-x}\text{Cr}_2\text{O}_4$  was studied first because the cation substitution is relatively simple. Both  $\text{MgCr}_2\text{O}_4$  and  $\text{NiCr}_2\text{O}_4$  are normal spinels [47, 48]; only the tetrahedral divalent cation is being exchanged from  $\text{Ni}^{2+}$  to  $\text{Mg}^{2+}$ . This gave us an opportunity to examine the impact of the divalent cation on the vibrational modes.

The second synthesized series was  $\text{NiFe}_x\text{Cr}_{2-x}\text{O}_4$ . This series involves the substitution of the trivalent cation from Cr to Fe within the spinel lattice. In addition, the role of inversion upon the vibrational modes can be studied, as  $\text{NiFe}_2\text{O}_4$  is an inverse spinel [49].  $\text{Cr}^{3+}$  has the largest octahedral site preference of the three cations, but  $\text{Ni}^{2+}$  has a larger octahedral preferences than  $\text{Fe}^{3+}$  [50]. Because of the this, as the amount of iron,  $x$ , is increased, the series transitions from a normal spinel lattice to a completely inverse spinel lattice. In  $\text{NiFe}_2\text{O}_4$ , the  $\text{Ni}^{2+}$  cations occupy one half of the octahedral positions, and  $\text{Fe}^{3+}$  occupy the remaining half of the octahedral sites and

all of the tetrahedral sites. Mixed spinels of the form  $\text{NiFe}_x\text{Cr}_{2-x}\text{O}_4$  could be likely products in the corrosion of nickel-based alloys.

The third solid solution series studied in this work was  $\text{Fe}_x\text{Cr}_{3-x}\text{O}_4$ . This series is the most relevant to the corrosion research on iron-based stainless steels exposed to LBE.  $\text{FeCr}_2\text{O}_4$  is a normal spinel, and  $\text{Fe}_3\text{O}_4$  is an inverse spinel [51,52], so vibrational spectroscopy of this series can also investigate the role of lattice inversion on the vibrational modes.

### The Jahn-Teller effect

Some spinels exhibit slight distortions from the spinel structure. In many instances, this is due to the Jahn-Teller effect involving degenerate electron orbital energy states. The valence electrons of the transition metals fill various levels within the  $d$  orbitals. Jahn and Teller showed that a nonlinear molecule will distort along a vibrational coordinate to remove the orbital degeneracy of an electronic state [53]. Electrons that do not contribute to the molecular binding do not produce this distortion. The degeneracy is created by a crystal having multiple electronic configurations with the same energy. Dunitz and Orgel explain these Jahn-Teller distortions by applying crystal field theory to the spinel structure [54]. Their discussions of crystal field stabilization are applicable to comparing members of the same crystal structure and their arguments will be summarized.

In an octahedral or tetrahedral field, the energy levels of the  $d$  orbitals are split into a doublet,  $e_g$  ( $d_{x^2-y^2}$ ,  $d_{z^2}$ ), and a triplet,  $t_{2g}$  ( $d_{xy}$ ,  $d_{xz}$ ,  $d_{yz}$ ). In the octahedral arrangement, the  $e_g$  orbitals point directly at the anions, which causes destabilization. For this octahedral configuration, the  $e_g$  doublet has a higher energy than the  $t_{2g}$  triplet. The  $t_{2g}$  orbitals are more stable in this configuration because the orbitals point between the axes of the anions. For the tetrahedral configuration, the energy

levels are inverted: the  $t_{2g}$  orbitals have a higher energy than the  $e_g$  orbitals.

For the triply degenerate lower  $t_{2g}$  level of the tetrahedral configuration, a tetragonal distortion removes the degeneracy by splitting the energy levels into a singlet and a doublet. The new tetragonal unit cell has two lattice parameters,  $c$  and  $a$ , instead of just  $a$ , though the unit cell is redefined so that as it approaches cubic, the  $a$  parameter is equal to the lattice parameter of the spinel lattice divided by  $\sqrt{2}$ . For such comparisons to the cubic lattice, the  $c/a$  ratio of the distorted cell is often compared to this factor of  $\sqrt{2}$ . The energy level arrangement is determined by the  $c/a$  ratio of the tetragonal geometry.

Dunitz and Orgel further hypothesize that the distortion has no directional preference, and will be along any of the three coordinate axes, independent of the neighbors of the tetrahedral or octahedral unit [54]. This randomness indicates that the overall lattice still appears cubic, though the x-ray diffraction peaks may be broadened. However, as the temperature is lowered, the interaction between neighboring distortions becomes more significant, and a transition temperature exists distortions occur in a single direction.

An excellent example of the Jahn-Teller effect in spinels is  $\text{Ni}^{2+}$  in the tetrahedral configuration.  $\text{Ni}^{2+}$  in the tetrahedral configuration has eight electrons in the  $d$  orbitals. The lower  $e_g$  doublet is completely filled with four electrons, but the upper  $t_{2g}$  triplet will be degenerate because there are three orbitals for the four remaining electrons. After an electron occupies each triplet level, a single remaining electron is available to occupy any of the three orbitals of this triplet, all of which have the same energy. This degeneracy is lifted by elongating the bonds along the z-axis. As a result, the  $d_{xy}$  orbital becomes a single lower-energy, non-degenerate state occupied by the single remaining electron.

Nickel is mentioned because  $\text{NiCr}_2\text{O}_4$  was studied and a Jahn-Teller distortion of

the lattice is expected. This distortion to the  $I4_1/amd$  space group will be discussed with the results of  $\text{NiCr}_2\text{O}_4$ . Another nickel spinel studied in the present work,  $\text{NiFe}_2\text{O}_4$ , is a completely inverse spinel structure, in which the  $e_g$  doublet of  $\text{Ni}^{2+}$  in an octahedral configuration contains a single electron in each level, indicating the absence of a Jahn-Teller distortion for  $\text{NiFe}_2\text{O}_4$ .

$\text{Cr}^{3+}$  has five electrons in the  $d$  orbital. In either the octahedral or tetrahedral configuration, there will be one electron filling each of the  $e_g$  and  $t_{2g}$  orbitals. This configuration has no degeneracy, and thus there is no Jahn-Teller distortion for  $\text{Cr}^{3+}$  in the octahedral site.

$\text{Fe}^{2+}$  and  $\text{Fe}^{3+}$  have 6 and 5 electrons, respectively, when bonded in a tetrahedral or octahedral configuration. A 5-electron configuration has no Jahn-Teller distortion in either the tetrahedral or octahedral configuration. For the 6 electrons of  $\text{Fe}^{2+}$  in the octahedral configuration, the degeneracy exists in the mostly non-bonding  $t_{2g}$  orbitals, leading to only small Jahn-Teller distortions. Likewise, in the tetrahedral configuration, the degeneracy occurs in the  $e_g$  orbitals, which are mostly non-bonding. Any Jahn-Teller distortion due to iron in the octahedral or tetrahedral sites will be too small to detect [54].

### X-ray diffraction

The atoms within a crystal lattice form regular planes with spacing  $d$  between each plane. Coherent x-rays incident upon these regular planes can reflect off these planes and constructively interfere if the path length difference is a multiple of the wavelength of the light. Knowing the angle at which the light scatters from these planes allows determination of the distance between each plane. Many different planes may exist in a regular crystal lattice, defined by coplanar atoms in the various crystal sites throughout the lattice. The incident x-rays will therefore be capable of scattering

off all these planes which leads to constructive interference at many different angles. Information about the crystal structure can be determined from this diffraction pattern.

The spacing between atomic planes,  $d$ , is determined using Bragg's law,

$$2d \sin \theta = m\lambda, \quad (2.4)$$

where  $\theta$  is the angle between the incident light and the lattice planes,  $m$  is an integer describing the order, and  $\lambda$  is the wavelength of the incident light. X-rays are used because, to achieve measurable diffraction, the wavelength must be on the order of  $d$ . Because the x-ray diffraction (XRD) spectrum and structure of spinel are well known, the lattice parameter can be calculated by knowing the Miller indices of each spinel diffraction peak.

Miller indices are reciprocal fractions along each dimension that define a plane within the lattice, and are commonly denoted as three numbers,  $hkl$ , that represent the fraction in each dimension of the lattice. For the cubic system, the dimensions are the standard cartesian coordinates  $x, y, z$ . For example, the (100) represents a plane in the  $yz$  plane. The (200) surface would be a  $yz$  plane halfway along the  $x$  dimension of the crystal.

For a cubic lattice, the diffraction spacing,  $d$ , can be related to the lattice parameter,  $a$ , and the Miller indices,  $(hkl)$ , by

$$d = \frac{a}{\sqrt{h^2 + k^2 + l^2}} \quad (2.5)$$

Intensities of the x-ray diffraction peaks are affected by many variables such as the electron distribution around any atom or ion and the structure of the crystal. Scattering of the x-rays occur from the electron cloud surrounding the atom or ion, and therefore the intensities are a sum of all scattering from the electron cloud. Because the spacing within the electron cloud is smaller than the wavelength of the



incident x-ray, partially destructive interference occurs from the sum, and an atomic scattering factor,  $f_0$ , can be calculated for atoms and ions. The structure factor,  $F_{hkl}$ , describes how the atomic arrangement of the crystal affects the x-ray diffraction peaks. The Rietveld refinement method, named for Hugo Rietveld who developed the method, incorporates all of the variables that affect diffraction peaks, and involves a least squares fit to refine structural information of the sample [55].

X-ray diffraction is a common and powerful tool for determining the crystal structure of a material. However, sample preparation is crucial, and the technique cannot examine all varieties of samples. The sample must be a single crystal, a uniform surface, or a powder, all of which require long-range order for coherent x-ray diffraction. Vibrational spectroscopy can thus be a more practical approach to the study of corrosion layers upon a steel, or any non-uniform sample, because it is a more local probe.

## CHAPTER 3

### RAMAN SCATTERING AND INFRARED ABSORPTION

The Raman effect, named for the Nobel prize work by Chandrasekhra Venkata Raman in 1928 [56], is an inelastic light scattering effect resulting from the excitation or de-excitation of vibrational modes. In the simple case of a single molecule, Figure 3, an incident photon can either scatter elastically, known as Rayleigh scattering, or scatter inelastically and excite or absorb a vibrational mode of the molecule. In a crystal lattice, the photon may scatter from a lattice phonon that will change the energy of the phonon. The energy loss or gain of the inelastically scattered photon corresponds to the energy of a vibrational level, or phonon level, of the system. If a phonon is created at a higher energy state, then the scattered photon will have less energy than the incident photon. Alternatively, a phonon can be annihilated, resulting in a scattered photon having greater energy than the incident photon.

Raman scattering is a phenomenon with a low probability of occurrence. Only one in  $10^6$  of incident photons is inelastically scattered. Because the majority of incident light is Rayleigh scattered, Raman detector systems must remove this elastically scattered light from the collected light, or else the Rayleigh scattered light can overwhelm the weaker Raman signal.

Raman scattering is typically performed non-resonantly, meaning that the energy of the incident photons does not equal any energy difference between any phonon levels of the lattice. In the most common conceptual description, the photon excites the system to a virtual state before decaying to the ground state (Rayleigh) or an

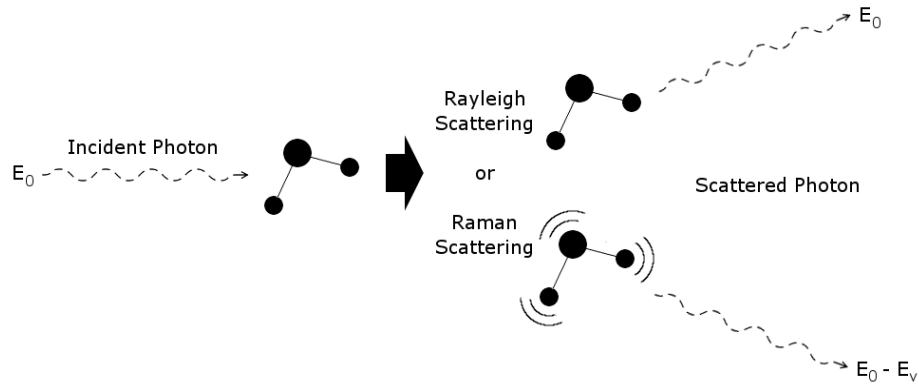


Figure 3. The cartoon displays Rayleigh and Raman scattering processes. An incident photon can either scatter elastically or inelastically from a molecule. Most often, the inelastic process results in a vibrating molecule and a photon of less energy [56].

excited vibrational state (Raman). This can be seen in Figure 4.

Stokes scattering and anti-Stokes scattering are the terms applied to whether a phonon is created or annihilated, respectively. Anti-Stokes scattering is a much weaker effect than Stokes scattering. All Raman data collected in this study, used for purposes of determining peak positions, are Stokes signals, corresponding to scattered photons of lower energy than the incident photons.

### Raman Scattering

In a classical approach [35], the oscillating electric field  $E$  of the incident light with frequency  $\nu_0$  and amplitude  $E_0$  can be written as

$$E = E_0 \cos 2\pi\nu_0 t. \quad (3.1)$$

This electric field interacts with and distorts the electron cloud of the lattice, inducing an electric dipole  $P$  given by

$$P = \alpha E, \quad (3.2)$$

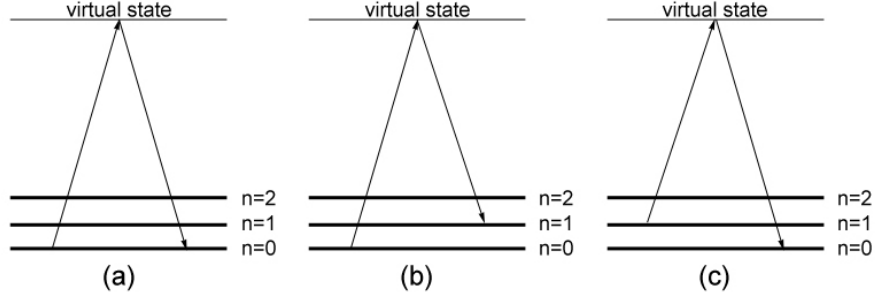


Figure 4. (a) Rayleigh scattering - absorption and re-emission of a photon of identical energies. (b) Stokes - Raman scattering involving the emission of a photon of lower energy than the absorbed photon. The vibration level  $n = 1$  becomes excited. (c) Anti-Stokes - Raman scattering involving the emission of a photon having greater energy than the absorbed photon. The vibrational level  $n = 1$  was initially occupied.

where  $\alpha$  is the polarizability of the lattice.

If the lattice is vibrating with frequency  $\nu_m$  and amplitude  $q_0$ , then the nuclear displacement can be written as

$$q = q_0 \cos 2\pi\nu_m t. \quad (3.3)$$

For small amplitudes,  $\alpha$  is a linear function of  $q$ , and can be expanded as

$$\alpha = \alpha_0 + \left( \frac{\partial \alpha}{\partial q} \right)_0 q + \dots, \quad (3.4)$$

where the partial derivative is evaluated at the equilibrium nuclear position.

Combining equations 3.1, 3.2, 3.3, and 3.4 gives

$$\begin{aligned}
P &= \alpha E_0 \cos 2\pi\nu_0 t \\
P &= \alpha_0 E_0 \cos 2\pi\nu_0 t + \left(\frac{\partial\alpha}{\partial q}\right)_0 q E_0 \cos 2\pi\nu_0 t \\
P &= \alpha_0 E_0 \cos 2\pi\nu_0 t + \left(\frac{\partial\alpha}{\partial q}\right)_0 q_0 E_0 \cos 2\pi\nu_0 t \cos 2\pi\nu_m t \\
P &= \alpha_0 E_0 \cos 2\pi\nu_0 t \\
&\quad + \frac{1}{2} \left(\frac{\partial\alpha}{\partial q}\right)_0 q_0 E_0 [\cos\{2\pi(\nu_0 + \nu_m)t\} + \cos\{2\pi\nu_0 - \nu_m)t\}], \tag{3.5}
\end{aligned}$$

where the first term on the right side of the equality in Equation 3.5 is the Rayleigh scattering term, which has a frequency equal to the incident frequency,  $\nu_0$ . The Stokes and anti-Stokes terms, having frequencies shifted from the incident frequency, are  $\nu_0 - \nu_m$  and  $\nu_0 + \nu_m$ , respectively. The partial derivatives of the polarizability act as coefficients for the Stokes and anti-Stokes terms, thus indicating that these Raman terms are non-zero only if there is a change in the polarizability ( $\partial\alpha/\partial q \neq 0$ ) when the molecule vibrates. If the polarizability does not change during a vibration, this coefficient is zero, and the vibration is not Raman-active.

### Polarizability tensor

Electron clouds are three-dimensional entities, and an incident electric field can induce a dipole in directions perpendicular to the direction of polarization. Therefore, Equation 3.2 must be a tensor to incorporate the  $x$ ,  $y$ , and  $z$  directions. In matrix form, this equation can be written as

$$\begin{pmatrix} P_x \\ P_y \\ P_z \end{pmatrix} = \begin{pmatrix} \alpha_{xx} & \alpha_{xy} & \alpha_{xz} \\ \alpha_{yx} & \alpha_{yy} & \alpha_{yz} \\ \alpha_{zx} & \alpha_{zy} & \alpha_{zz} \end{pmatrix} \begin{pmatrix} E_x \\ E_y \\ E_z \end{pmatrix}, \tag{3.6}$$

where the  $3 \times 3$  matrix on the right side of Equation 3.6 is called the *polarizability tensor*,  $\alpha_{ij}$ . The polarizability tensor is symmetric, obeying

$$\alpha_{ij} = \alpha_{ji}. \tag{3.7}$$

If any of the components of this tensor change during a vibration, the vibration is Raman-active. The intensities of the Raman fundamentals are therefore determined by  $\partial\alpha_{ij}/\partial Q$  where  $Q$  is a normal coordinate of the lattice. Even though  $\alpha_{ij}$  is symmetric,  $\partial\alpha_{ij}/\partial Q$  may not be symmetric.

Approaching Raman scattering using quantum mechanics requires the use of the Kramers-Heisenberg formula for a two-photon scattering process [36]. The virtual state that the system transitions to is unknown, and so all virtual states must be summed over. In addition, the excitation to and relaxation from the virtual state occurs simultaneously. This Kramers-Heisenberg formula can be shown to be related to the classical polarizability tensor.

#### Infrared absorption

A quantum mechanical treatment [36] of the vibrations of a crystal as a harmonic oscillator shows that phonon energies are quantized, with

$$E_i = (n_i + \frac{1}{2})h\nu_i, \tag{3.8}$$

where  $n_i$  is the quantum number and  $\nu_i$  is the normal frequency associated with the normal coordinate  $Q_i$  [34].

A crystal is capable of directly absorbing a photon that corresponds to an energy of vibration, given in Equation 3.8. Because photons are polarized, the electric field of the photon must be capable of interacting with the vibration. An electric field will create a force on charged particles, such as the positive and negative ions constituting the crystal. As the electric field points in one direction, the electric dipole may be stretched along an axis of the crystal. As the electric field points in the opposite direction, the electric dipole becomes compressed. This results in a vibration of the system. This photon-dipole interaction leads to the selection rule for infrared absorption. Vibrations are infrared-active if there is a change in the dipole moment

during the vibration. If the dipole is not changed during the vibration, an incident photon will not be capable of exciting the vibration.

### Wavenumbers

Raman and infrared spectra are often plotted as intensity versus wavenumber ( $\text{cm}^{-1}$ ). A wavenumber can easily be calculated from a known light frequency  $\nu$ , using

$$\text{wavenumber} = \frac{1}{\lambda} = \frac{\nu}{c} \text{ (cm}^{-1}\text{)} \quad (3.9)$$

where  $\nu$  is the frequency of the photon, and  $c$  is the speed of light in a vacuum,  $2.998 \times 10^{10}$  cm/s.

For Raman spectra, the wavenumber shift relative to the wavenumber of the incident laser is usually plotted. This Raman shift,  $\bar{\nu}$ , can be calculated in wavenumbers using

$$\bar{\nu} = \frac{\Delta\nu}{c} = \frac{\nu_i - \nu_s}{c} \quad (3.10)$$

where  $\nu_i$  and  $\nu_s$  are the frequencies of the incident and scattered photons, respectively. The Raman shift is the difference between the wavenumbers of the Raman-scattered photon and the Rayleigh-scattered photon.

## CHAPTER 4

### PREVIOUS WORK

The present work was partly motivated by an ambition to augment the results from our group on the LBE-corroded steels acquired with scanning electron microscopy (SEM), energy dispersive x-ray spectroscopy (EDX), and x-ray photoelectron spectroscopy (XPS) done before, and in parallel, with the present work [57–59]. The work then expanded into a more comprehensive account of the vibrational properties of the spinel system, as uncertainty regarding the assignment of the vibrational modes of spinel is apparent. As such, a summary of the previous work from our research group will be presented, as well as a summary of the large amount of experimental data and theoretical models on the vibrational modes of the spinel lattice. Doing so will highlight the gaps in knowledge that the present work will attempt to complete.

#### LBE-corroded steels

Our previous work characterized the compositional and morphological properties of the corrosion layers of stainless steel samples exposed to lead-bismuth eutectic (LBE) [57–59]. One of the conclusions was that the surface treatment of the steel was crucial to reducing the severity of corrosion damage sustained by the steel [59]. Cold-rolling the surface of the stainless steel leads to a better preservation of the chromium oxide layer.

SEM images from our previous work also clearly show that at least two corrosion layers are formed during the corrosion process on these steels exposed to LBE [57]. A cross-section SEM image of a LBE-corroded stainless steel sample is shown in



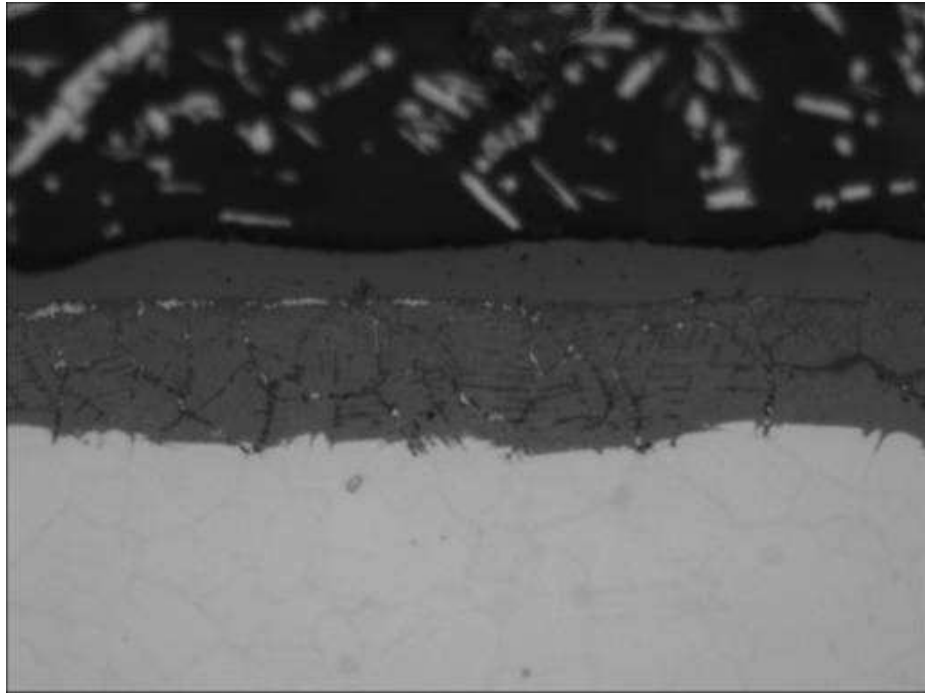


Figure 5. SEM image of a cross section cut from a stainless steel. A dual oxide layer is visible [60].

Figure 5. The outer oxide layer grows outwards from the original surface, while the inner oxide layer grows inwards.

In energy dispersive x-ray spectroscopy (EDX), the sample is bombarded by electrons, and the resulting characteristic x-rays emitted by the sample are used to produce an elemental map of the sample. Different SEM images highlighting the elemental composition of the corrosion layers are shown in Figure 6. The image proves that the outer corrosion layer contains only iron and oxygen, while the inner layer also contains chromium. Nickel is enhanced in the inner oxide layer compared to the bulk metal.

In x-ray photoelectron spectrometry (XPS), the sample is bombarded by x-rays, and the energies of the resulting photoelectrons from the top few atomic layers are

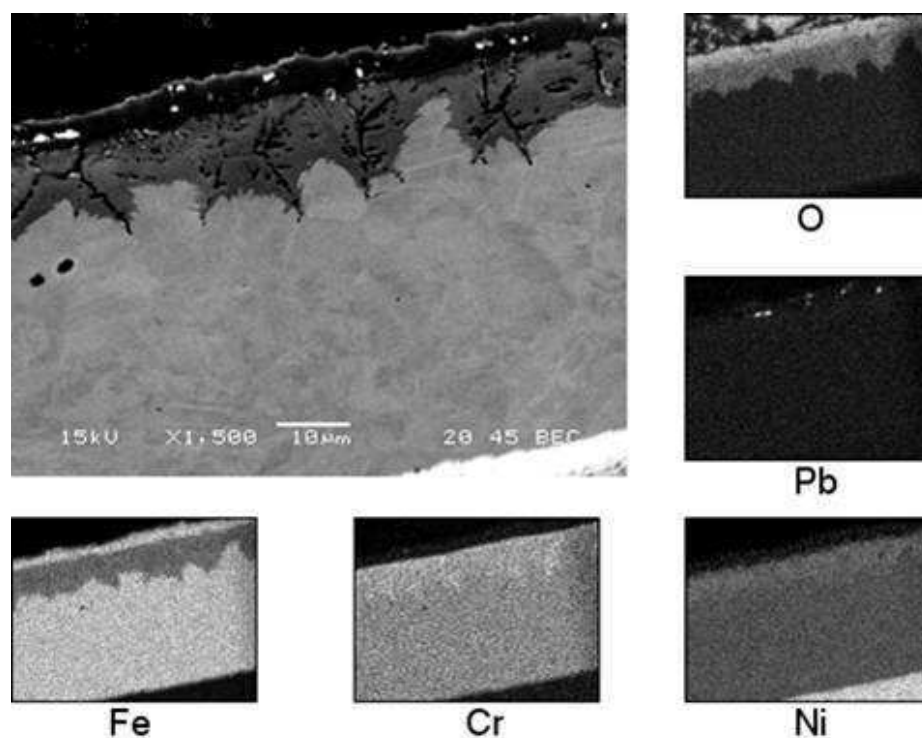


Figure 6. SEM image using the elemental mapping capabilities of EDX [60].

analyzed. XPS is capable of determining oxidation states of elements, which can give clues to the molecular species existing within a sample. In previous work by our group, XPS studies of LBE-corroded steels observed that iron and chromium are oxidized, while the nickel within the inner corrosion layer is metallic [60].

As powerful as SEM, EDX, and XPS techniques are, structural and chemical ambiguities can remain. These techniques can accurately identify the existence of iron, chromium, oxygen, and other elements within the corrosion layer, but cannot accurately differentiate between  $\alpha$ - $\text{Fe}_2\text{O}_3$ ,  $\text{Fe}_3\text{O}_4$ , or other oxidation products. Fortunately, vibrational spectroscopy is a technique capable of determining the vibrational modes of a solid, and these vibrational modes are strongly dependent of the crystal symmetry.

## Identifying corrosion layers using Raman spectroscopy

Many researchers have used Raman spectroscopy to study the corrosion layers on alloys exposed to a variety of extreme conditions. The common method to identify corrosion products is to compare Raman spectra of the unknown corrosion layers with the known spectra of standard oxide compounds, such as  $\alpha$ -Fe<sub>2</sub>O<sub>3</sub>, Fe<sub>3</sub>O<sub>4</sub>, Cr<sub>2</sub>O<sub>3</sub>, and other compounds [25,61–65]. The best-matching spectral “fingerprint” then identifies the chemical species within the corrosion layer.

For example, Cunha et al. studied the oxides formed on 316L stainless steel in a high-temperature pressurized water reactor environment and determined the corrosion layer to be composed of spinels of nickel, iron, and chromium [24]. Kim et al. studied NiCr<sub>2</sub>O<sub>4</sub> and NiFe<sub>2</sub>O<sub>4</sub> powders to identify corrosion layers of a nickel-based alloy in a high-temperature water environment [64]. Renush et al. examined the corrosion layers on Fe-Cr-Ni alloys at various temperatures and reported the formation of  $\alpha$ -Fe<sub>2</sub>O<sub>3</sub>, Fe<sub>3</sub>O<sub>4</sub>, and Cr<sub>2</sub>O<sub>3</sub> [66]. Boucherit et al. examined Fe and Fe-Mo alloys and observed evidence of spinel layers formed over the bulk iron [67]. Gardiner et al. identified the spinel and corundum phases in the corrosion layers formed on Fe-Cr stainless steels [25]. Other studies have shown evidence of the formation of spinels such as FeCr<sub>2</sub>O<sub>4</sub> [68] and MnCr<sub>2</sub>O<sub>4</sub> [30,69] as corrosion products.

All of these studies, with the exception of Cunha et al. [24], assumed that the corrosion products identified are pure end-member chromites and ferrites, as opposed to a solid solution of two or more end-member oxides containing iron, nickel, chromium, or other elements from the alloy. The use of Raman spectroscopy to identify solid solutions requires a database of experimentally measured Raman spectra of standard compounds.

## Theoretical work of the spinel system

A database of experimentally measured Raman spectra of standard compounds is valuable for identifying chemical species, but a purely experimental database would suffer from some definite limitations. There are a very large number of possible solid solutions, and accordingly, a purely empirical approach is a large undertaking. The development and testing of theoretical models of such solid solutions can lead to insight and the recognition of series regularities. Many researchers have worked to develop and use models to calculate the vibrational modes of spinels [8,70–77]. Such calculations can provide crucial support in the assignment of vibrational modes as correct calculations could predict frequencies, intensities, and atomic motions of the vibrations of solid solution spinel systems.

Before the development of computers to perform calculations, researchers used group theory to investigate the vibrations of spinel. In early work, Waldron assumed the primitive cell of spinel was composed of two tetrahedral  $AO_4$  units and a  $B_4$  unit [78]. The nearest-neighbor interactions from the octahedral cations were assumed to be small and ignored. This approach allowed all of the vibrations to be identified from the  $T_d$  point group of the  $AO_4$  tetrahedron. The interaction between neighboring tetrahedral units was also assumed to be small. This approach predicts eight infrared-active  $F_2$  modes, however only four distinct infrared-active modes are typically reported for spinels.

White et al. approached the spinel lattice with a group theoretical analysis of the spinel unit cell [38]. Their method predicted the observed four infrared and five Raman-active modes. They assumed the atomic motions derived from Waldron’s two  $AO_4$  and  $B_4$  units. Verble employed a similar approach in a study of  $Fe_3O_4$  [79], which includes diagrams of the vibrations. Similar to the models by Waldron and White et al., the octahedral cations remain at rest during all vibrations. Similar calculations of

the atomic motions were performed by Yamanaka et al. in a study of the vibrations of  $\gamma$ -Ni<sub>2</sub>SiO<sub>4</sub> [8].

Vibrations of spinel sulfides and selenides ACr<sub>2</sub>X<sub>4</sub>, with X being S or Se, mainly chalcogenides, with A being Cd, Fe, Mn, and Zn, were calculated by Gupta et al. [73–75] who find the B-X interaction to dominate the A-X interaction. Gupta et al. and also Sinha, in a study of chromites, support the hypothesis that the B-O interaction is more important than the A-O interaction [77,80]. Recently, Kushawaha et al. have performed calculations on several chromites, ACr<sub>2</sub>O<sub>4</sub>, with A = Co, Mn, Zn [81,82]. They report stronger interactions for the octahedral B-O bond than the tetrahedral A-O bond. However, work by Sinha et al. has shown stronger A-O force constants for MgAl<sub>2</sub>O<sub>4</sub> and ZnCr<sub>2</sub>O<sub>4</sub> [83].

Wakamura et al. performed calculations to model the behavior of Zn<sub>1-x</sub>Cd<sub>x</sub>Cr<sub>2</sub>S<sub>4</sub> [84]. The low-frequency mode  $\nu_4$  was observed to have a large discontinuity in wavenumber as zinc was substituted for cadmium. They concluded that the behavior of this mode results from large differences in the force constants of the two end members.

### Assignment of the vibrations of spinel

The literature is inconsistent with regard to the assignment of the specific atomic motions within the spinel lattice during the Raman-active vibrations. However, the common atomic motions assigned to the vibrations of spinel from the literature will be summarized.

The highest-frequency A<sub>1g</sub> mode is assigned as the symmetric breathing mode of the AO<sub>4</sub> unit within the spinel lattice [7, 8, 79]. The oxygen atoms move away from the tetrahedral cation along the direction of the bonds. Neither the tetrahedral nor octahedral cations are in motion during this vibration.

The second highest-frequency Raman-active mode is the  $F_{2g}(3)$  mode. The literature disagrees about the assignment of atomic motions during the vibration, which has been reported as either the antisymmetric breathing mode of the  $AO_4$  unit [8, 79], or as an asymmetric bending motion of the oxygens bonded to the tetrahedral cation [7].

The  $F_{2g}(2)$  mode was shown by Verble to be a translation along one direction of the lattice, with the cation and oxygen atoms moving in opposite directions [79]. Verble also assigns the  $E_g$  mode as a symmetric bending motion of the oxygen anions within the  $AO_4$  unit [79]. This assignment is supported by other researchers [14, 85]. Most of the literature agrees that the lowest-frequency Raman-active mode,  $F_{2g}(1)$ , is a complete translation of the  $AO_4$  unit within the spinel lattice [8, 14, 79, 85, 86].

There is very little discussion of the motion of the octahedral cations during these vibrations. This results from the assumption that the simplest unit of the spinel lattice is composed of two  $AO_4$  tetrahedra and a  $B_4$  tetrahedron. Many researchers seem to use this assumption in assigning all vibrational modes to motions involving solely the  $AO_4$  unit [7, 8, 79, 87]. The octahedral cations are assumed to remain at rest. Every oxygen atom is bound to three octahedral cations and only a single tetrahedral cation. Even if the cation remains at rest, the bonding force between octahedral cations and the oxygen atoms must be relevant for determining phonon energies.

However, as Preudhomme et al. have shown with extensive experimental data in their series of infrared studies on spinels, the assumption that the higher-frequency vibrations depend solely upon the tetrahedral cations may be incorrect, at least for the normal II-III spinels, and instead depend more strongly on the nature of the octahedral cation [88].

Marinković Stanojević et al. assign many vibrations to octahedral cations in their study of  $ZnCr_2O_4$  [89]. All high-frequency modes, Raman and infrared, are assigned to vibrations involving the  $CrO_6$  octahedron, and the low-frequency modes are assigned

to the  $\text{ZnO}_4$  tetrahedron. The  $A_{1g}$  mode is assigned to the symmetric breathing mode of the octahedral unit. The Raman-active  $E_g$  mode is assigned as a complex vibration involving both zinc and chromium atoms. The lowest-frequency infrared-active mode,  $\nu_4$ , is assigned as a bending mode of the chromium octahedron.

Laguna-Bercero et al. studied the  $\text{NiAl}_2\text{O}_4$  inverse spinel and argued that the  $A_{1g}$  mode depends upon the octahedral cations [41]. They predict that the complicated  $A_{1g}$  mode is due to the random occupation of the octahedral sites by the  $\text{Ni}^{2+}$  and  $\text{Al}^{3+}$  cations. The possible configurations lead to slight differences in the energies of this vibrational mode, creating the multiple  $A_{1g}$  modes.

Hwang et al. examined chromium substituted  $\text{LiMn}_2\text{O}_4$ , a spinel containing both  $\text{Mn}^{3+}$  and  $\text{Mn}^{4+}$  in the octahedral sites [90].  $\text{Li}^{2+}$  occupies all tetrahedral sites. They interpret the two  $A_{1g}$  modes as resulting from tetragonally distorted  $\text{Mn}^{3+}\text{O}_6$  and undistorted  $\text{Mn}^{4+}\text{O}_6$  octahedra.

Additional modes may appear in vibrational spectra due to local distortions of the crystal lattice. These defects do not affect the long-range ordering of the system, and are often undetectable by x-ray diffraction. However, vibrational spectroscopy is very sensitive to these defects. The additional modes due to local distortions of the lattice are known as *local* modes.

Preudhomme et al. argued that, as the cations are exchanged in these mixed spinel systems, there are three different ways that the vibrational modes can vary [91]. They define the terms *localized* and *complex* to describe two behaviors, with a third being a combination of localized and complex. The term *localized* can be confused with the common usage of *local* modes, as described above. Chang et al. define the terms *one-mode behavior* and *two-mode behavior* [92] to describe the same phenomena that Preudhomme et al. emphasized, which have become more common in the literature.

One-mode behavior describes phonons in mixed systems that vary continuously

from the frequency of one end member to the frequency of the other end member. Alternatively, two-mode behavior of a mixed crystal system possesses two distinct vibrational modes, close to the frequency of both end members, with intensities proportional to the fraction of each pure member within the mixed system. Both one- and two-mode behavior can occur where the two distinct modes also shift in frequency upon cation substitution. Two-mode behavior may be evidence of local crystallization of the two end members within the sample. This may occur on a scale small enough to not be resolvable using x-ray diffraction.

#### Experimental work on the spinel vibrations

Many Raman studies of pure spinel oxides,  $AB_2O_4$ , have appeared in the literature. The wavenumbers of the five Raman-active modes for various spinel oxides are shown in Table 3. These data allow investigation of the Raman-active modes for any patterns due to replacement of the tetrahedral and octahedral cations.

The chromites are all normal II-III spinels and vary only by the divalent cation occupying the tetrahedral sites.  $Cr^{3+}$  has a greater preference for the octahedral site than other cations [50, 103]. The  $A_{1g}$  mode for all chromites, with the exception of cadmium, varies significantly less than the other Raman-active modes. This could indicate that this mode is mostly independent of the divalent cation species. The change in the  $A_{1g}$  mode for  $CdCr_2O_4$  from the other chromites is only approximately 7%. The  $F_{2g}(1)$  mode seems to have a much greater dependence on the divalent cation: The  $F_{2g}(1)$  modes of  $CdCr_2O_4$  and  $MgCr_2O_4$  differ by approximately 40%.

The  $F_{2g}(2)$  and  $F_{2g}(3)$  modes of  $CdCr_2O_4$  are similar to the other chromites, even with the much heavier cadmium atom occupying the octahedral site. The  $F_{2g}(1)$ ,  $E_g$ , and  $A_{1g}$  modes are all lower than the respective modes of the other chromites.

Many of the ferrites exhibit inversion of the cations between the tetrahedral and



Spinel	F <sub>2g</sub> (1)	E <sub>g</sub>	F <sub>2g</sub> (2)	F <sub>2g</sub> (3)	A <sub>1g</sub>
<i>Chromites</i>					
CdCr <sub>2</sub> O <sub>4</sub> [93]	134	343	499	600	647
CoCr <sub>2</sub> O <sub>4</sub> [81]		454			692
CuCr <sub>2</sub> O <sub>4</sub> [94]	190			623	680
FeCr <sub>2</sub> O <sub>4</sub> [45]					686
MgCr <sub>2</sub> O <sub>4</sub> [48]	227	447	544	614	687
MnCr <sub>2</sub> O <sub>4</sub> [76, 80]		457	511	600	671,685
NiCr <sub>2</sub> O <sub>4</sub> [47]	181	425	511	580	686
ZnCr <sub>2</sub> O <sub>4</sub> [93, 95]	180	430,457	511	605	687
<i>Ferrites</i>					
CoFe <sub>2</sub> O <sub>4</sub> [96]	210	312	470	576	624 <i>sh</i> , 695
MgFe <sub>2</sub> O <sub>4</sub> [97]	217	333	486	554	646, 715
Fe <sub>3</sub> O <sub>4</sub> [51]	193	306		538	668
NiFe <sub>2</sub> O <sub>4</sub> [64]			460 <i>sh</i> , 492	574 <i>sh</i> , 595	654 <i>sh</i> , 702
ZnFe <sub>2</sub> O <sub>4</sub> [98]	221	246	355	451	647
<i>Aluminates</i>					
CoAl <sub>2</sub> O <sub>4</sub> [99]	201			516	615
MgAl <sub>2</sub> O <sub>4</sub> [87]	311	410	492	671	772
ZnAl <sub>2</sub> O <sub>4</sub> [100]	197	417	509	658	758
<i>Other Spinel</i>					
CoCo <sub>2</sub> O <sub>4</sub> [101]	194	482	522	618	691
ZnGa <sub>2</sub> O <sub>4</sub> [102]		638	467	611	714

Table 3. Compiled Raman data from the literature on AB<sub>2</sub>O<sub>4</sub> spinels. Shoulders of peaks are marked with *sh*. Data from the present work are not included.

octahedral sites.  $\text{NiFe}_2\text{O}_4$  and  $\text{Fe}_3\text{O}_4$  are completely inverse spinels [104].  $\text{MgFe}_2\text{O}_4$  has an inversion parameter of  $\xi = 0.90$  [105, 106]. At ambient conditions,  $\text{CoFe}_2\text{O}_4$  has an inversion parameter of  $\xi = 0.95$  [96]. Raman spectra of these inverse spinels is more complicated and show additional Raman-active modes over the five predicted by group theory.

Unlike the other ferrites in Table 3,  $\text{ZnFe}_2\text{O}_4$  is a normal spinel [18]. However, nanostructured powders of various synthesis and treatment methods have exhibited differing degrees of inversion [107]. As a normal spinel,  $\text{ZnFe}_2\text{O}_4$  can be compared to  $\text{ZnCr}_2\text{O}_4$  to examine the effect of only replacing the octahedral cation on the Raman-active modes. The  $A_{1g}$  mode is located at  $647\text{ cm}^{-1}$ , a much greater departure from any of the  $A_{1g}$  modes of the other chromites, with the exception of  $\text{CdCr}_2\text{O}_4$ . This suggests that the  $A_{1g}$  mode has a greater dependence upon the octahedral trivalent cation than the tetrahedral divalent cation.  $\text{MgAl}_2\text{O}_4$  and  $\text{MgCr}_2\text{O}_4$  can also be compared as both are normal spinels and differ only by the octahedral cation. The  $A_{1g}$  mode of  $\text{MgAl}_2\text{O}_4$  has a 12% greater frequency than the  $A_{1g}$  mode of  $\text{MgCr}_2\text{O}_4$ .

The  $E_g$ ,  $F_{2g}(2)$ , and  $F_{2g}(3)$  modes of  $\text{ZnFe}_2\text{O}_4$  differ greatly from the other chromites and ferrites. However, Wang et al. made these assignments from powder samples [98], and the assignments need confirmation by polarization studies on a single crystal sample.

The wavenumber of the  $A_{1g}$  mode varies more strongly among the ferrites than the chromites. If this mode is dependent only on the  $\text{AO}_4$  unit of the lattice, the frequency should be nearly identical for all ferrites, because they, with the exception of  $\text{ZnFe}_2\text{O}_4$ , are inverse spinels with  $\text{Fe}^{3+}$  in the tetrahedral position. From these compiled results on chromite and ferrites, the  $A_{1g}$  mode appears to depend more on the octahedral cation than the tetrahedral cation. The  $F_{2g}(1)$  mode remains similar to the other ferrites, as well as the chromites. The other three modes,  $E_g$ ,  $F_{2g}(2)$ , and

$F_{2g}(3)$ , are dramatically lower than the corresponding modes in any of the chromites.

Figure 7 is a plot of the wavenumbers of the Raman-active modes from the literature, versus the reciprocal of the square root of the mass of the tetrahedral cation for various chromites in the literature. This simple “mass on a spring” model predicts a wavenumber proportional to the reciprocal of the square root of the cation mass. The data show a linearly increasing Raman shift for the  $F_{2g}(1)$  and  $F_{2g}(2)$  modes. The wavenumber of the  $A_{1g}$  and  $E_g$  phonons remain mostly constant, with only cadmium chromite having a significantly smaller frequency. The  $F_{2g}(3)$  mode shows no overall dependence on the mass of the tetrahedral cation. Malavasi et al. create a similar plot for what they label “peak 2” of some normal  $AMn_2O_4$  spinels, where  $A = Mn, Mg,$  and  $Zn$  [108]. The wavenumber of this mode is in the  $470\text{-}510\text{ cm}^{-1}$  range, which suggests that it may be the  $F_{2g}(2)$  mode. If this assignment is correct, it is consistent with the behavior of the  $F_{2g}(2)$  mode for the chromites with different tetrahedral composition.

Figure 8 is a plot of the wavenumbers of the  $A_{1g}$  modes versus the reciprocal of the square root of the octahedral cation mass for various  $MgB_2O_4$  and  $ZnB_2O_4$  spinels. The figure shows a similar dependence upon substitution of the octahedral cation within the normal spinel lattice. Only  $ZnGa_2O_4$  breaks the trend seen in both plots.  $MgFe_2O_4$ , unlike the other spinels plotted in Figure 7, is an inverse spinel. However, Wang et al. report an unidentified peak at  $646\text{ cm}^{-1}$  on the low frequency side of the  $A_{1g}$  mode, similar to the shoulder of the  $A_{1g}$  mode on  $NiFe_2O_4$ . This data point is included to test the validity of the common interpretation that shoulders on the  $A_{1g}$  mode of the inverse spinels are due to the two distinct octahedra formed by the divalent and trivalent cations occupying the octahedral site of the inverse spinel lattice. The  $MgFe_2O_4$  data are consistent with this argument, as assigning the  $646\text{ cm}^{-1}$  mode to the  $A_{1g}$  behavior of the  $FeO_6$  unit in the inverse lattice agrees very

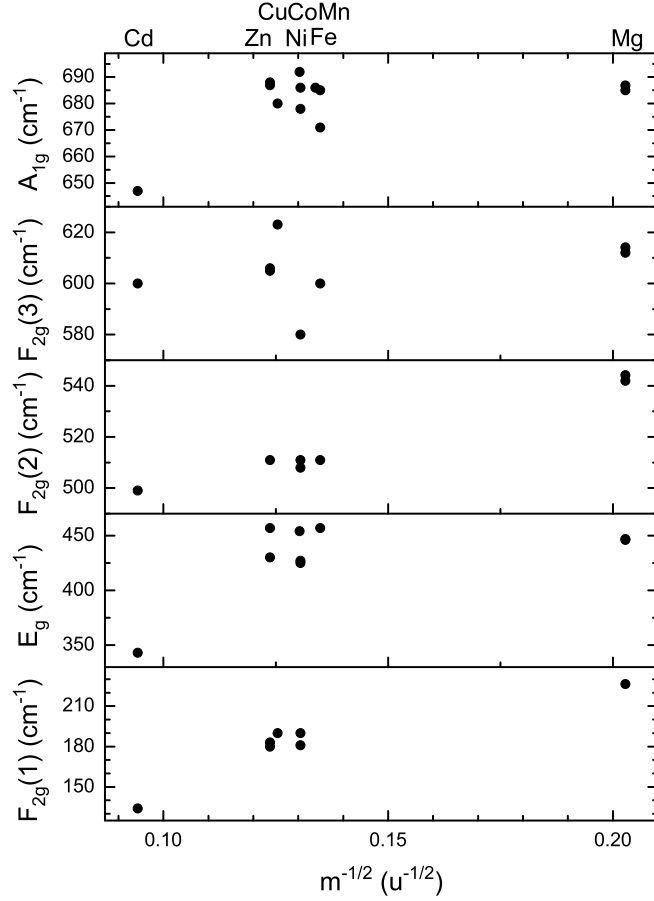


Figure 7. The wavenumbers of the Raman-active modes, from the literature, of various chromites plotted versus the reciprocal of the square root of the tetrahedral cation mass. Data from the present work on  $NiCr_2O_4$  and  $MgCr_2O_4$  is also included.

well with the  $ZnFe_2O_4$  data. If this lower frequency feature can be assigned to the  $FeO_6$  of the inverse lattice, the higher frequency  $A_{1g}$  feature,  $715 \text{ cm}^{-1}$  for  $MgFe_2O_4$  and  $702 \text{ cm}^{-1}$  for  $NiFe_2O_4$ , should be assigned to the divalent cation occupying the octahedral position.

Raman spectra of the  $CoFe_2O_4$ ,  $MgFe_2O_4$ , and  $NiFe_2O_4$  inverse spinels exhibit shoulders on the  $A_{1g}$  mode [96,97,109]. A common interpretation of these shoulders is that the distinct  $AO_6$  and  $BO_6$  octahedral units within the inverse lattice create the two features. However, as Laguna-Bercero et al. point out, if this were the case, the

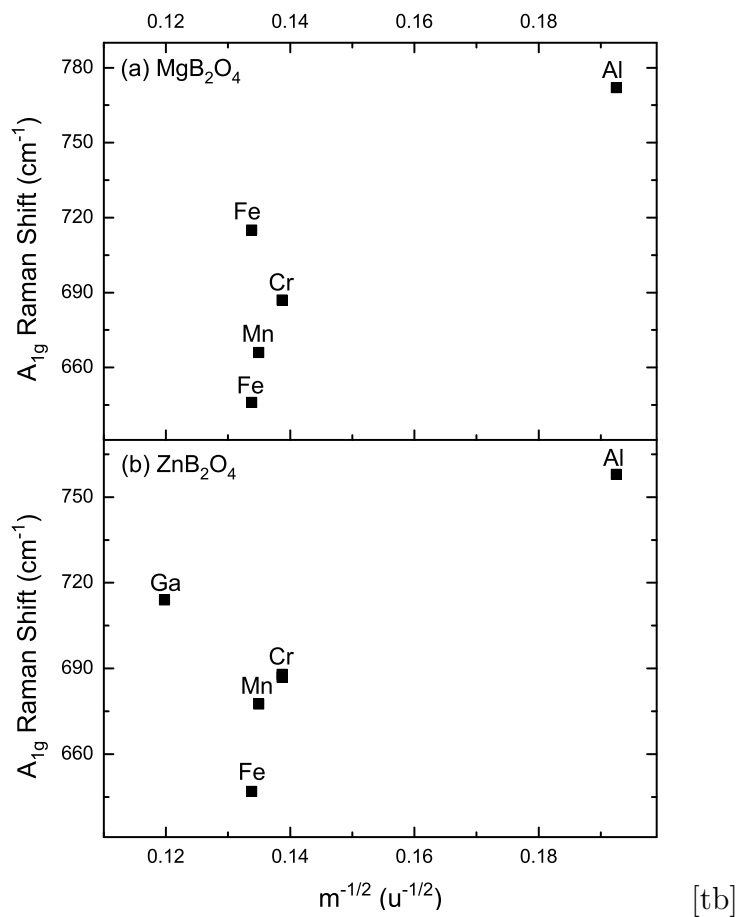


Figure 8. The Raman shifts of the  $A_{1g}$  mode of some (a)  $\text{MgB}_2\text{O}_4$  and (b)  $\text{ZnB}_2\text{O}_4$  spinels show a large, but similar dependence on the octahedral cation. The Raman spectrum of  $\text{MgFe}_2\text{O}_4$  displays two possible  $A_{1g}$  modes.

ratio of intensities of these features should be proportional to the amount of inversion within the spinel [41], and this is not seen in any of the inverse spinels in Table 3.  $\text{Fe}_3\text{O}_4$ , although an inverse spinel, does not contain these dual  $A_{1g}$  features. This may be attributed to fast electron hopping between the  $\text{Fe}^{3+}$  and  $\text{Fe}^{2+}$  cations occupying the octahedral sites [23, 51]. As a result, a valency of +2.5 is often quoted for the octahedral site of  $\text{Fe}_3\text{O}_4$ .

Laguna-Bercero et al. report that the  $A_{1g}$  mode of  $\text{NiAl}_2\text{O}_4$  contains more than two shoulders, and perform a fit using four peaks to the broad  $A_{1g}$  mode [41]. They argue that modeling the mode as solely based on the two distinct octahedra is insufficient. Instead, they argue that the mode is due to the tetrahedra, but the octahedral cations neighboring the tetrahedra must also be accounted for. Because the Al and Ni cations randomly occupy these neighboring sites, there are several different configurations, which create the four components of the broad  $A_{1g}$  mode.

In their study of  $\text{NiAl}_2\text{O}_4$ , Laguna-Bercero et al. report that the compilation of II-III spinel oxides show that the  $E_g$  mode is closely related to the bond distance between the octahedral cation and the oxygen [41]. Laguna-Bercero et al. report that the normal spinels have a slightly larger oxygen coordinate,  $u$ , than the inverse spinels, which leads to a large difference in the  $E_g$  mode of the inverse  $\text{NiAl}_2\text{O}_4$  and normal  $\text{MgAl}_2\text{O}_4$ . Specifically, the longer bond distance of the inverse spinels leads to a smaller frequency of the  $E_g$  mode. Table 3 supports this claim, as the inverse ferrites all have lower, but similar  $E_g$  frequencies. The normal chromites, with the exception of  $\text{CdCr}_2\text{O}_4$ , also have similar  $E_g$  frequencies. The solid solutions studied in this work provide a good opportunity to examine this effect and the results will be presented in Chapter 8. Because structure is determined by x-ray diffraction, the bond distances can be determined directly from measurements of the lattice parameter,  $a$ , and the oxygen parameter  $u$  [42].

The  $F_{2g}(1)$  mode of the inverse ferrites, if only a translation of the tetrahedral unit within the lattice, should not vary greatly. With the exception of  $Fe_3O_4$ , many of the ferrites do have a similar  $F_{2g}(1)$  frequency. Interestingly, even the normal  $ZnFe_2O_4$ , has a similar  $F_{2g}(1)$  mode.

Gasparov et al. reported small shifts in the  $A_{1g}$  and  $F_{2g}(3)$  modes for  $Fe_3O_4$  with small substitutions (1-4% by molar amount) of aluminum, nickel, and manganese [110]. One of their main conclusions was that the frequency of these two modes decreases as the ionic radius of the dopants increase. Work by Malavasi et al. on  $AMn_2O_4$  ( $A = Mn, Mg, Zn$ ) shows a decrease in wavenumber of one of their reported Raman-active modes upon an increase of the ionic radius [108]. Figure 9 plots the wavenumbers of the Raman-active modes from the literature versus the ionic radii (in pm) [111] for different chromites. The  $A_{1g}$ ,  $E_g$ , and  $F_{2g}(2)$  modes decrease in frequency with increasing ionic radius, but the decrease is entirely due to the Cd cation. The  $F_{2g}(3)$  mode shows no dependence on the ionic radius, with or without the Cd data points.

The wavenumber of the spinel vibrational modes depend upon the lattice parameter of the spinel lattice. The lattice parameter of spinel decreases with increasing pressure [112]. Wang et al. has performed many studies of various spinels and reports that all of the detected vibrational modes increase with increasing pressure [47, 48, 95, 97, 98]. As the distance between the positive and negative cations gets smaller, the resulting electrostatic force will increase. The high pressure data on chromites presented by Sawaoka et al. shows that the volume of  $MgCr_2O_4$  decreases by 5% as the pressure is increased to 8 GPa. [112] Wang et al. reports wavenumber increases of 2 to 4  $cm^{-1}$  per GPa for the Raman-active modes of  $MgCr_2O_4$ ,  $NiCr_2O_4$ , and  $ZnCr_2O_4$  [47, 48]. Combining these two changes, using

$$\frac{\Delta\bar{\nu}}{\Delta V} = \frac{\Delta\bar{\nu}}{\Delta P} \frac{\Delta P}{\Delta V}, \quad (4.1)$$

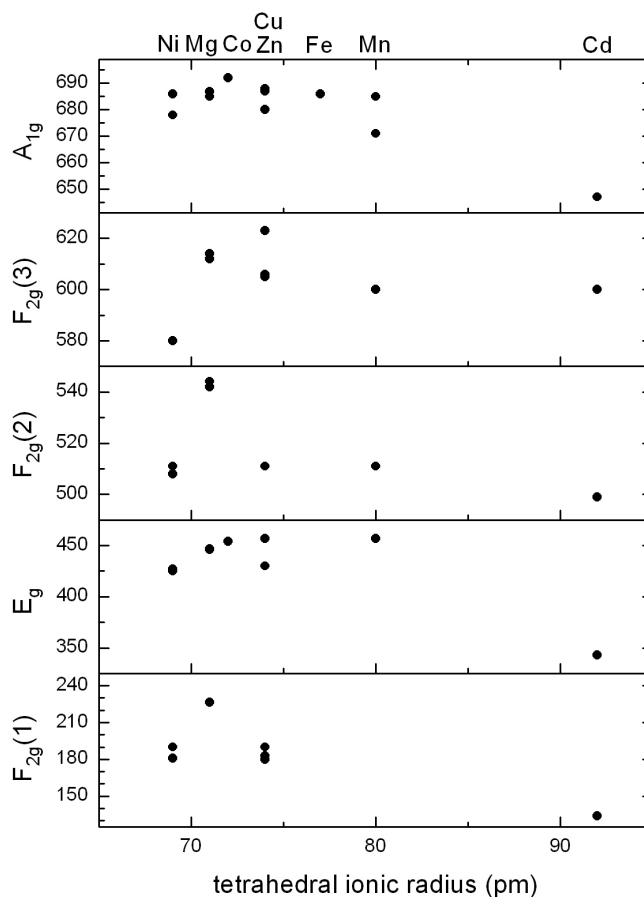


Figure 9. The Raman frequencies of various chromites plotted versus the ionic radius of the tetrahedral cation.

yields an approximate increase in the Raman shift of  $0.32$  to  $0.64 \text{ cm}^{-1}$  per  $0.1\%$  decrease in unit cell volume.

#### Experimental work on solid solution spinels

Although there has been a large amount of experimental work on pure spinels, solid solution spinel systems have not been examined to the same extent using vibrational spectroscopy. The relationship between the vibrational modes and cation substitution is complicated, as the vibrational modes can be dependent upon the mass of the cations, the bonding forces, and the ionic radii. All these variables change with



substitution of one cation with another.

Infrared absorption data exist on some spinel solid solutions. Preudhomme et al. studied zinc spinels, chromites, and rhodites, which are all normal spinels, using infrared spectroscopy [88]. They presented the dependence of the four infrared-active modes upon the methodical exchange of either the divalent or trivalent cation for the  $\text{Mg}_x\text{Co}_{1-x}\text{Cr}_2\text{O}_4$  and  $\text{ZnCr}_x\text{Rh}_{2-x}\text{O}_4$  series.

Basak and Ghose studied infrared spectra of three different substituted  $\text{CuCr}_2\text{O}_4$  spinels [113]. Two of the solid solutions substituted the  $\text{Cu}^{2+}$  cation with  $\text{Mg}^{2+}$  and  $\text{Cd}^{2+}$ . The third substituted  $\text{Cr}^{3+}$  with  $\text{Rh}^{3+}$ . They report a broadening of the  $\nu_1$ ,  $\nu_2$ , and  $\nu_3$  modes for any lattice containing more than one atomic species of cation on either the tetrahedral or the octahedral site.

The two higher frequency infrared-active modes are often broad [88]. Preudhomme et al. instead refer to these two modes as regions of absorption as they notice distinct shoulders or even splitting of these modes. They provided evidence that, for the normal II-III spinels, these modes are dependent upon the trivalent octahedral cation. Preudhomme et al. also examined the infrared-active modes of different II-III spinels to test if the infrared-active modes depend upon the mass of the divalent or trivalent cation [88]. For the compiled infrared data on different chromites,  $\text{ACr}_2\text{O}_4$  with  $\text{A} = \text{Mg}, \text{Zn}, \text{Co}, \text{Ni}, \text{Mn},$  and  $\text{Cd}$ , they concluded that the lower-frequency infrared-active modes have a small dependence on the mass of the divalent cation.

Work by Gupta et al. on mixed chalcogenides has shown good agreement for the infrared-active modes [73]. Sinha also observed agreement with measured higher-frequency infrared-active modes of the  $\text{Cu}_x\text{Mg}_{1-x}\text{Cr}_2\text{O}_4$  series, although a third mode of lower frequency showed less agreement [77]. Himmrich et al. also performed calculations on  $\text{ZnCr}_2\text{O}_4$  which showed good agreement with experimental infrared and Raman spectroscopic results [114].

Raman spectroscopic studies of solid solutions of spinels is less common than infrared absorption data. McCarty et al. studied the spinel system  $\text{Fe}_x\text{Cr}_{3-x}\text{O}_4$  [45] over the range of  $1 \leq x \leq 3$ . Only the  $A_{1g}$  mode was visible in all of their Raman spectra. They observed that the wavenumber of the  $A_{1g}$  mode is inversely proportional to the lattice parameter of the  $\text{Fe}_x\text{Cr}_{3-x}\text{O}_4$  system.

Nakagomi et al. studied the  $\text{Mg}_x\text{Fe}_{3-x}\text{O}_4$  spinel system and reported two  $A_{1g}$  phonons that they suggest to result from coexisting  $\text{MgO}_4$  and  $\text{FeO}_4$  tetrahedrons [106]. They argue that the two-mode behavior results from the large mass difference of the Fe and Mg cations. They also conclude that the increased tetrahedral site, due to substituting  $\text{Fe}^{3+}$  with  $\text{Mg}^{2+}$ , decreases the frequency of the vibrational modes.

Recently, Bahlawane et al. studied the cobalt-iron system  $\text{Co}_{3-x}\text{Fe}_x\text{O}_4$  and reported the most significant effect on the  $A_{1g}$  mode during the initial substitution at the octahedral site of the spinel lattice, before the iron began entering the tetrahedral sites and inverting the lattice [115]. The  $A_{1g}$  mode developed a shoulder on the high-frequency side of the mode, once inversion of the lattice began occurring. The  $E_g$  mode suffered a smaller change, but this change was also observed during the initial substitution, before inversion of the lattice occurred.

Malézieux et al. studied the  $\text{MgCr}_x\text{Al}_{2-x}\text{O}_4$  system by examining both natural and synthetic spinel samples [116]. The  $A_{1g}$  mode of their synthetic samples also shows an inverse relationship between the wavenumber of this mode and the lattice parameter. The lattice parameter increases linearly, while the position of the  $A_{1g}$  mode decreases linearly from  $760 \text{ cm}^{-1}$  at the  $\text{MgAl}_2\text{O}_4$  end of the series to  $685 \text{ cm}^{-1}$  at the  $\text{MgCr}_2\text{O}_4$  end. Malavasi et al. examined the tetragonally distorted  $\text{Mg}_{1-x}\text{Mn}_x\text{Mn}_2\text{O}_4$  spinel system [108]. Their data also support the  $A_{1g}$  mode wavenumbers as inversely proportional to the lattice parameter of the spinel, although the shift in wavenumber of the Raman-active mode is only approximately 1%.

Identification of solid solutions in corrosion layers requires knowledge of the behavior of the vibrational modes over the entire range of composition. For example, Cunha et al. made the assumption that the Raman peaks of solid solutions could be fitted linearly between the two pure end-member spinels [24]. They wanted to identify unknown oxide layers on corroded 316L stainless steel and recognized that a solid solution spinel may be formed in the corrosion layer. They identified the inner oxide layer as a mixture of  $\text{Fe}_3\text{O}_4$ ,  $\text{FeCr}_2\text{O}_4$ , and  $\text{Cr}_2\text{O}_3$  [24]. They reported an outer oxide layer, consisting of  $\text{Ni}_{0.75}\text{Fe}_{2.25}\text{O}_4$  inverse spinel, with  $\text{Fe}_3\text{O}_4$  also forming in the intermediate layer. This identification of  $\text{Ni}_{0.75}\text{Fe}_{2.25}$  will be inaccurate if the frequencies of the Raman-active modes do not shift linearly upon nickel substitution in  $\text{Fe}_3\text{O}_4$ .

Raman spectroscopic data are available in the literature for a number of pure  $\text{AB}_2\text{O}_4$  spinels oxides, but certainly not all. However, Raman data of solid solutions is much more limited and fragmentary. In a solid solution of spinels, the wavenumber shifts in vibrational modes upon composition change are not known experimentally, or understood theoretically. Experimental data will be an invaluable asset for those checking models and calculations of the vibrational modes of spinel.

Trends noticed from the compiled data of the Raman-active vibrations of spinels can be examined from data on solid solutions. In addition, conclusions made by other researchers regarding the behavior of these modes can be tested for general application on all spinels.

## CHAPTER 5

### EXPERIMENTAL SETUP

Three series of solid solution spinel oxides were synthesized, in order to study the effect of cation substitution on the vibrational modes of spinel. A micro-Raman spectrometer was constructed for the purposes of this research and will be discussed in detail below. A Varian FTS FTIR spectrometer, fitted with a photoacoustic detector, was also used for taking complementary infrared-absorption spectra on the  $\text{Mg}_x\text{Ni}_{1-x}\text{Cr}_2\text{O}_4$  series. X-ray diffraction was performed on all samples using a Bruker AXS D8 Advance Vario diffractometer with a Johansson-type primary monochromator.

LBE-corroded stainless steels were obtained from the Institute of Physics and Power Engineering (IPPE) in Obninsk, Russia, on contract from Los Alamos National Lab. The compositions of the three stainless steels are shown in Table 4. 316L stainless steel is a stainless steel containing small amounts of carbon. D9 is a nuclear grade stainless steel containing small amounts of titanium to help reduce void swelling of the steel in a reactor environment [117]. Void swelling results from the neutron flux within a reactor displacing atoms within the stainless steel lattice, creating voids. HT9 stainless steel is a ferritic alloy which is common as cladding and structural components because of its high-temperature strength and radiation tolerance.

Samples of these stainless steels were exposed in a LBE loop at the IPPE at temperatures of 550°C for 1000, 2000, and 3000 hours. The oxygen concentration in the LBE was controlled and maintained at levels of  $10^{-6}\%$  by weight. The steel

Steel	Fe	Cr	Si	Ni	C	Mo	Mn	Ti	W	V
316L	66.12	17.3	0.35	12.1	0.02	2.31	1.8	-	-	-
D9	68.4	13.6	0.85	13.6	0.04	1.11	2.1	0.3	-	-
HT9	84.65	11.95	0.4	0.5	0.2	1.0	0.57	-	0.4	0.33

Table 4. Elemental composition as a weight percent of 316L, D9, and HT9 stainless steels.

samples were rods and hollow tubes of approximately 10 cm in length and 1 cm in diameter. Cross sections were cut from the steels and mounted in epoxy so that the corrosion layers could be better examined. Sample polishing was performed on the samples using increasingly smaller grit. The final polish was performed with a 5  $\mu\text{m}$  diamond dust. Sample preparation was previously performed by Koury [60].

### Spinel synthesis

Synthesis of the pure and solid solution spinels studied here closely follows a simple combustion method described by other researchers [118, 119]. In a 100 ml beaker, stoichiometric amounts of metal nitrates, purchased from Alfa Aesar and of 98% or greater purity, was mixed with urea and a small amount of water, just enough to dissolve the ingredients. The solution was then placed in a furnace set to a temperature of approximately 375°C for 15 to 20 minutes. In order to protect the inside of the furnace from contamination caused by the explosive combustion reaction, the 100 ml beaker was placed on top of another wide dish containing a small amount of quartz wool at the base. Another beaker was then placed upside down over the top of the 100 ml beaker. This setup allowed gases to escape from the reaction through the quartz wool, but also filtered any spinel from being expelled during the combustion. This multiple beaker setup can be seen in Figure 10.

The recipe for  $\text{NiCr}_2\text{O}_4$  will serve as an example of the calculations necessary for the synthesis of the spinels. A redox reaction of nickel(II) nitrate,  $\text{Ni}(\text{NO}_3)_2 \cdot 6\text{H}_2\text{O}$ ,

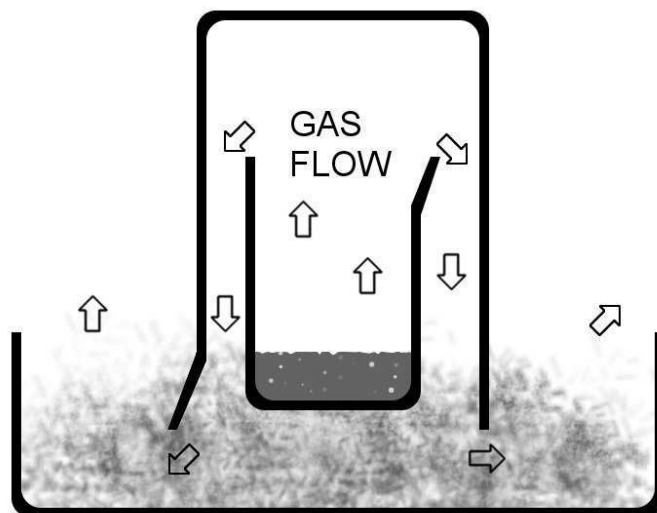
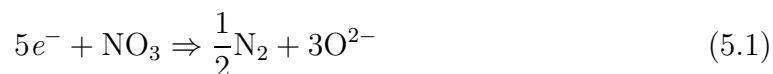
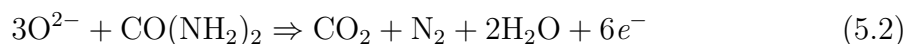


Figure 10. The combustion synthesis was contained within a series of beakers and quartz wool. This setup was then placed and heated inside a furnace.

chromium(III) nitrate,  $\text{Cr}(\text{NO}_3)_3 \cdot 9\text{H}_2\text{O}$ , and urea,  $\text{CO}(\text{NH}_2)_2$  yields  $\text{NiCr}_2\text{O}_4$ ,  $\text{CO}_2$ ,  $\text{N}_2$ , oxygen, and water. The  $\text{Ni}^{2+}$  and  $\text{Cr}^{3+}$  remain at the same oxidation state, but the nitrogens in the nitrates change from +5 to 0, while the nitrogens in the urea change from  $-3$  to 0. The carbon and hydrogen remain at +4 and +1, respectively. Thus, every nitrogen from the nitrate requires five electrons to change from +5 to 0.



Every nitrogen from the urea gives up 3 electrons to change oxidation state from  $-3$  to 0, for a total of 6 electrons from every urea molecule.



One  $\text{Ni}^{2+}$  and two  $\text{Cr}^{3+}$  ions are required for the spinel, indicating a total of 8 nitrogens from the metal nitrates. These 8 nitrogens require a total of 40 electrons to change to an oxidation state of 0, which are given up by  $40/6 = 6.67$  molecules of urea. The

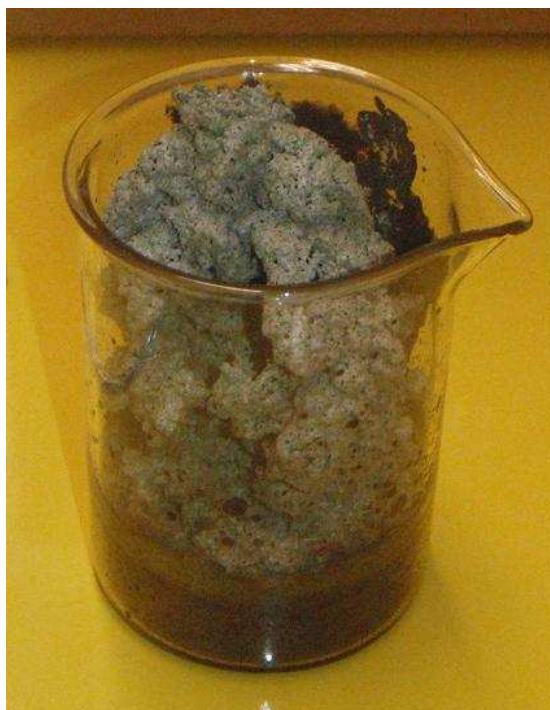


Figure 11. The foamy product of  $\text{NiCr}_2\text{O}_4$  spinel immediately after synthesis.

resulting mole ratio of nickel nitrate : chromium nitrate : urea is 1:2:6.67.

The actual weights of the compounds must be calculated using the molecular weights of the reagents, including the waters of hydration, as appropriate. The waters of hydration pass through the reaction without change. For  $\text{NiCr}_2\text{O}_4$ , 0.73 g of  $\text{Ni}(\text{NO}_3)_2 \cdot 6\text{H}_2\text{O}$ , 2.00 g of  $\text{Cr}(\text{NO}_3)_3 \cdot 9\text{H}_2\text{O}$ , and 1.00 g of urea are required to balance the stoichiometry. The reactions of any of the other spinels and solid solution spinels are essentially the same, since the number of nitrates do not change when different cations of the same charge are selected. Reagents for synthesis of all spinels were measured within 0.2% of the desired weight.

The combustion reaction produces a light, fragile foam that is easily crumbled into a powder. The foam product is shown in Figure 11. The chromium end spinels

produce a very light foam, whereas the iron end spinels are much more dense.

$\text{Mg}_x\text{Ni}_{1-x}\text{Cr}_2\text{O}_4$  was synthesized using the above described method without need for any additional treatment to the samples. 22 samples of this series were synthesized, varying the magnesium content in increments of  $\Delta x = 0.1$ , and each composition being synthesized twice. The  $\text{NiFe}_x\text{Cr}_{2-x}\text{O}_4$  and  $\text{Fe}_x\text{Cr}_{3-x}\text{O}_4$  series required additional preparation to achieve the spinel phase for all samples within these two series.

On the high iron end of the  $\text{NiFe}_x\text{Cr}_{2-x}\text{O}_4$  series, the combustion synthesis did not result in a high-crystalline spinel phase. XRD patterns of the as-synthesized samples contained broad and weak diffraction peaks. Ramalho et al. synthesized  $\text{NiFe}_2\text{O}_4$  and calcined the powder at  $700^\circ\text{C}$  for two hours after the combustion reaction [120]. The samples in this series were all heated to  $700^\circ\text{C}$  for 12 hours in air immediately following the combustion synthesis. After this calcination, XRD patterns showed more intense and sharp diffraction patterns, characteristic of the spinel phase. A total of 22 different  $\text{NiFe}_x\text{Cr}_{2-x}\text{O}_4$  samples over the entire range of  $0 < x < 2$  were synthesized and calcined. The iron content was varied by 0.1 between each sample, with an additional sample having  $x = 0.05$ , to investigate only a small substitution of iron into the  $\text{NiCr}_2\text{O}_4$  lattice.

The  $\text{Fe}_x\text{Cr}_{3-x}\text{O}_4$  system also required additional preparation after the combustion process. Similar to the  $\text{NiFe}_x\text{Cr}_{2-x}\text{O}_4$  series, acquired XRD spectra of these samples possessed only weak spinel phase diffraction peaks. As an example, Figure 12 displays the XRD spectrum of an  $\text{Fe}_x\text{Cr}_{3-x}\text{O}_4$  sample with  $x = 2.2$  immediately after the combustion reaction. Some samples also had crystallized with significant impurities of a corundum phase instead of being entirely spinel. The XRD spectrum of a sample of this series with  $x = 0.6$  is shown in Figure 13. The peaks are characteristic of the corundum phase. This was not too surprising as  $\text{Fe}_3\text{O}_4$  is known to oxidize to the  $\alpha\text{-Fe}_2\text{O}_3$  at high temperature [1, 121].



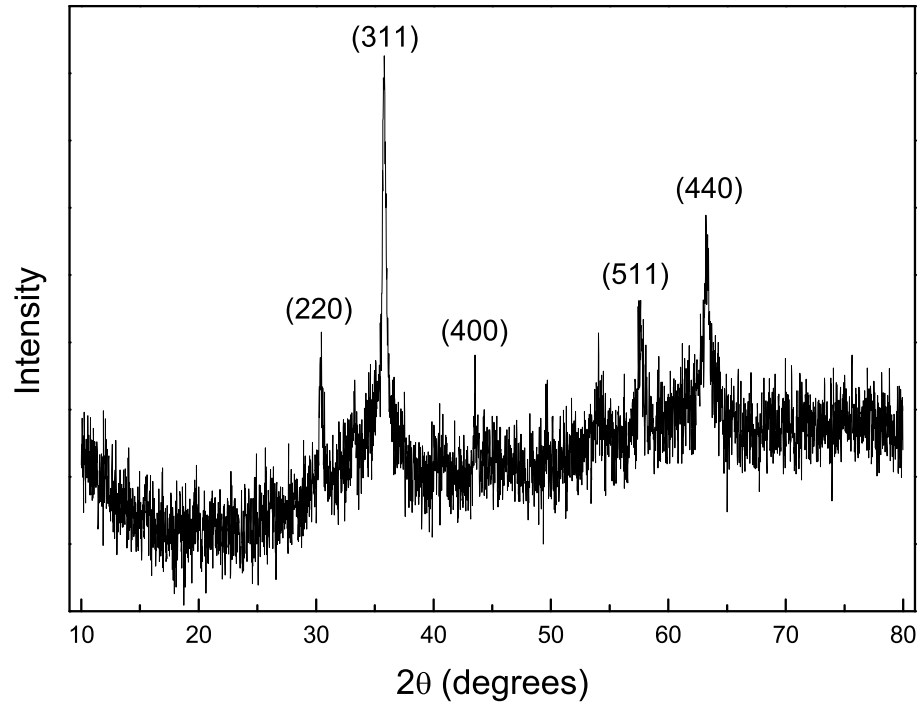


Figure 12. X-ray diffraction pattern of the as-combusted  $\text{Fe}_{2.2}\text{Cr}_{0.8}\text{O}_4$ . The diffraction spectra of many as-combusted  $\text{Fe}_x\text{Cr}_{3-x}\text{O}_4$  samples were similar and exhibit very weak spectra.

A reduction environment was assembled to reduce the secondary phase within the as-combusted  $\text{Fe}_x\text{Cr}_{3-x}\text{O}_4$  powders from the corundum phase to the spinel phase. In a reducing environment, the following reaction occurs, which converts corundum phase hematite into spinel phase magnetite:



This reaction can be performed using hydrogen gas, which removes oxygen from the corundum phase to produce water and the iron-chromium spinel.

A sketch of the apparatus making up the reducing furnace can be seen in Figure 14. A stainless steel guard tube, open at one end, was placed inside a Thermodyne 79300 vertical tube furnace. Inside this guard tube, a 2" diameter quartz tube was inserted,

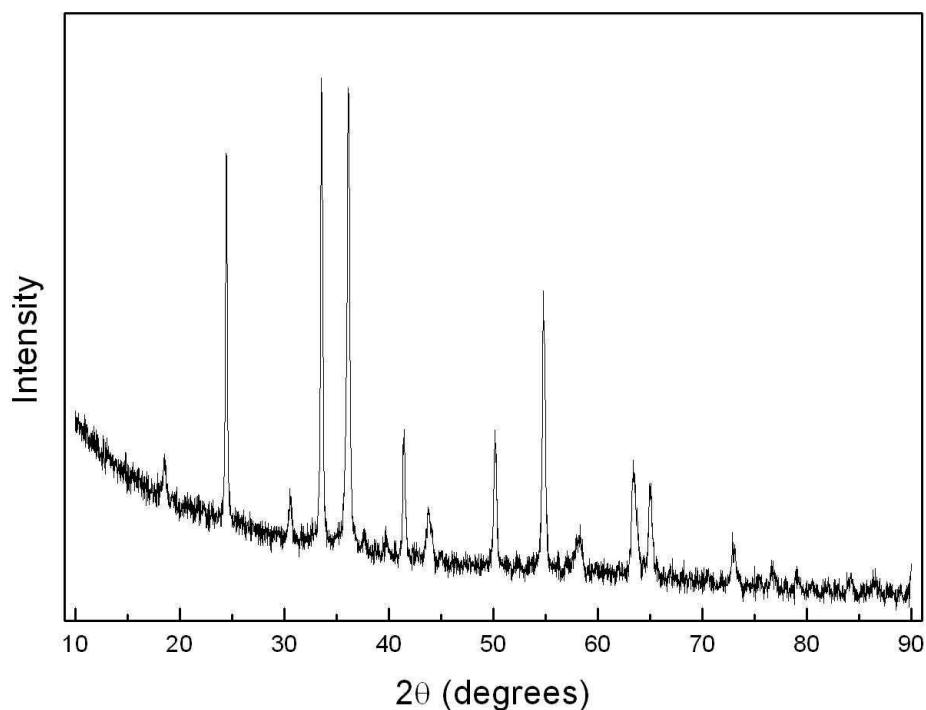


Figure 13. The XRD patterns of some  $\text{Fe}_x\text{Cr}_{3-x}\text{O}_4$  samples were characteristic of the corundum phase, instead of the spinel phase, immediately after combustion.

also open at the top. The open end of the large quartz tube was covered with an attachment having two ports, to allow a reducing gas to flow in and out of the guard tube. For holding a small amount of the powder sample, a 0.25 in. quartz tube was sealed at one end, and a window was cut 1" from the end, where the powder could be stored. This quartz tube was slid into one of the ports on the top of the 2" quartz tube. The reducing gas was a mixture containing 2%  $\text{H}_2$  and 98% argon. The gas flow was controlled at 20.0 sccm with a MKS Mass-Flo gas flow controller. The gas inlet was connected directly to the 0.25 in. quartz tube containing the sample. The window allowed gas to escape the quartz tube and eventually exit the system through the second port on the top piece. The temperature of the furnace was set to 700°C. The sample was allowed to reduce overnight and cooled to room temperature over a

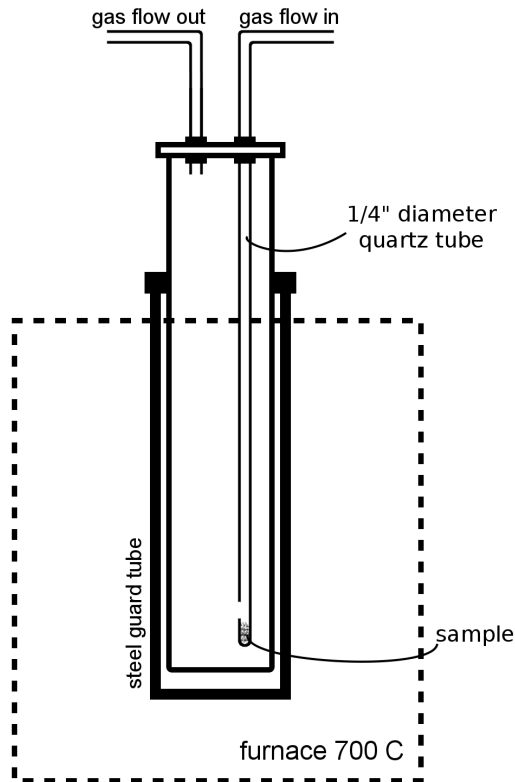


Figure 14. Schematics of the reducing furnace. The  $\text{Fe}_x\text{Cr}_{3-x}\text{O}_4$  series required heating to  $700^\circ\text{C}$  in a reducing environment of a hydrogen and argon gas mixture. The sample was placed at the bottom of the quartz tube.

period of eight hours under gas flow.

The literature examines the iron content range of  $1 \leq x \leq 3$  for  $\text{Fe}_x\text{Cr}_{3-x}\text{O}_4$  [122–124]. This begins with  $\text{FeCr}_2\text{O}_4$ , where  $\text{Fe}^{2+}$  occupies the tetrahedral position. From  $1 \leq x \leq 3$ ,  $\text{Fe}^{3+}$  is substituted for  $\text{Cr}^{3+}$ . Samples over the range of  $0.8 \leq x \leq 3$ , and in increments of 0.2, were synthesized and studied in this work.

### X-ray diffraction

The Bruker D8 Advance diffractometer uses a copper source with  $\text{K}\alpha_1$  wavelength of  $1.54063 \text{ \AA}$ . Scans were done over a  $2\theta$  range of 10 to 120 degrees with a step size

of 0.008 degrees. Acquisition time was four hours. Topas 4.2 software was used to fit the x-ray diffraction patterns using the Pearson VII peak function, an approximation of the Voigt function.

X-ray diffraction was performed on all synthesized samples to prove that the synthesis process actually produced the desired spinel phase. X-ray diffraction patterns were calibrated using a high-crystalline silicon standard. The silicon powder was mixed with the spinel powder in an approximate 1:5 weight ratio of silicon to spinel. The mixture was then mixed and ground in an agate mortar before being placed onto the sample stage. A few drops of alcohol were then added onto the powder to create a slurry that could be evenly spread across the surface of the sample stage. The alcohol does not react with any of the spinel samples. The Topas software was used for the analysis of the diffraction data and for determining the lattice parameters of the spinels. The silicon standard is exclusively fitted first to provide the calibration for the x-ray diffraction pattern. The x-ray diffraction pattern of silicon is well known [125]. The NIST-quoted positions of these lines using the  $K\alpha_1$  radiation of copper are shown in Table 5.

The diffraction spectrum of spinel is very different than the spectrum of another common phase of metal oxides, the corundum phase, shown in Figure 13. A diffraction spectrum acquired with the Bruker diffractometer of  $\text{Fe}_{1.4}\text{Cr}_{1.6}\text{O}_4$ , containing the silicon standard used for calibration, is shown in Figure 15.

Typically, the XRD pattern of most of the samples showed that a very small amount of the crystalline sample, usually less than 3%, of the powder, existed as the corundum phase. The most likely product would be either  $\text{Cr}_2\text{O}_3$  for the chromite samples and  $\alpha\text{-Fe}_2\text{O}_3$  for the ferrite samples, or a solid solution of  $\alpha\text{-Fe}_2\text{O}_3$  and  $\text{Cr}_2\text{O}_3$ .

hkl	Angle ( $2\theta$ )
111	28.439
220	47.297
311	56.115
400	69.120
331	76.365
422	88.017
511	94.937
440	106.690
531	114.071
620	127.516
533	136.858

Table 5. The XRD spectral lines of the silicon standard used for calibration.

#### Determination of lattice parameters

Spinel is a cubic lattice, and thus only a single lattice parameter is required to define the dimensions of the unit cell. As described above, knowing the angle of the diffraction peaks for all of the Miller planes determines the lattice parameter  $a$ . Because each peak gives a value for the lattice parameter, an average can be calculated using all of the diffraction peaks from a diffraction spectrum. The Topas software uses the Rietveld refinement method to determine the lattice parameter of the crystal structure [55]. The oxygen parameter  $u$  was also refined during the process. The x-ray diffraction spectrum of  $\text{MgCr}_2\text{O}_4$  with a silicon standard, the Rietveld fit and residual is shown in Figure 16.

Table 6 shows good agreement of the lattice parameters of the pure  $\text{AB}_2\text{O}_4$  spinels synthesized in this work with values reported from literature. The weighted profile R-factors for refinements from all samples were usually between 1.0 and 3.0. The full results of the Rietveld refinements can be seen in Appendix A

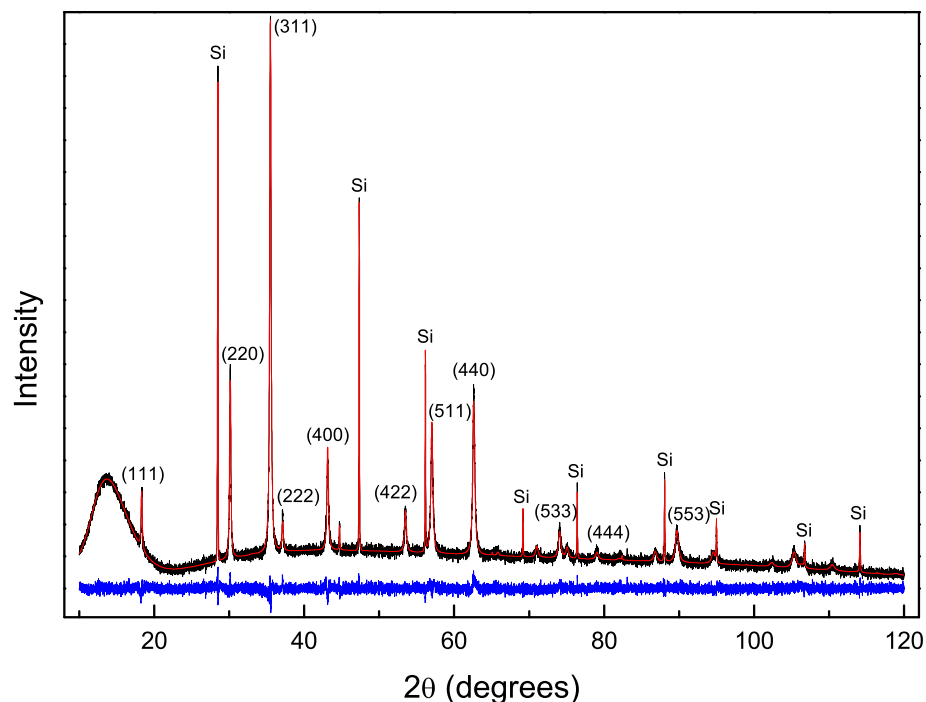


Figure 15. X-ray diffraction pattern of  $\text{Fe}_{1.4}\text{Cr}_{1.6}\text{O}_4$  spinel powder mixed with a high-crystalline silicon standard. The x-ray diffraction data is in black. The Rietveld fit and residual is in red and blue, respectively. Full Rietveld refinement results is located in Appendix A.

### Infrared photoacoustic spectroscopy

Fourier transform infrared spectroscopy (FTIR) is a common technique used for measuring the infrared-active vibrational modes of a sample. Light from a broad spectrum infrared source is collimated and sent into an interferometer. The interferometer contains a beamsplitter that divides the light into two separate paths where one light path is reflected from a movable mirror. The other beam is reflected from a fixed mirror. A path length difference between the two beams creates an interference pattern when the beams recombine, which contains the intensity information of all wavelengths from the infrared source. A computer can then calculate the Fourier

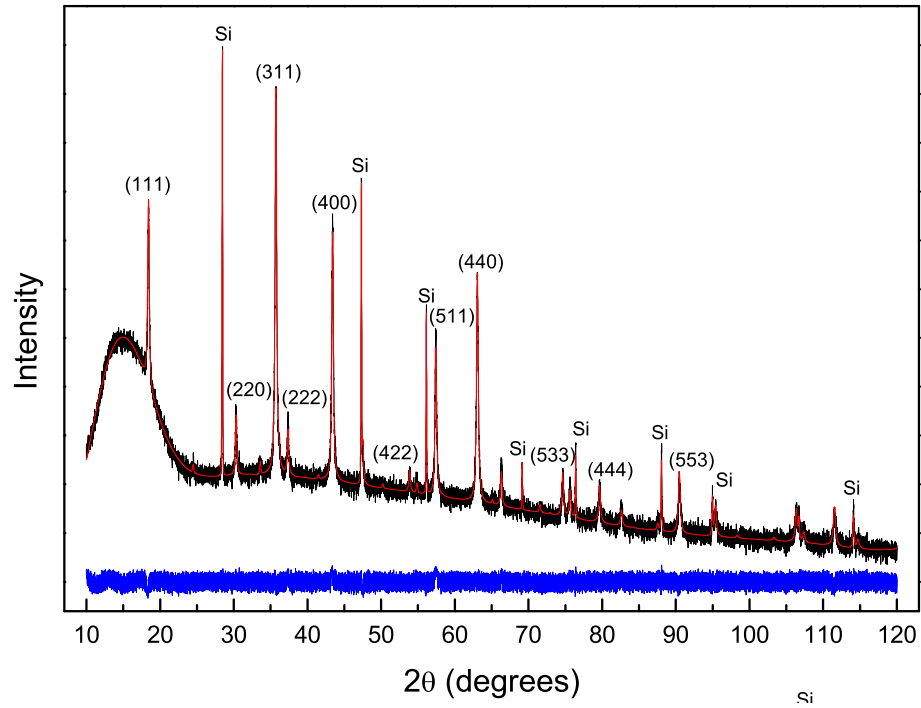


Figure 16. X-ray diffraction pattern of  $\text{MgCr}_2\text{O}_4$ . The fit from the Rietveld refinement is shown in red and the residual is shown in blue. The  $R_{\text{wp}}$  for the fit is 2.90. Full Rietveld refinement results are located in Appendix A.

Spinel	This work	literature
$\text{MgCr}_2\text{O}_4$	8.3344(2)	8.3329(1) [52], 8.3341 [126]
$\text{NiCr}_2\text{O}_4$	8.3185(3)	8.3186 [127]
$\text{NiFe}_2\text{O}_4$	8.3389(2)	8.3391 [127]
$\text{FeCr}_2\text{O}_4$	8.3771(2)	8.3765(2) [52]
$\text{Fe}_3\text{O}_4$	8.3908(4)	8.398(1) [45]

Table 6. Lattice parameters of synthesized spinels. Full Rietveld refinement results are located in Appendix A.

transform of the detected signal to determine the intensities of all of the frequencies contained within the infrared light.

Photoacoustic spectroscopy is a method for measuring the infrared absorption of a sample by detecting induced heating within the sample. The induced heating creates thermal waves that transfer to a gas that fills the sample chamber. A microphone detects the acoustic waves from the gas.

Infrared data on the  $\text{Mg}_x\text{Ni}_{1-x}\text{Cr}_2\text{O}_4$  series were acquired with a Varian FTS FTIR spectrometer equipped with a photoacoustic detector. The low frequency limit of the equipment is  $375\text{ cm}^{-1}$ , above the lowest-frequency IR-active mode. Therefore, only three of the four infrared-active modes are reported for the  $\text{Mg}_x\text{Ni}_{1-x}\text{Cr}_2\text{O}_4$  series.

### Raman microscope

Raman microscope systems have the advantage of obtaining good spatial resolution by focusing to a spot size on the order of only a few micrometers using a focusing objective lens. However, lasers are intense sources of light, and this small spot size creates a very high power density on the sample, which can lead to significant sample heating. Heating of the sample results in broadening of the Raman-active modes, as well as shifts to lower frequencies, due to the vibrational modes of a heated sample requiring less energy to excite. This heating may also lead to oxidization of the sample.

The Raman microscope system was constructed specifically for use in the present work, and thus will be explained in detail. A simple diagram of the major components of the micro-Raman system is shown in Figure 17, and a picture of the laboratory setup is shown in Figure 18.

The excitation source is a Lexel RamanIon krypton ion laser tuned to 647.1 nm. The power output was most commonly set to a very low power of about 5 mW,



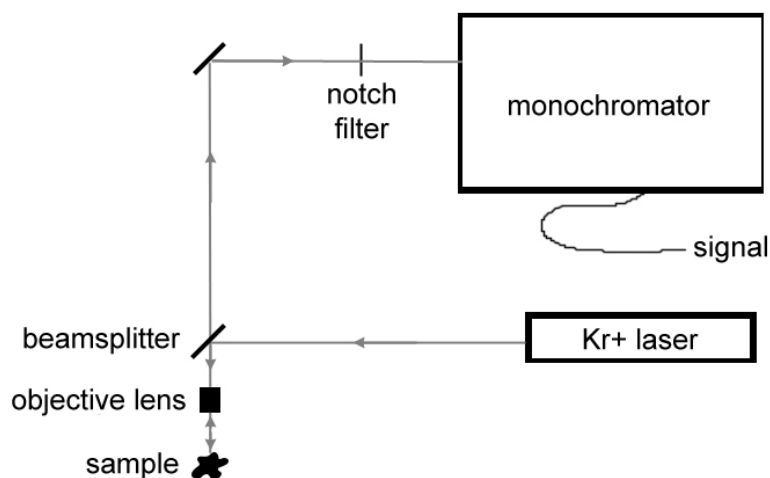


Figure 17. Schematic of the micro-Raman spectrometer.

though the power was further reduced by neutral density filters, to prevent heating effects, as described above, that could lead to shifted Raman peaks or damaged samples. There is also access to a Spectra-Physics BeamLok argon ion laser tuned to 514.5 nm. This gives the option for an alternative excitation source if fluorescence or other problems arise with the krypton laser. For example, the fluorescence from the green-colored  $\text{Cr}_2\text{O}_3$  powder due to excitation from the krypton ion laser overwhelmed the Raman spectrum. However, the excitation with the argon laser does not result in the fluorescence, and the Raman spectrum is easily detected from the background.

The laser light passes through a spatial filter containing a  $10\ \mu\text{m}$  pinhole, before being sent to the entrance port of a Nikon MM-40 Measuring Microscope. A beamsplitter with an anti-reflective coating on one side, to prevent interference from reflections at both the top and bottom surfaces, directs the light down through the microscope objective to be focused onto the sample. The objective also collects the scattered light from the sample, where the light travels back up through the beam-

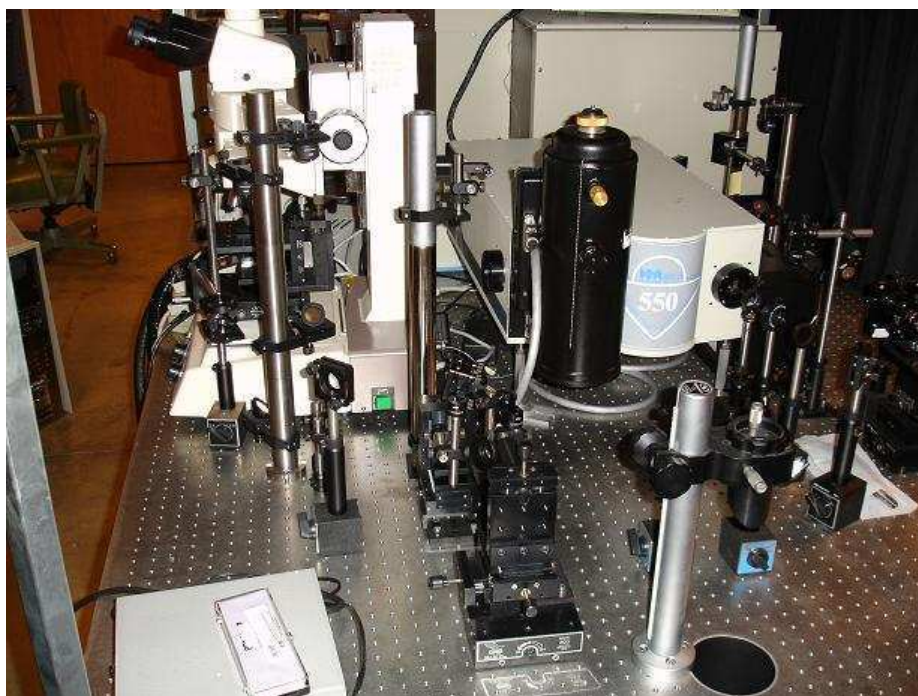


Figure 18. Photograph of the micro-Raman spectrometer. The krypton ion laser is located underneath the optical table. The beam is directed up through the hole seen at the bottom right corner of the image.

splitter to the exit port of the microscope.

A 50X objective was used for most data collection. In the event of sample heating, detected in the  $\text{Fe}_x\text{Cr}_{3-x}\text{O}_4$  series by the appearance of Raman-active modes characteristic of the corundum phase, a 10X or 20X objective or neutral density filters were used to further cut down the power density. If used, the neutral density filters were placed between the spatial filter and the entrance port of the microscope. Alternatively, the sample could be left out of the field of focus to reduce the laser intensity. These methods reduce the intensity of the Raman signal and require longer acquisitions to compensate for the weak signal. Acquisition times of fifteen minutes were required for many samples.

An experiment was performed to determine the focused spot size of the laser

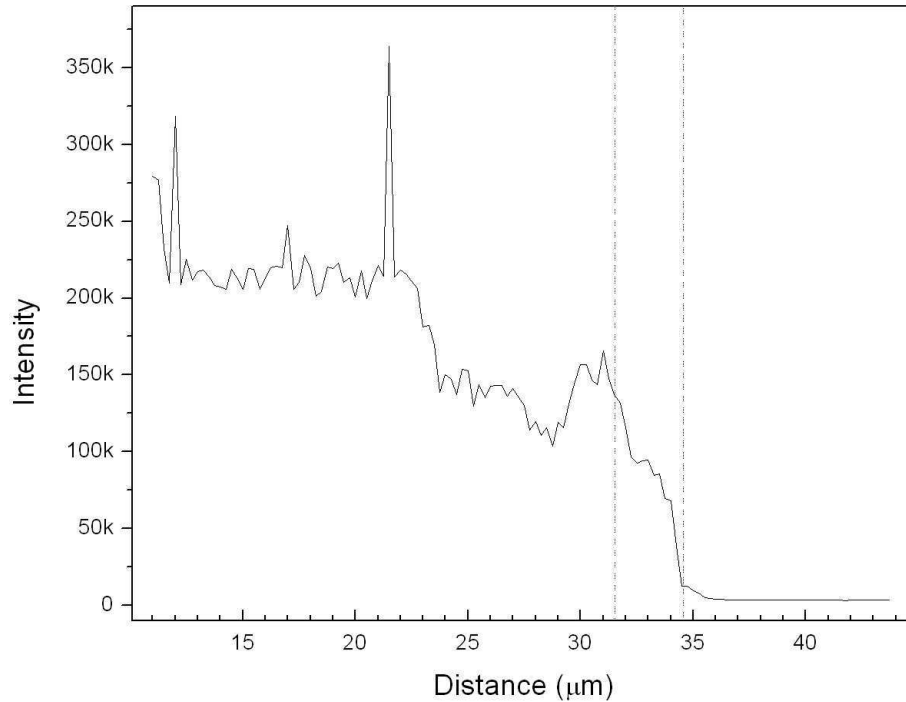


Figure 19. The spot size of the focused laser was determined by a simple razorblade experiment.

on the sample. The laser was focused through the 50X microscope objective onto a razorblade. The intensity of laser reflection was recorded as the razorblade was moved out of the beam path in  $0.25 \mu\text{m}$  increments. The micrometer drive was only accurate down to  $0.5 \mu\text{m}$  increments, so a simple lever arm was constructed to reduce the effective movement by a factor of two. This procedure was performed five times, giving a spot size of  $3.3 \pm 0.2 \mu\text{m}$ . Results from one of the trials can be seen in Figure 19.

The lowest power setting available to the krypton laser is approximately 5 mW. However, after passing through the spatial filter and beamsplitter within the microscope, only about 1 mW is incident upon the sample. Even with this low power, the focused laser spot leads to an intensity of approximately  $25 \text{ W}/\text{mm}^2$ , high enough to cause noticeable heating effects or thermal broadening on many samples. Two

neutral density filters could be placed in the beam path to further cut down the power to approximately 0.5 mW or 0.1 mW, if necessary. Most spectra were acquired with 0.5 mW of laser intensity at the sample. The  $\text{Fe}_x\text{Cr}_{3-x}\text{O}_4$  series was especially sensitive to laser power, and the power was kept to 0.1 mW to prevent sample heating.

The microscope objective collects and collimates the scattered light. This light passes through the beamsplitter within the microscope and exits the upper port of the microscope, where it is directed to the monochromator. A double convex lens of focal length 45 mm focuses the light onto the entrance slit of a Horiba Jobin-Yvon Triax 550 monochromator. The monochromator contains a grating of 600 lines/mm and is blazed at a wavelength of 500 nm. The collimated light from the 50X objective has an approximate diameter of 2 mm at the 45 mm focal length lens. This setup adequately matches the 6.4 f-number of the monochromator to fill the mirrors within the monochromator. The f-number  $f/\#$  of an optical system is given by

$$f/\# = \frac{f}{A}, \quad (5.4)$$

where  $f$  is the focal length of the lens and  $A$  is the aperture diameter of the light.

A Princeton Instruments liquid nitrogen cooled Spec 10 CCD detector was used for photon counting. The temperature of the CCD was maintained at  $-120^\circ\text{C}$  during data acquisition. The CCD has a width of 1340 pixels that must be manually calibrated for wavelength position.

A Kaiser Optical Systems, Inc. holographic notch filter was placed in the light path between the exit port of the microscope and the focusing lens into the monochromator to eliminate the intense Rayleigh scattered light, which would quickly saturate the detector, and hide any Raman-scattered light at small wavenumbers. The notch filter allows the monochromator to detect Raman-scattered photons as low as  $100\text{ cm}^{-1}$ .

The microscope stage accommodates for a wide range of sample sizes. A large 1" thick sample is as easily accommodated as a microscope slide. The stage has

micrometer drives for three-axis motion. The standard oxide powders and synthesized spinel powders were placed on a microscope slide and put under the objective of the Raman microscope. The microscope has a viewport for visual inspection of focusing the laser upon the sample. This allows different spots on a sample to be inspected, such as the cross-section samples of the LBE-corroded stainless steels, where the different corrosion layers may give different Raman spectra.

#### Software and calibration

The WinSpec software used for data acquisition from the CCD can communicate with the detector, but cannot communicate with the monochromator. Separate software controls the grating within the monochromator, and allows a selected wavelength to be centered on the detector. However, the software does not know this position or the dispersion of the grating. Therefore, any time the grating position is adjusted, the spectral range falling on the detector must be calibrated. Calibration is achieved using a UVP brand neon pen-lamp. Neon has many emission lines in the 650-700 nm range [128], where Raman shifts from the 647.1 nm excitation source are located. This range of wavelengths corresponds to Raman shifts of approximately 50 to 1500  $\text{cm}^{-1}$ . The neon spectral lines are fitted with a Gaussian profile. A new calibration is acquired every day, even if the grating was not moved from the previous day.

To check the accuracy of the calibration, the emission lines of argon visible at a grating position of 705 nm, were examined. The neon calibration spectrum, shown in Figure 20, was analyzed and used as a calibration for the argon spectrum, shown in Figure 21. As can be seen in Table 8, the agreement between these lines and literature is very good.

To check the precision of the calibration method, several neon spectra were ac-

Neon lines (nm)
653.29
659.90
667.82
671.70
692.95
702.41
703.24
705.91
717.39

Table 7. Neon emission lines used for calibration of spectrometer at grating positions of 670 nm and 700 nm [128].

quired and fitted. During the course of a single day, five new neon calibration spectra were acquired without moving the grating within the monochromator. At the grating position of 670 nm, four neon lines are detected within the 1340 pixel width of the detector. The standard deviation of the positions of these lines is 0.6 pixels. These neon calibration spectra were then applied to a previously acquired  $\alpha$ -Fe<sub>2</sub>O<sub>3</sub> spectrum to check the variability in the Raman peak centers after WinSpec had performed a linear fit using data from each individual neon calibration. The standard deviation in the  $\alpha$ -Fe<sub>2</sub>O<sub>3</sub> Raman-active modes using the five different neon calibrations is 0.3 cm<sup>-1</sup>. This is the same deviation arrived at for the uncalibrated system, because at this grating position, each pixel represents approximately 0.5 cm<sup>-1</sup>.

### Peak fitting

SeaSolve PeakFit software was used for fitting of all spectral peaks, to determine wavenumbers and intensities of spectral lines. The background is fitted with a third order polynomial and subtracted from the spectrum. The spectra are also cleaned of random noise spikes with the software. As phonons behave identically throughout

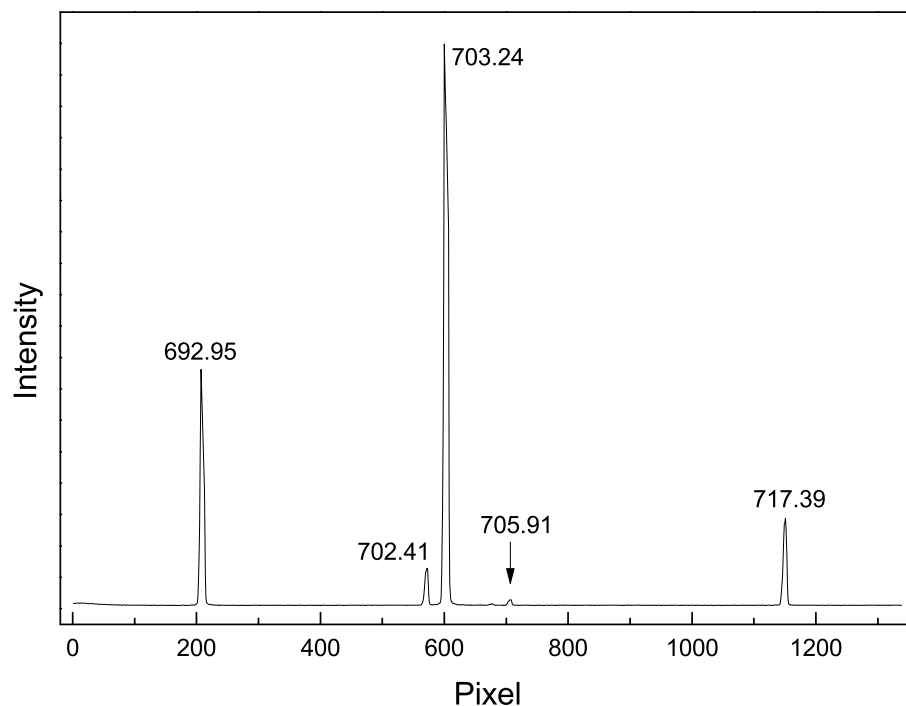


Figure 20. Uncalibrated neon emission spectrum at a grating position of 705 nm. The  $x$ -axis represents the 1340 pixel width of the CCD detector.

the crystal system, Raman peaks are fitted using Lorentzian profiles. Emission lines from the neon pen lamps were fitted with Gaussian line profiles, due to the thermal broadening of the heated neon gas within the lamp.

As an example of an extreme background subtraction, a raw spectrum of  $\text{Cr}_2\text{O}_3$  using the krypton laser is shown in Figure 22. This spectrum has a large sloping background due to sample fluorescence from the 647.1 nm excitation line. The fluorescence is caused from the laser energy exciting an electronic level of  $\text{Cr}_2\text{O}_3$  and emitting photons of longer wavelengths as the electrons relax to the ground state. The same spectrum, with a third order polynomial fitted to the background and subtracted, is shown in Figure 22. A random noise spike, that is also seen at low wavenumbers in the original spectrum, has also been removed with the program.

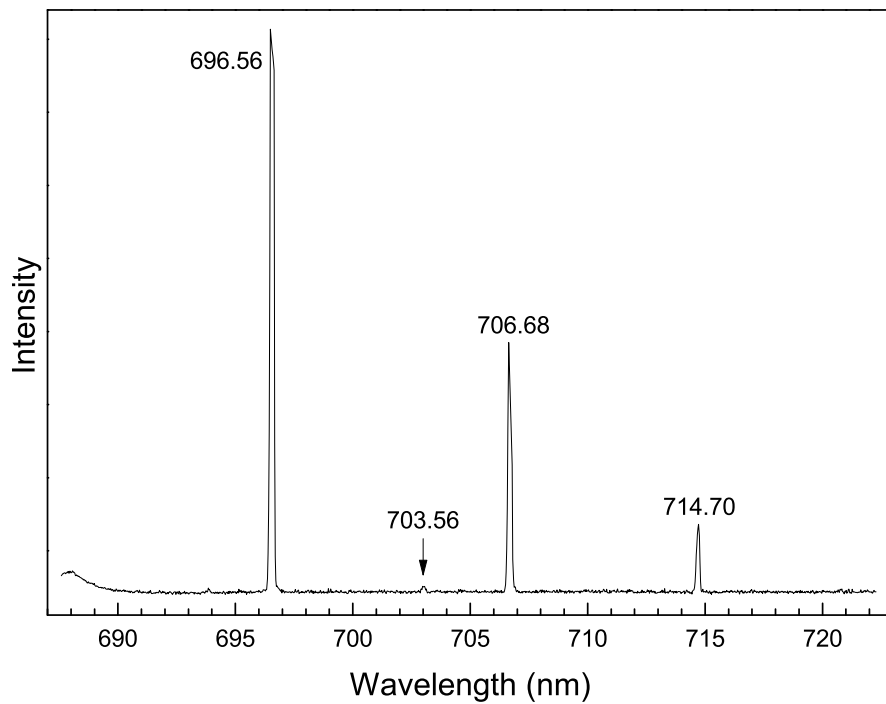


Figure 21. Argon spectrum at a grating position of 705 nm. The  $x$ -axis has been calibrated to the neon lines visible in this spectral range.

This work	NIST [128]
696.56(2)	696.54
703.02(8)	703.03
706.68(2)	706.72
714.70(2)	714.70

Table 8. Argon emission lines, in nm, measured in this work compared, to NIST spectral tables.



## Error analysis

Raman data was acquired at several spots on all samples studied. Raman spectra were fit using the PeakFit software which calculates the standard error of the peak centers used in the fit. A weighted mean was calculated for the Raman shift of all modes of the synthesized solid solutions using the peak centers and uncertainties determined by PeakFit for all acquired spectra. The weighted mean is given by

$$\bar{x} = \frac{\Sigma(x_i/\sigma_i^2)}{\Sigma(1/\sigma_i^2)}, \quad (5.5)$$

where  $x_i$  is the wavenumber of the mode from each fitted peak, and  $\sigma_i$  is the uncertainty in the position of each peak. The uncertainty of the peak center is calculated using the standard deviation of the average added in quadrature with the uncertainty of the weighted mean. This was done because the peak centers of any given composition were occasionally outside of the uncertainties reported by PeakFit.

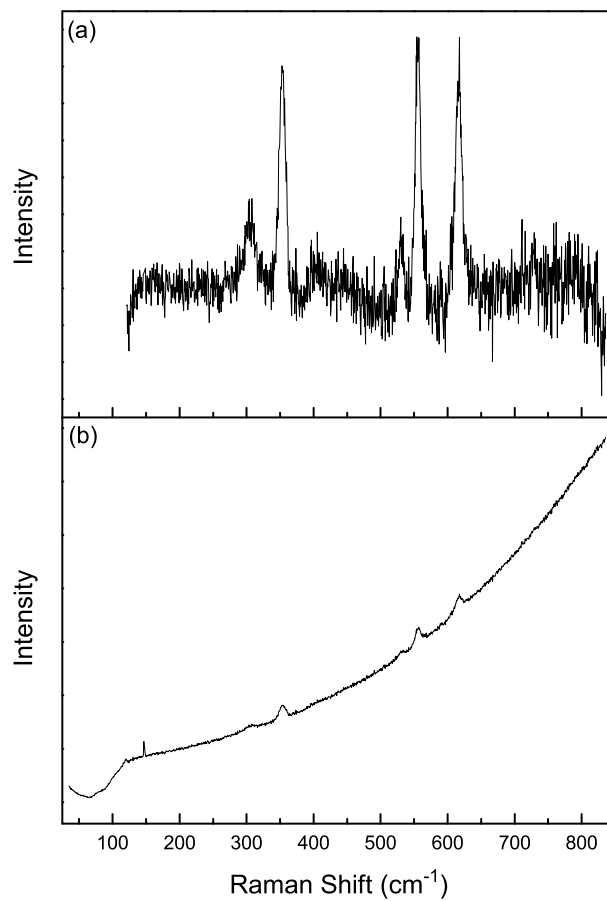


Figure 22. (a) Using PeakFit, a third order polynomial has been fitted to the background and subtracted from the Raman spectrum of Cr<sub>2</sub>O<sub>3</sub> acquired using the krypton laser as the excitation source. (b) The raw spectrum of Cr<sub>2</sub>O<sub>3</sub> showing the fluorescence background resulting from the krypton laser.

## CHAPTER 6

### OXIDE STANDARDS

Standards are used to confirm that the micro-Raman system is working properly as the vibrational spectra of common standards are well characterized, and acquired data can be compared to literature. Several powder oxide standards were purchased and studied with the Raman system developed in the present work. The  $\alpha$ -Fe<sub>2</sub>O<sub>3</sub>, Fe<sub>3</sub>O<sub>4</sub>, and Cr<sub>2</sub>O<sub>3</sub> powder standards are brand Alfa Aesar and are greater than 99.9% pure.

#### Hematite, $\alpha$ -Fe<sub>2</sub>O<sub>3</sub>

Hematite,  $\alpha$ -Fe<sub>2</sub>O<sub>3</sub>, is the common culprit when iron rusts and erodes. The powder sample from Alfa Aesar is a red powder, and thus is a very strong Raman scatterer under the red 647.1 nm excitation source. Because of the strong Raman signal,  $\alpha$ -Fe<sub>2</sub>O<sub>3</sub> was often used as a quick signal check to verify that the Raman system was aligned and working properly.

The spectrum of  $\alpha$ -Fe<sub>2</sub>O<sub>3</sub>, shown in Figure 23, is well known and will not be examined in detail [1]. However, the spectrum does give a good opportunity to recognize the resolution capabilities of the micro-Raman system. This spectrum was acquired at a very low laser power of 0.1 mW, achieved with neutral density filters. Without the neutral density filter, there is enough heating of the sample that thermal broadening makes the 291 and 298 cm<sup>-1</sup> modes difficult to resolve. In agreement with de Faria et al., the peak at approximately 295 cm<sup>-1</sup> is identified as a superposition of the 291 and 298 cm<sup>-1</sup> peaks. This peak resolved into two peaks is shown in Figure 24.

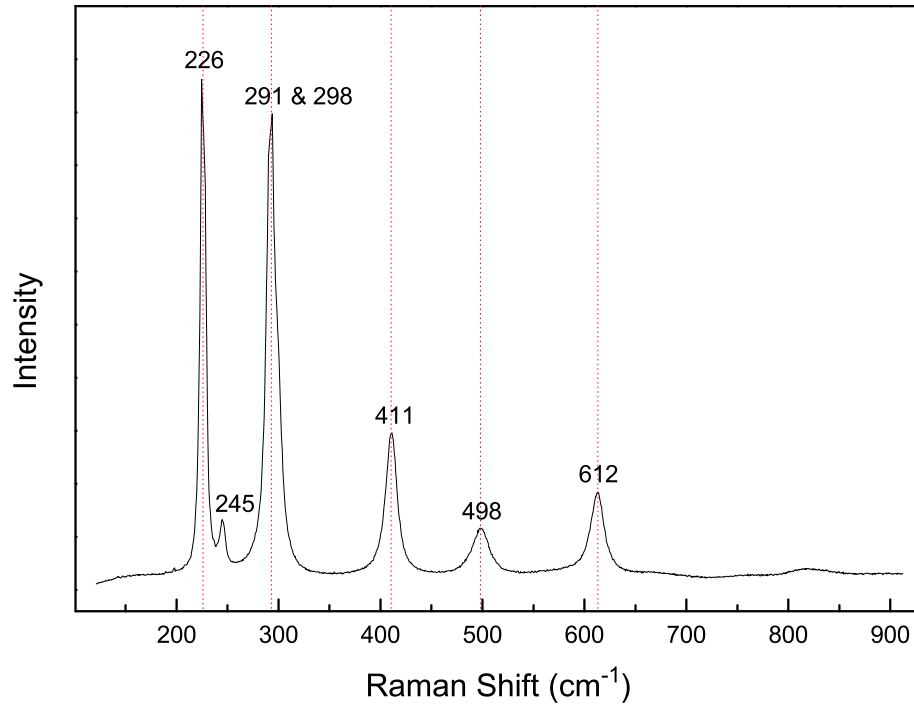


Figure 23. Raman spectrum of  $\alpha\text{-Fe}_2\text{O}_3$ . The laser power at sample is approximately 0.1 mW. The red lines indicate the position of the intense  $\alpha\text{-Fe}_2\text{O}_3$  modes and will be used in other figures for reference.

The Raman spectrum of  $\alpha\text{-Fe}_2\text{O}_3$  is well known, and as evident from Table 9, there is very good agreement of the seven Raman-active modes between data acquired in this work and the literature [1].

#### Magnetite, $\text{Fe}_3\text{O}_4$

Magnetite is an inverse spinel structured oxide, containing both  $\text{Fe}^{3+}$  and  $\text{Fe}^{2+}$  cations. The inversion indicates that the  $\text{Fe}^{3+}$  cations occupy the tetrahedral and half of the octahedral sites, whereas the  $\text{Fe}^{2+}$  iron cations occupy the remaining octahedral sites. The formula for magnetite is occasionally written as  $\text{Fe}^{3+}(\text{Fe}^{2+}\text{Fe}^{3+})\text{O}_4$ , where the parentheses represent equal occupancy of the octahedral site by the divalent and trivalent iron. The extra electron on the octahedral site can move around and thus

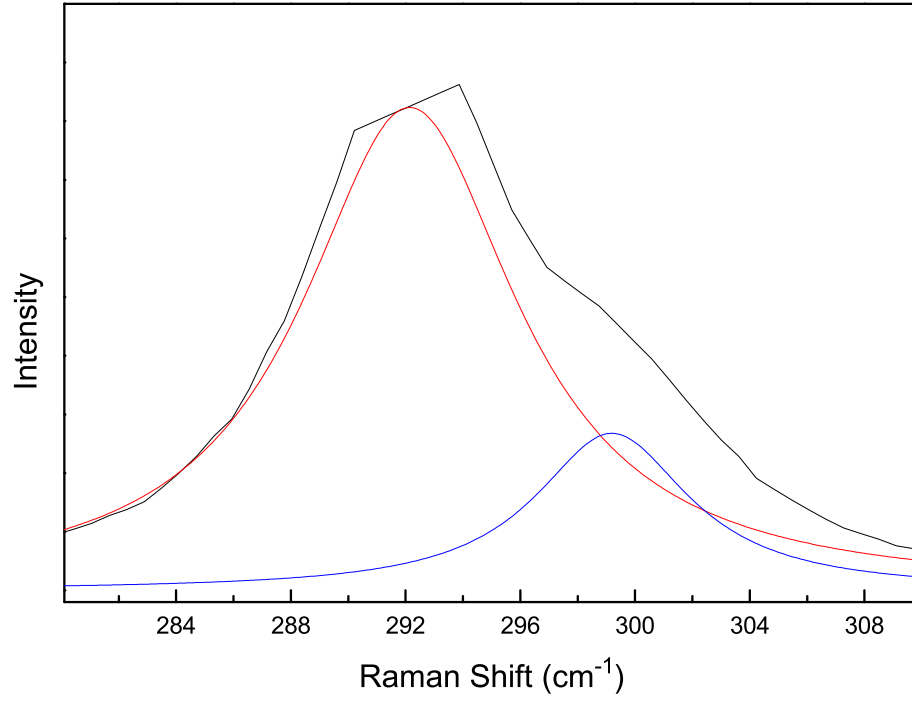


Figure 24. The two  $\alpha\text{-Fe}_2\text{O}_3$  modes at 291 and 298  $\text{cm}^{-1}$  can be fit accurately with two peaks using PeakFit.

This work	de Faria et al. [1]
226.0(3)	226.7
245.4(4)	245.7
291.8(3)	292.5
298.6(3)	299.3
410.8(3)	410.9
498.5(5)	497.1
612.8(4)	611.9

Table 9. Raman-active phonons, in  $\text{cm}^{-1}$ , of  $\alpha\text{-Fe}_2\text{O}_3$  compared to literature.

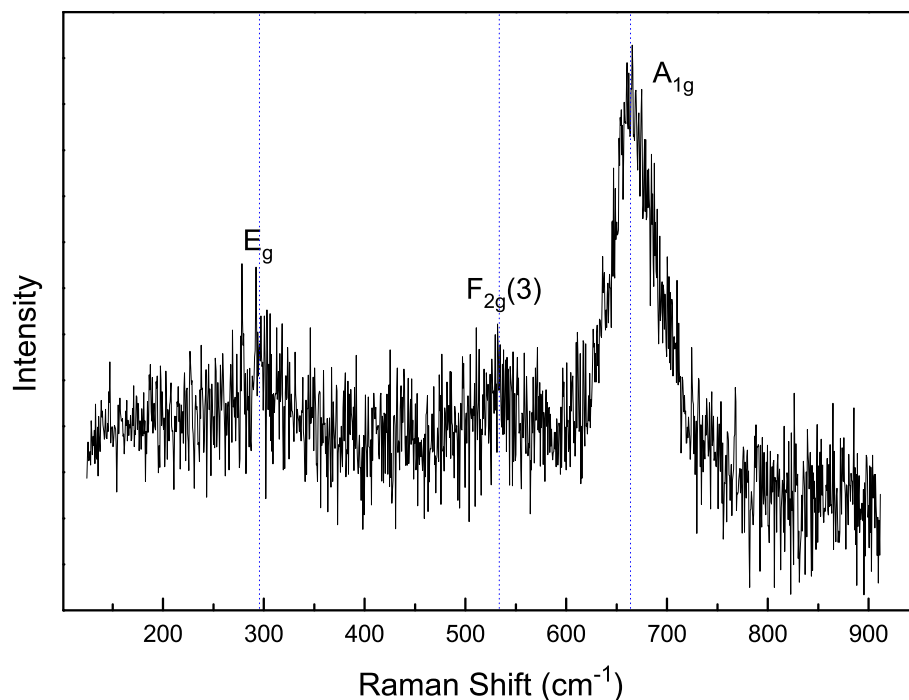


Figure 25. Raman spectrum of  $\text{Fe}_3\text{O}_4$ . The blue lines indicate the positions of the  $\text{Fe}_3\text{O}_4$  modes, and will be used in other figures for reference.

a valency of +2.5 is occasionally stated for the average valency of the iron occupying the octahedral site.

A Raman spectrum of  $\text{Fe}_3\text{O}_4$  is shown in Figure 25. The Raman spectrum of  $\text{Fe}_3\text{O}_4$  is also relatively well known, though there is no universal acceptance for the wavenumbers of the lower frequency modes, as evidenced in Table 10. Most of the literature reports a large peak around  $670\text{ cm}^{-1}$  as the  $A_{1g}$  phonon. This peak is easily observed with the Raman microscope in this experiment. Intensities of the other phonons are very weak, and only the  $E_g$  and  $F_{2g}(3)$  phonons were detected in the present work.

$\text{Fe}_3\text{O}_4$  easily oxidizes into  $\alpha\text{-Fe}_2\text{O}_3$  upon heating in air, which has been reported numerous times [1,51,121,129]. The effect is easily observed with our Raman system,

	This work	[45]	[1]	[51]
$F_{2g}(1)$	-	-		193
$E_g$	295(2)	-	301.6	306
	-	-	513.0	-
$F_{2g}(3)$	531(2)	542	533.6	538
$A_{1g}$	667(1)	671	662.7	668

Table 10. Raman-active phonons of  $Fe_3O_4$ , in  $cm^{-1}$ , compared to literature.

as shown in Figure 26. Increasing the laser power that illuminates a sample of pure  $Fe_3O_4$  powder begins to show  $\alpha$ - $Fe_2O_3$  modes in the Raman spectra above approximately 1 mW of laser power. The peaks shift to lower wavenumbers with increasing temperature resulting from the increasing laser power. Also, a visible red-colored spot appears on the black-colored magnetite sample where the laser is incident on the powder. The oxidation to  $\alpha$ - $Fe_2O_3$  is permanent; lowering the laser power does not cause the sample to revert to  $Fe_3O_4$ .

$Fe_3O_4$  does not immediately transition to  $\alpha$ - $Fe_2O_3$ . The literature reports an intermediate transition through maghemite,  $\gamma$ - $Fe_2O_3$  [1].  $\gamma$ - $Fe_2O_3$  also crystallizes into the spinel structure containing only  $Fe^{3+}$ , with 1/6 of the octahedral sites vacant [129, 130]. The Raman spectrum of maghemite has three broad features located at 350, 500, and 700  $cm^{-1}$  [1, 67, 131] and is easily recognized in Figure 26.

The temperature at which these conversions occur is only a few hundred degrees above room temperature. The literature differs slightly on the exact temperature. De Faria et al. reports that the conversion of magnetite to maghemite occurs at approximately 200°C, and the subsequent conversion to hematite occurs at 400°C [1]. Shebanova et al. studied magnetite at increasing laser powers and report that the hematite conversion began at 300°C, but did not report an intermediate  $\gamma$ - $Fe_2O_3$  phase [121].

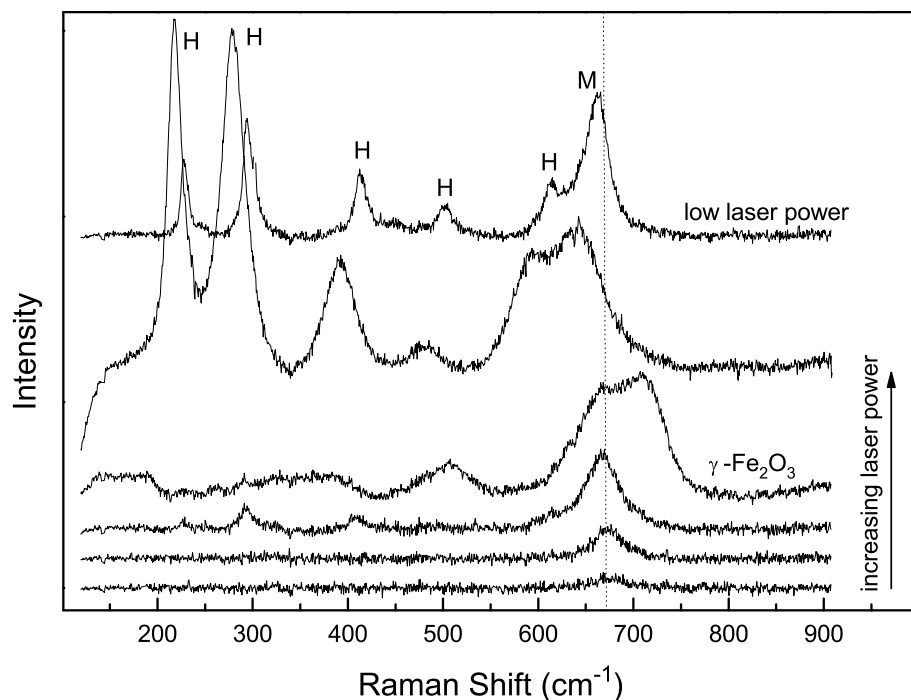


Figure 26. Raman spectra of  $\text{Fe}_3\text{O}_4$  as a function of increasing laser power from the krypton ion laser.  $\gamma\text{-Fe}_2\text{O}_3$  features appear just before the  $\alpha\text{-Fe}_2\text{O}_3$  features dominate the spectrum, indicating permanent conversion to  $\alpha\text{-Fe}_2\text{O}_3$ . In the top spectrum, (H) marks  $\alpha\text{-Fe}_2\text{O}_3$  modes and (M) marks the only visible  $\text{Fe}_3\text{O}_4$  mode.

Spectra acquired from a single spot on  $\text{Fe}_3\text{O}_4$  powder, taken as a function of increasing laser power, can be seen in Figure 26. The broad maghemite features appear just before the intense hematite modes dominate the spectrum. The permanence of the conversion is evident. The Raman spectrum is still characteristic of hematite after lowering the laser power back to the original low power, as evident in the top spectrum of Figure 26. Nevertheless, the sample is not completely converted. The main  $A_{1g}$  peak of the  $\text{Fe}_3\text{O}_4$  powder is still visible in all spectra.

The  $A_{1g}$  mode of the intermediate  $\gamma\text{-Fe}_2\text{O}_3$  phase was fitted with two peaks, to represent the occupied and unoccupied octahedral sites. The low-frequency side of the mode has a frequency of  $669\text{ cm}^{-1}$ , in agreement with the  $A_{1g}$  mode of  $\text{Fe}_3\text{O}_4$ ,



647.1 nm	514.5 nm	Mougin et al. [44]
305	310	296.3
353	351	350.4
530	531	528.5
556	552	554.2
617	609	615.0

Table 11. Raman-active phonons, in  $\text{cm}^{-1}$ , of  $\text{Cr}_2\text{O}_3$ , acquired with the krypton (647.1 nm) and argon (514.5 nm) lasers, compared to literature.

which would represent the octahedral sites occupied by iron. The high-frequency side of the mode is located at  $710 \text{ cm}^{-1}$ , in agreement with Boucherit et al., who also report  $710 \text{ cm}^{-1}$  for the high-frequency side of this mode [67]. This may be evidence of this shoulder of the  $A_{1g}$  mode being due to vacancies on some of the octahedral sites.

#### Chromium oxide, $\text{Cr}_2\text{O}_3$

The green chromium oxide powder,  $\text{Cr}_2\text{O}_3$ , also has a well characterized Raman spectrum [44]. The powder fluoresces under the red 647.1 nm excitation source and the large amount of longer wavelengths emitted from the fluorescence creates a large background that overwhelms the Raman spectrum, as shown previously in Figure 22. This motivated the use of the argon ion laser, tuned to 514.5 nm. The spectrum is seen in Figure 27, demonstrating that the use of the green excitation source eliminated the fluorescence background from the Raman spectrum of  $\text{Cr}_2\text{O}_3$ . The  $\text{Cr}_2\text{O}_3$  lines detected with both the krypton laser (Figure 22) and argon laser (Figure 27) agree well with the literature, as seen in Table 11.

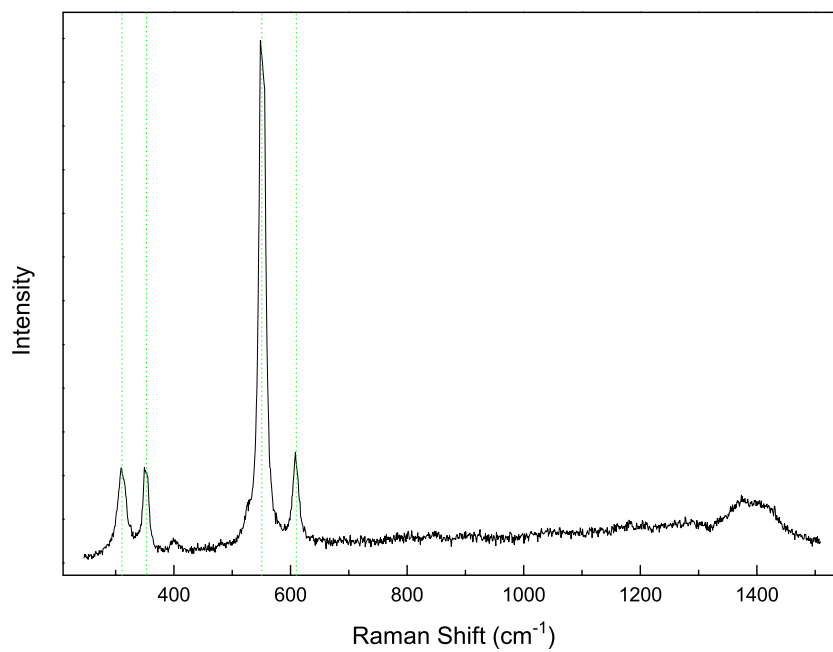
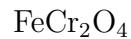


Figure 27. Raman spectrum of  $\text{Cr}_2\text{O}_3$  taken with the 514.5 nm emission line of an argon laser. The green lines represent the positions of  $\text{Cr}_2\text{O}_3$  Raman-active modes and will be used in other figures for reference.

## CHAPTER 7

### CHROMITES & FERRITES

All of the spinels synthesized and studied in the present work are II-III spinels, having +2 and +3 cations occupying the tetrahedral and octahedral sites of the lattice. The lattice parameters of all synthesized  $AB_2O_4$  spinels, determined from the x-ray diffraction data, are shown in Table 6 and agree well with the literature. Full Rietveld refinement results are shown in Appendix A.



Iron chromite,  $FeCr_2O_4$ , is a normal spinel, with  $Fe^{2+}$  occupying all of the tetrahedral sites of the lattice.  $FeCr_2O_4$  is a very common element within the Earth, and it is surprising that little Raman data exists on this mineral in its pure form. Existing data is often from natural chromite ore samples containing magnesium and aluminum impurities. The Raman-active modes from different studies are listed in Table 12.  $FeCr_2O_4$  from the present study is also included. The  $FeCr_2O_4$  data from Wang et al. is obtained from a sample that contains 3.5%  $Al_2O_3$  by weight, and 8% Mg in the tetrahedral sites [9]. The meteorite sample from Chen et al. contains approximately 2.5% MgO, 3%  $TiO_2$ , and 6%  $Al_2O_3$ , by weight percent [19]. McCarty et al. only assign the intense peak at  $686\text{ cm}^{-1}$  as the  $A_{1g}$  mode [45].

The Raman spectrum of  $FeCr_2O_4$  can be seen in Figure 28. The spectrum is very similar to the Raman spectrum of  $Fe_3O_4$ . Only two modes are intense enough to be distinguished from the background noise. The  $A_{1g}$  phonon is located at  $678\text{ cm}^{-1}$ , greater than the  $A_{1g}$  position of  $Fe_3O_4$ , located at  $667\text{ cm}^{-1}$ .

	This Work	[45]	[9]	[19]
$F_{2g}(3)$	531(1)		522	500
shoulder	635(2)		639	595
$A_{1g}$	678(1)	686	684	677

Table 12. Raman-active phonons, in  $\text{cm}^{-1}$ , of  $\text{FeCr}_2\text{O}_4$  compared to literature.

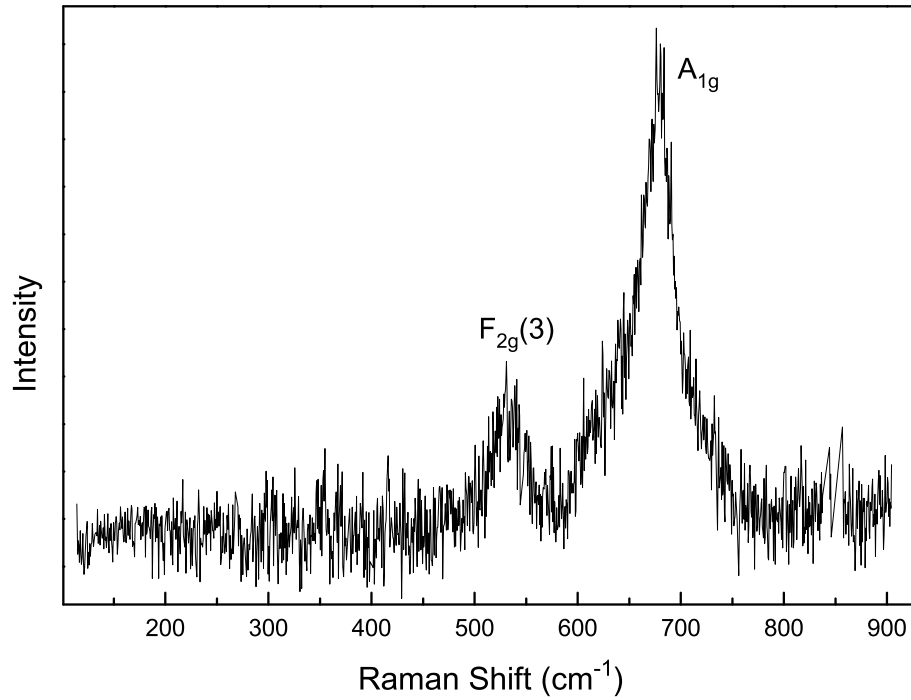


Figure 28. Raman spectrum of  $\text{FeCr}_2\text{O}_4$ .

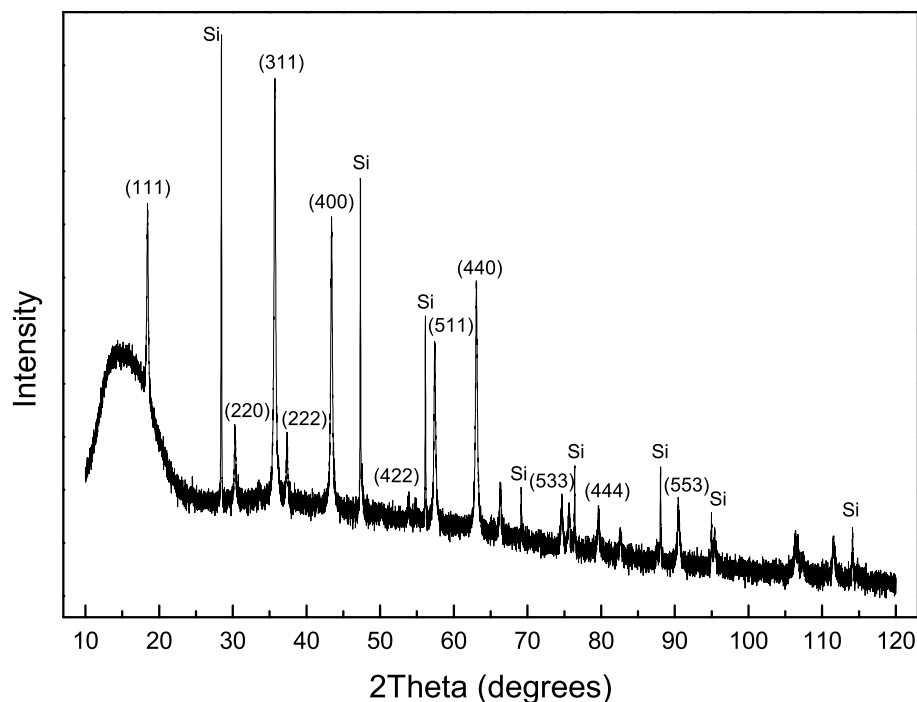


Figure 29. X-ray diffraction spectrum of  $\text{MgCr}_2\text{O}_4$ .



Magnesium chromite,  $\text{MgCr}_2\text{O}_4$ , is also a normal spinel. The x-ray diffraction spectrum of  $\text{MgCr}_2\text{O}_4$ , characteristic of all of the spinels, can be seen in Figure 29. The synthesized spinel contains less than 2% corundum phase impurity. Four out of the five predicted Raman-active modes, reported by Wang et al. [48], are detected. These detected modes of  $\text{MgCr}_2\text{O}_4$  are shown in Figure 30, and agree well with the literature [48].

Acquired spectra from multiple spots on the sample demonstrated nonuniformity: two additional modes were detected in some of the spectra, as shown in Figure 30(a). Wang et al. suggest that the  $361.9$  and  $792.1\text{ cm}^{-1}$  features they detected may be due to partial inversion of the  $\text{Mg}^{2+}$  and  $\text{Cr}^{3+}$  cations [48]. Cation disorder has often

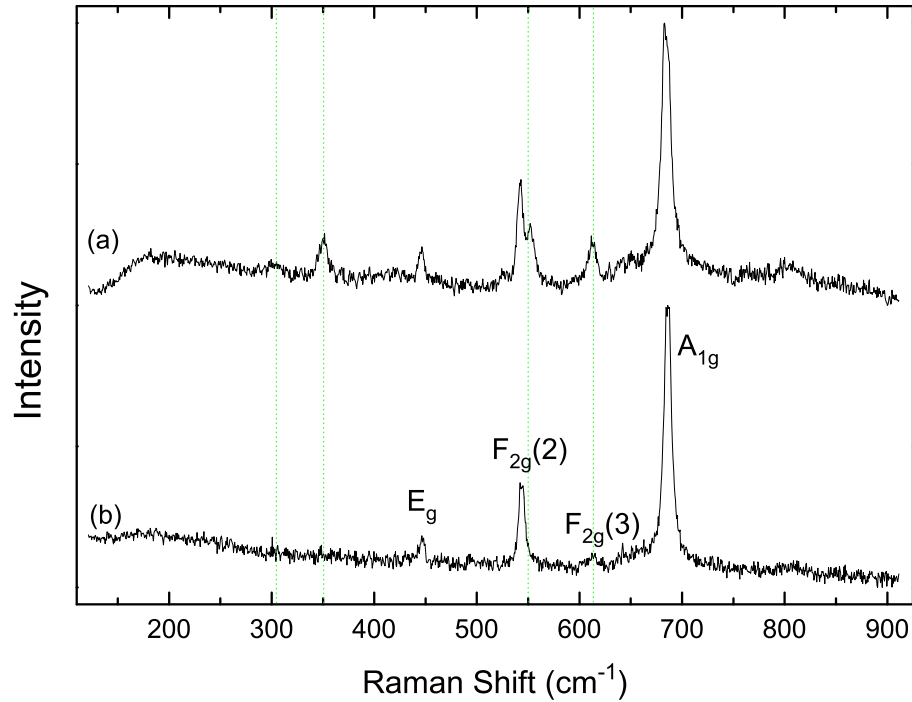


Figure 30. Two different Raman spectra of  $\text{MgCr}_2\text{O}_4$ : one (a) with additional Raman-active mode, and (b) after heating the sample to  $700^\circ\text{C}$  for 24 hrs, the extra modes are not detected. The green reference lines indicate the wavenumbers of the Raman-active modes of  $\text{Cr}_2\text{O}_3$ .

been attributed as the cause of the extra features in the Raman spectrum of  $\text{MgAl}_2\text{O}_4$  spinel [2, 7, 40]. The second additional feature is a shoulder on the high-frequency side of the  $F_{2g}(2)$  mode. This shoulder was detected in all spectra showing the  $351\text{ cm}^{-1}$  feature, indicating that they are due to the same phenomenon. This phonon was not reported by Wang et al. in their work [48]. The wavenumbers of these additional modes match very well with the spectrum of  $\text{Cr}_2\text{O}_3$ , and are indicated by the green lines in Figure 30. The additional features are removed after heating the sample to  $700^\circ\text{C}$  for a period of 24 hrs and all spectra acquired from different spots on the sample then resemble Figure 30(b).

Extra phonons in the Raman spectra of  $\text{MgAl}_2\text{O}_4$  have been previously attributed

This work	Wang et al. [48]
-	226.5
350(2)	361.9
446(1)	446.9
542(1)	544.1
612(1)	614.1
685(1)	686.8
-	792.1

Table 13. Raman-active phonons of  $\text{MgCr}_2\text{O}_4$  compared to literature.

to cation inversion [2, 7, 40]. However, work by Cynn et al. who show that the cation disorder occurs in natural spinels after increasing the temperature to 1200K and remains so after quenching [7]. Because no additional features appear after heating the sample to 700°C, the extra modes are probably not a result of cation disorder, and instead due to the small amount, roughly 3%, of  $\text{Cr}_2\text{O}_3$  detected in the sample by x-ray diffraction.

The Raman-active mode reported by Wang et al. at  $226.5 \text{ cm}^{-1}$  [48] was not detected in the spectrum of pure  $\text{MgCr}_2\text{O}_4$  acquired in this study. The feature is probably too weak to be distinguished from the background, since Wang et al. also show a very weak intensity for this mode [48]. Evidence that a feature exist in this area is supported by examining the entire  $\text{Mg}_x\text{Ni}_{1-x}\text{Cr}_2\text{O}_4$  series, presented in the next chapter, and noticing that the lowest  $F_{2g}(1)$  mode increases from  $190 \text{ cm}^{-1}$  at  $x = 0$  to  $210 \text{ cm}^{-1}$  at  $x = 0.9$ . This  $F_{2g}(1)$  mode decreases in intensity as the magnesium content is increased.

### $\text{NiCr}_2\text{O}_4$

$\text{NiCr}_2\text{O}_4$  undergoes a first order phase transition to spinel at approximately 310 K from the tetragonal space group  $I4_1/amd$  [132–134]. This is due to a Jahn-Teller dis-

tortion of the  $\text{Ni}^{2+}$  tetrahedron [54]. As Dunitz et al. report, the Jahn-Teller distortion exists above the 310 K, but the random orientation of the distortion within the spinel lattice makes the lattice appear statistically as spinel phase [54]. Only below the transition temperature does the lattice become ordered enough to identify the tetragonal distortion. As the transition temperature is very close to room temperature, XRD data reflects the presence of the tetragonal  $\text{NiCr}_2\text{O}_4$  phase.

Wojtowicz reported the coexistence of cubic and tetragonal phases of  $\text{NiCr}_2\text{O}_4$  between 27°C and 34°C [134]. At 27°C, the  $c/a$  ratio of the tetragonal phase is 1.022, and never decreases below 1.016 within the phase transition temperature range.

Several  $\text{NiCr}_2\text{O}_4$  samples were synthesized and treated differently following the combustion synthesis. Several samples were left untreated following the combustion. Two samples were heated in air: one was heated to a temperatures of 400°C, the other heated to 700°C. One sample was cooled to -10°C by placing it into a common freezer for 48 hrs. Another sample was placed into the reducing environment of flowing hydrogen and argon gas at a temperature of 500°C for 24 hrs, as detailed in the synthesis section. X-ray diffraction was performed on all of these samples and repeated on some of the untreated samples. Both the spinel and tetragonal phases are detected in all samples in varying amounts. Performing a Rietveld refinement with only the  $I4_1/amd$  or spinel phase results in a very poor fit compared to the refinement using both cubic and tetragonal phases. Repeated data on untreated samples showed inconsistent ratios between cubic and tetragonal  $\text{NiCr}_2\text{O}_4$ . This may be a result of fluctuating temperatures within the XRD laboratory. The temperature of the room is controlled by the air conditioning unit of the room. The temperature of the samples in the Bruker instrument was not measured by the instrument. It is also possible that the grinding the powder for preparation may trigger the tetragonal transformation. Full Rietveld refinement results on the  $\text{NiCr}_2\text{O}_4$  samples is shown in Appendix A.



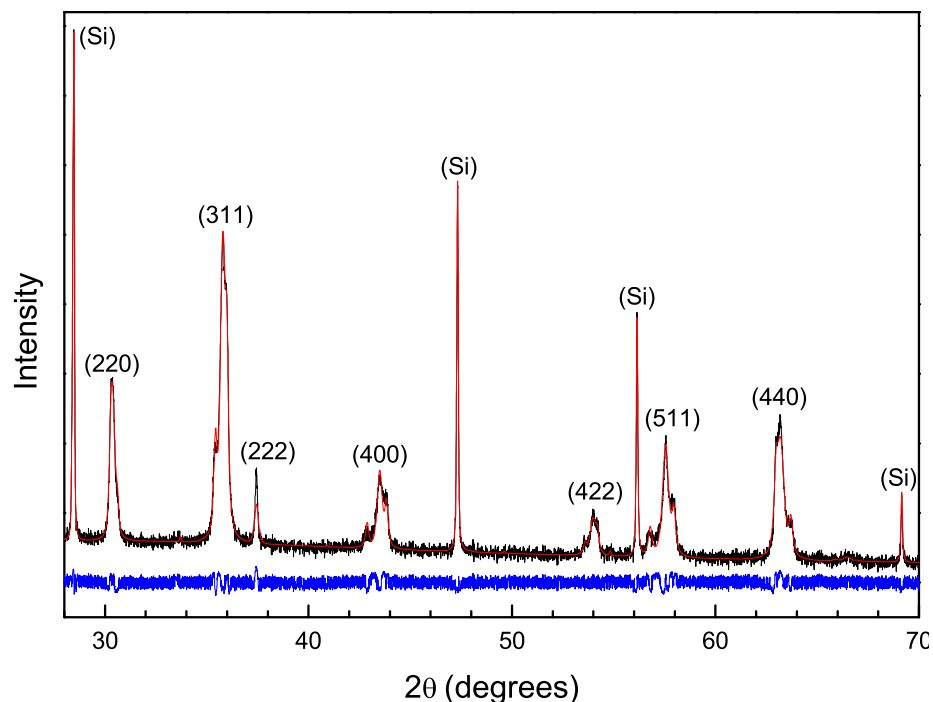


Figure 31. Diffraction spectrum of  $\text{NiCr}_2\text{O}_4$  heated to  $700^\circ\text{C}$  in air. A smaller angle selection is shown to emphasize the splitting of the  $\text{NiCr}_2\text{O}_4$  diffraction peaks, which is due to the presence of tetragonal phase  $\text{NiCr}_2\text{O}_4$ , in addition to the spinel phase.

The diffraction spectrum of  $\text{NiCr}_2\text{O}_4$  heated to  $700^\circ\text{C}$  in air can be seen in Figure 31, which is characteristic of all  $\text{NiCr}_2\text{O}_4$  samples. The samples were fitted with both spinel and tetragonal phases within the powder samples, indicating varying ratios of spinel to tetragonal phase present. However, the lattice parameters are consistent among the different samples and agree well with the literature. Table 14 displays some of the prepared  $\text{NiCr}_2\text{O}_4$  samples compared to previous work.

The  $c/a$  ratio for the tetragonal phase of all samples is between 1.022 and 1.016, lending support to the hypothesis that the samples are within the two-phase region of the transition range. During this two-phase regime, there should be a correlation between the amount of cubic and tetragonal phases, and the  $c/a$  ratio of the tetragonal

NiCr <sub>2</sub> O <sub>4</sub>	lattice parameter (Å)	
	spinel	tetragonal
Crottax et al. [132]	a = 8.3155(7)	a = 5.8369(4) c = 8.4301(6)
Ziemniak et al. [127]	a = 8.3186	a = 5.8418 c = 8.4337
Untreated sample	a = 8.3178(3)	a = 5.8412(2) c = 8.4275(4)
Cooled to -10°C for 48 hrs	a = 8.3185(3)	a = 5.8405(2) c = 8.4329(4)
Reduced at 500°C for 24hrs	a = 8.3189(3)	a = 5.8414(3) c = 8.4290(5)

Table 14. Lattice parameters of cubic and tetragonal NiCr<sub>2</sub>O<sub>4</sub>. The first two are values reported from the literature [127, 132] while the latter three are samples from the present work.

phase, although, as Wojtowicz reports, the ratio should not fall below 1.016 [134]. Figure 32 plots the  $c/a$  ratio versus the ratio of the amount of cubic phase to tetragonal phase. The correlation is not strong, but is consistent with a decreasing  $c/a$  ratio as the proportion of spinel phase NiCr<sub>2</sub>O<sub>4</sub> increases. The uncertainties of each ratio were calculated by summing the individual percent uncertainties of  $a$  and  $c$  in quadrature.

The introduction of another cation into the tetrahedral position of the lattice, such as Fe<sup>3+</sup> or Mg<sup>2+</sup>, removes the Jahn-Teller distortion at this temperature. No XRD spectra on Mg<sub>0.1</sub>Ni<sub>0.9</sub>Cr<sub>2</sub>O<sub>4</sub> or NiFe<sub>0.05</sub>Cr<sub>1.95</sub>O<sub>4</sub> exhibited the tetragonal distortion, and instead resemble the x-ray diffraction spectrum shown in Figure 29.

The Raman spectrum of NiCr<sub>2</sub>O<sub>4</sub> is shown in Figure 33. Four of the five Raman lines predicted for spinel are detected here. The E<sub>g</sub> and F<sub>2g</sub>(2) modes agree well with the spectrum reported by Wang et al. [47], shown in Table 15. There is a small deviation to smaller wavenumber for the F<sub>2g</sub>(1) and A<sub>1g</sub> modes. The F<sub>2g</sub>(3) mode was too weak to be distinguished from the background. Wang et al. locate this mode

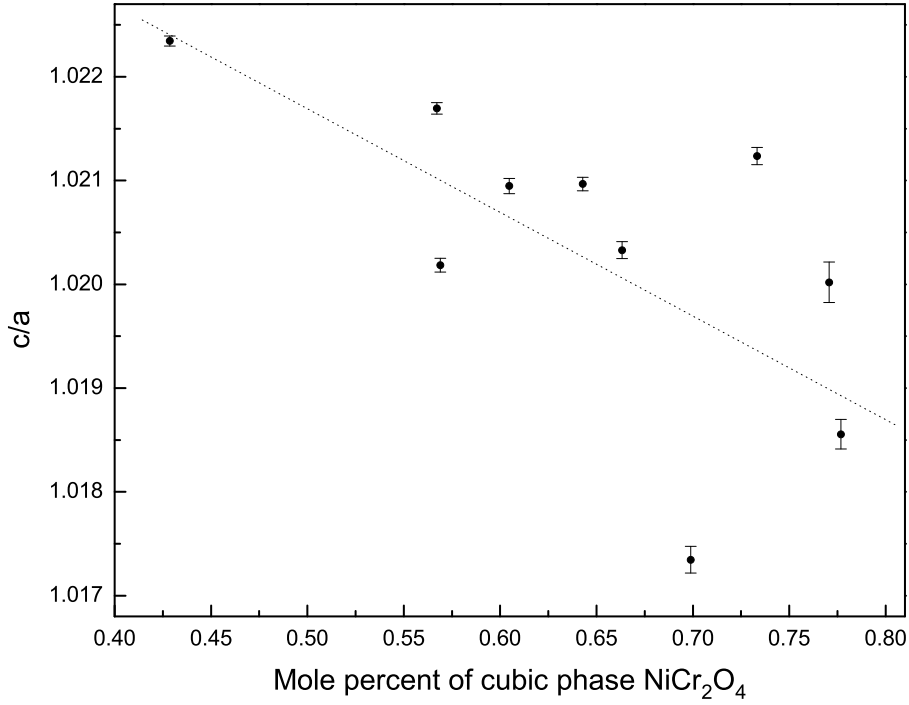


Figure 32.  $c/a$  ratio of tetragonal phase  $\text{NiCr}_2\text{O}_4$  as the amount of cubic phase increases. A line is drawn as a rough guide for the eye.

at a Raman shift of  $580 \text{ cm}^{-1}$ .



$\text{NiFe}_2\text{O}_4$  is an inverse spinel, with the tetrahedral sites completely filled with  $\text{Fe}^{3+}$ , and the octahedral sites occupied in equal molar amounts by the remaining  $\text{Fe}^{3+}$  and  $\text{Ni}^{2+}$  cations. This inversion occurs because nickel has a higher preference for the octahedral sites than iron [50]. The Raman spectrum of  $\text{NiFe}_2\text{O}_4$  is shown in Figure 34 and agrees well with the literature [64]. The  $F_{2g}(2)$ ,  $F_{2g}(3)$ , and  $A_{1g}$  modes all have shoulders. Graves et al. examined a single crystal sample of  $\text{NiFe}_2\text{O}_4$  to identify the character of some of these shoulders [109]. They assigned the low-frequency shoulder of the  $A_{1g}$  mode as having  $E_g$  character and the low-frequency

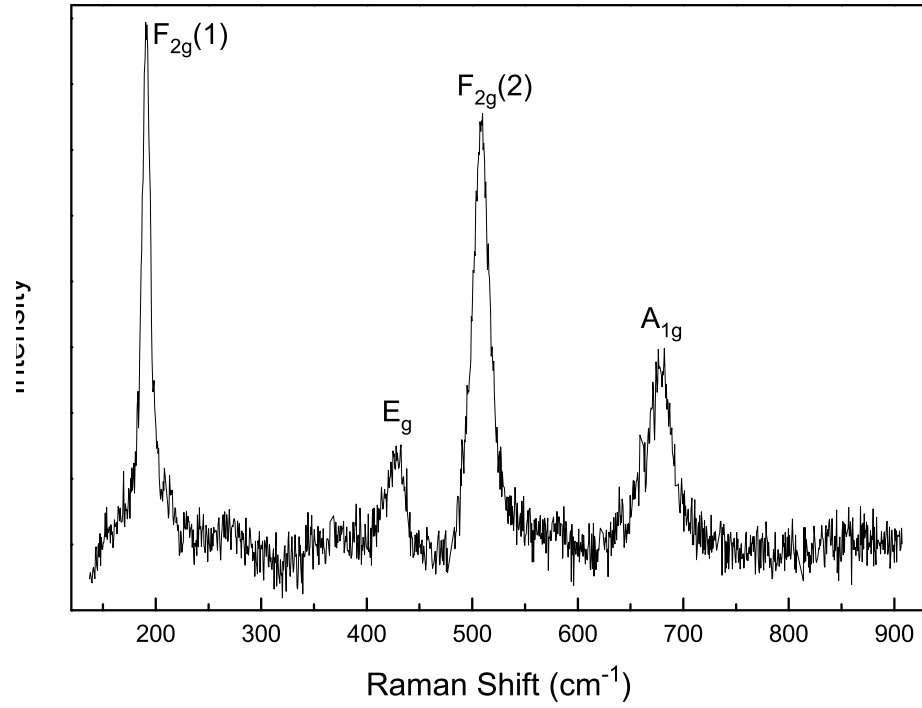


Figure 33. Raman spectrum of  $\text{NiCr}_2\text{O}_4$ .

$\text{NiCr}_2\text{O}_4$	This work	Wang et al. [47]
$F_{2g}(1)$	191(1)	181
$E_g$	429(1)	425
$F_{2g}(2)$	508(1)	511
$F_{2g}(3)$	-	580
$A_{1g}$	676(2)	686

Table 15. Raman-active phonons of  $\text{NiCr}_2\text{O}_4$  compared to literature.

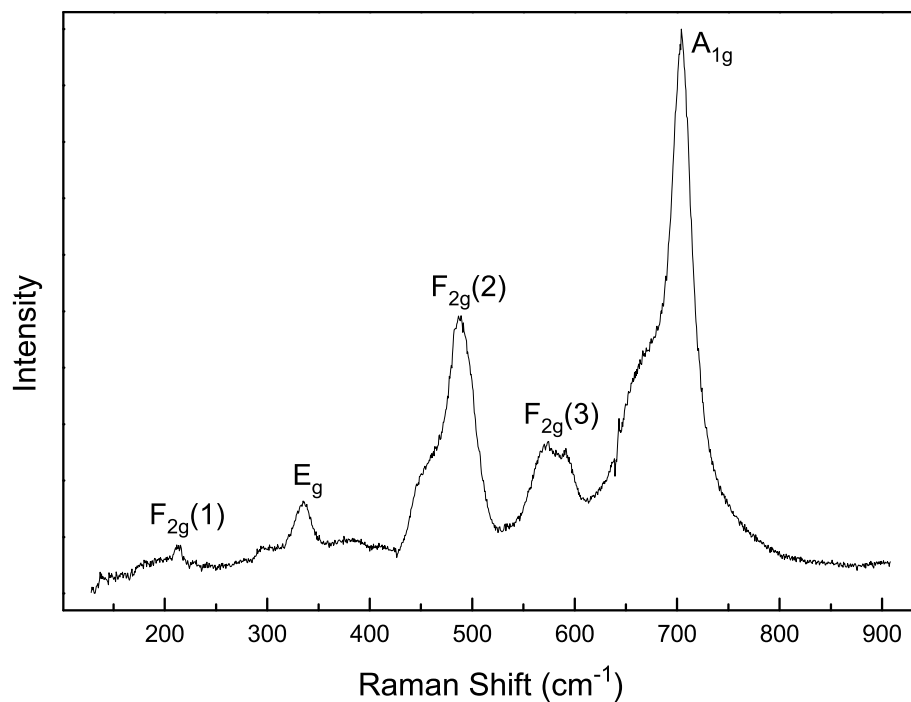


Figure 34. Raman spectrum of NiFe<sub>2</sub>O<sub>4</sub>.

shoulder of the F<sub>2g</sub>(3) mode as having A<sub>1g</sub> character. The position of the Raman lines and shoulders can be seen in Table 16.

A possible explanation of these extra modes is the inversion of the NiFe<sub>2</sub>O<sub>4</sub> lattice. The existence of both Fe<sup>3+</sup> and Ni<sup>2+</sup> occupying the octahedral sites leads to separate vibrational frequencies for the NiO<sub>6</sub> and FeO<sub>6</sub> octahedra. The A<sub>1g</sub> mode of LiMn<sub>2</sub>O<sub>4</sub> has a similar structure as NiFe<sub>2</sub>O<sub>4</sub>, which Hwang et al. attribute to the presence of Mn<sup>3+</sup>O<sub>6</sub> and Mn<sup>4+</sup>O<sub>6</sub> [90]. These additional modes will be examined further in the discussion on NiFe<sub>x</sub>Cr<sub>2-x</sub>O<sub>4</sub>.

NiFe <sub>2</sub> O <sub>4</sub>	This Work	Kim et al. [64]	Graves et al. [109]
shoulder	189(2)		
F <sub>2g</sub> (1)	211(1)		
E <sub>g</sub>	333(1)		339
shoulder	456(1)	460	
F <sub>2g</sub> (2)	487(1)	492	490
shoulder	568(1)	574	579 (A <sub>1g</sub> )
F <sub>2g</sub> (3)	590(1)	595	
shoulder	663(2)	654	666 (E <sub>g</sub> )
A <sub>1g</sub>	704(1)	702	700

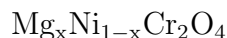
Table 16. NiFe<sub>2</sub>O<sub>4</sub> Raman-active phonons compared to literature.

## CHAPTER 8

### SOLID SOLUTION SPINELS

A solid solution assumes substitution on the octahedral or tetrahedral sites with a different cation species. This is very different than a simple mixture of the two end-member crystals. The solid solutions synthesized from the combustion reaction must be tested whether or not the solid solution is actually formed, or if only a heterogeneous mixture of two pure spinels is created. This was directly tested using the  $\text{NiFe}_x\text{Cr}_{2-x}\text{O}_4$  system. Pure  $\text{NiCr}_2\text{O}_4$  and  $\text{NiFe}_2\text{O}_4$  were mixed in a 3:1 ratio and compared to  $\text{NiFe}_x\text{Cr}_{2-x}\text{O}_4$  with  $x = 0.5$ . Raman spectra of each sample are shown in Figure 35 and show that the mixture is a sum of the two pure spinels  $\text{NiCr}_2\text{O}_4$  and  $\text{NiFe}_2\text{O}_4$ . Lines from both pure  $\text{NiCr}_2\text{O}_4$  and  $\text{NiFe}_2\text{O}_4$  are present in the spectrum. Summation of the two individual spectra of  $\text{NiCr}_2\text{O}_4$  and  $\text{NiFe}_2\text{O}_4$  does not result in the same spectrum as the solid solution sample..

Cunha et al. assumed a linear change in phonon frequency for the different mixed oxides as the  $\text{Ni}^{2+}$  cation is substituted for  $\text{Fe}^{2+}$  in the  $\text{Ni}_x\text{Fe}_{3-x}\text{O}_4$  system [24]. The Raman spectra of pure spinels are well known in the literature, but complete vibrational data is lacking for many of these mixed metal oxides. As will be seen from data presented in this chapter, the change in wavenumber of the Raman-active vibrations is not necessarily linear for these mixed spinels as cation content is varied.



Both  $\text{MgCr}_2\text{O}_4$  and  $\text{NiCr}_2\text{O}_4$  are normal spinels. The  $\text{Mg}_x\text{Ni}_{1-x}\text{Cr}_2\text{O}_4$  series provides a good opportunity to examine how the vibrational modes of a normal II-III

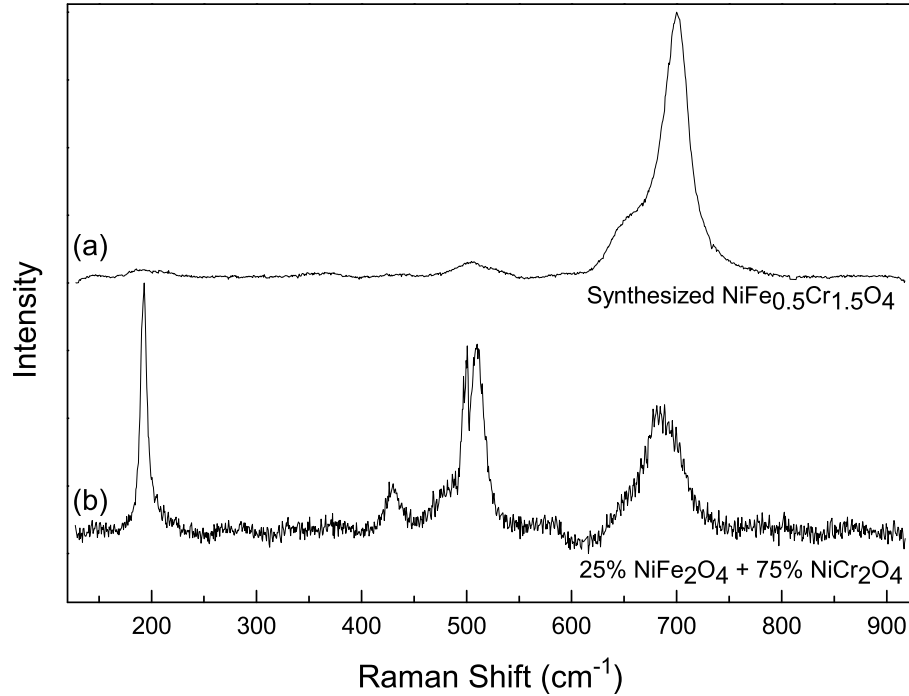


Figure 35. (a) Raman spectrum of a synthesized solid solution of  $\text{NiFe}_x\text{Cr}_{2-x}\text{O}_4$  with  $x = 0.5$ , and (b) a mixture containing 25%  $\text{NiFe}_2\text{O}_4$  and 75%  $\text{NiCr}_2\text{O}_4$  by weight (bottom).

spinel are affected as only the divalent cation is exchanged from nickel to magnesium. The octahedral position is occupied by the trivalent chromium cation for all  $x$  in the series. Nickel has a significantly larger mass than magnesium. Therefore, from a simple mass on a spring model, substitution of the nickel atoms with the lighter magnesium atoms should lead to higher vibrational frequencies.

All samples of the  $\text{Mg}_x\text{Ni}_{1-x}\text{Cr}_2\text{O}_4$  series were synthesized twice to confirm consistency of the synthesis method. The lattice parameters from both sets of synthesized samples are consistent and increase as nickel is substituted by magnesium. This increase in the lattice parameter, shown in Figure 36, deviates from linear, given (in Ångstroms) by:  $y = 8.31882(9) + 0.02054(4)x - 0.00506(4)x^2$ , where  $x$  is the amount



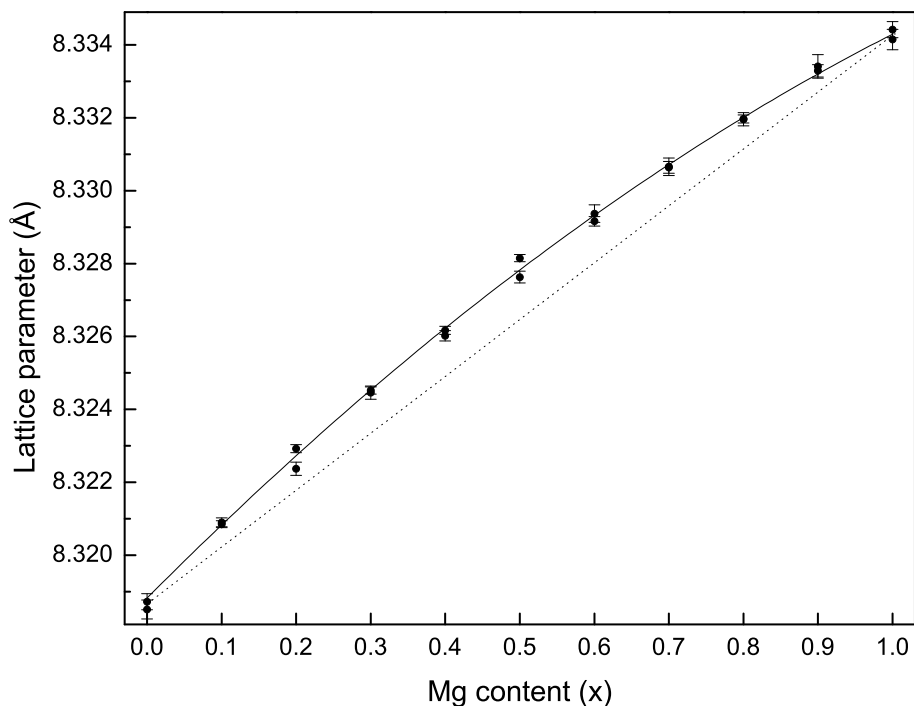


Figure 36. Lattice constants of  $\text{Mg}_x\text{Ni}_{1-x}\text{Cr}_2\text{O}_4$ . The dashed line represents a linear guide for the eye.

of magnesium in  $\text{Mg}_x\text{Ni}_{1-x}\text{Cr}_2\text{O}_4$ . The numbers in the parentheses represent the error in the last digit.

The Raman spectra of the  $\text{Mg}_x\text{Ni}_{1-x}\text{Cr}_2\text{O}_4$  series can be seen in Figure 37. All Raman-active modes are detected, though some modes are very weak and difficult to distinguish from background noise across the entire series. The highest-frequency  $F_{2g}(3)$  mode is undetected in  $\text{NiCr}_2\text{O}_4$  and only appears in the high chromium end of the series, emerging at a magnesium content of  $x = 0.9$ , and with a wavenumber of  $611\text{ cm}^{-1}$  in the pure  $\text{MgCr}_2\text{O}_4$  sample. Wang et al. report this mode to be located at  $580\text{ cm}^{-1}$  for pure  $\text{NiCr}_2\text{O}_4$  [47].

The wavenumbers of all Raman-active modes, and of the infrared-active  $\nu_3$  mode, of  $\text{Mg}_x\text{Ni}_{1-x}\text{Cr}_2\text{O}_4$  are plotted versus magnesium composition in Figure 38. All

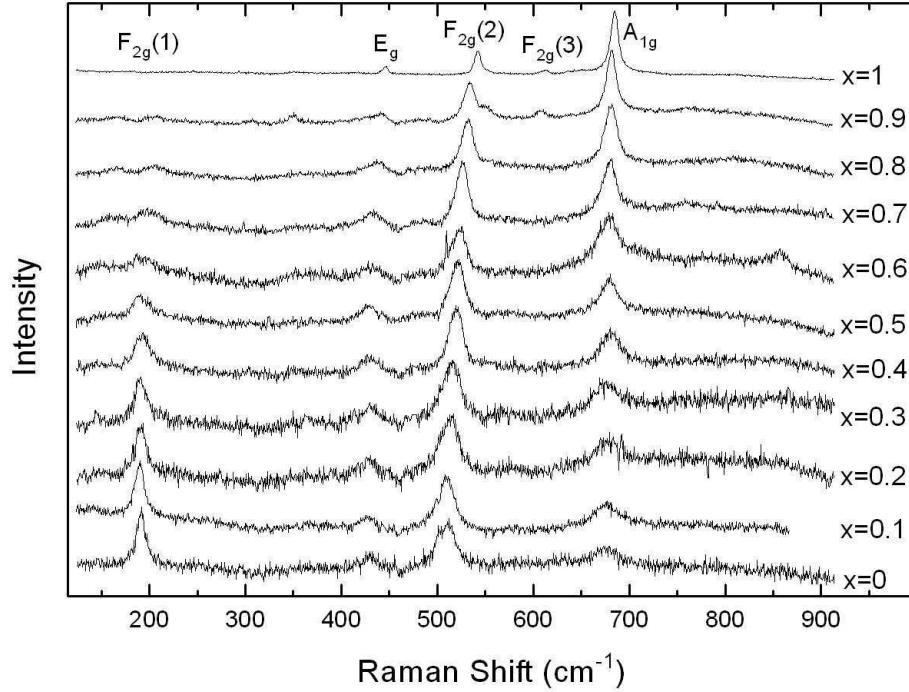


Figure 37. Raman spectra of  $\text{Mg}_x\text{Ni}_{1-x}\text{Cr}_2\text{O}_4$ .

Raman-active modes display an increase in wavenumber as the nickel cation is replaced with magnesium. The wavenumber of the  $F_{2g}(2)$  mode increases fairly linearly. However, the  $E_g$  and  $F_{2g}(1)$  modes exhibit nonlinear behavior. Only a small increase in wavenumber occurs until approximately  $x = 0.6$ . Above this iron content, the wavenumbers of the modes increase to the wavenumbers of the end member  $\text{MgCr}_2\text{O}_4$ ,  $x = 1$ . The increase in wavenumber of the  $F_{2g}(1)$  mode is discontinuous at  $x = 0.6$ .

The largest overall change in Raman phonon frequencies is found from the lower-frequency modes,  $F_{2g}(1)$ ,  $E_g$ , and  $F_{2g}(2)$ , with respective percent changes of 8.4%, 4.0%, and 6.6%. In contrast, the  $A_{1g}$  mode only changed by 1.1%. This supports the claim put forth by Preudhomme et al. that the high-frequency phonons have a

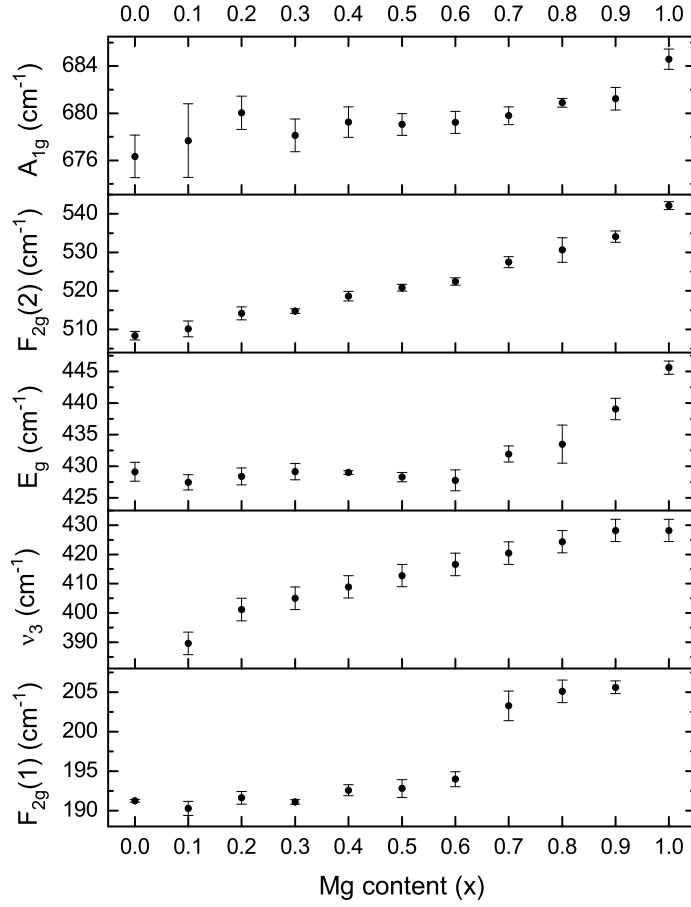


Figure 38. Vibrational mode peak positions of  $\text{Mg}_x\text{Ni}_{1-x}\text{Cr}_2\text{O}_4$ .

stronger dependence on the octahedral cations and the lower frequency vibrations depend more strongly upon the tetrahedral cations [88]. Exchanging the octahedral cation, as in the  $\text{MgCr}_x\text{Al}_{2-x}\text{O}_4$  series studied by Malézieux et al., shows an 11% increase in the  $A_{1g}$  mode [116].

The  $F_{2g}(2)$  mode, located in the  $500\text{-}550\text{ cm}^{-1}$  range, has a slight dependence on the tetrahedral cation. However, this mode is reported to be located at  $492\text{ cm}^{-1}$  for  $\text{MgAl}_2\text{O}_4$  [87]. This is a 10% shift from the peak position in  $\text{MgCr}_2\text{O}_4$ , again showing a greater dependence on the octahedral cation.

The  $E_g$  mode of  $Mg_xNi_{1-x}Cr_2O_4$  changes by 4% upon magnesium substitution. Malézieux et al. show that  $MgAl_2O_4$  exhibits a larger dependence on the octahedral cation with an increase of about 7% in the frequency of this mode [116]. Gupta et al. calculate an expression for the  $E_g$  mode that shows negligible dependence on the force constant of the oxygens bonded to the tetrahedral cation [135]. Laguna-Bercero et al. argue that the  $E_g$  mode is strongly correlated with the bond distance of the oxygen atoms bonded to the octahedral cations and that the decrease in the  $E_g$  position of  $NiAl_2O_4$  is due to a longer B-O bond [41]. These two ideas suggest that substitution of the tetrahedral cation should have little influence upon the wavenumber of the  $E_g$  mode. The B-O bond distance can be calculated using the  $a$  and  $u$  parameters of the spinel lattice from Equation 2.2 [42]. This bond distance is shown in Figure 39 for the  $Mg_xNi_{1-x}Cr_2O_4$  series. In contrast to what Laguna-Bercero et al. argue for  $NiAl_2O_4$ , the B-O bond distance increases as the magnesium content increases, corresponding with an increase in the  $E_g$  mode. The B-O bond distance increase is relatively linear, unlike the increase in wavenumber of the  $E_g$  mode, which dramatically increases at  $x = 0.7$ .

As previously stated, most literature suggests that the  $F_{2g}(1)$  mode is a translational motion of the entire tetrahedral  $AO_4$  unit within the lattice [8, 79, 114]. Our data support the view that this vibration involves the tetrahedral cation, as this mode shows the largest percent change in wavenumber of all Raman-active modes. However, the change is not linear. There is only a small change in the wavenumber of this mode up until a magnesium content of  $x = 0.6$ .

Three of the four IR bands can be seen in the spectra of the  $Mg_xNi_{1-x}Cr_2O_4$  series, shown in Figure 40. Preudhomme et al. report IR bands for numerous normal II-III spinels [88]. The  $\nu_3$  position of  $MgCr_2O_4$  and  $NiCr_2O_4$  agrees well with their reported values, 430 and 374  $cm^{-1}$ , respectively. Our data shows a  $MgCr_2O_4$  peak

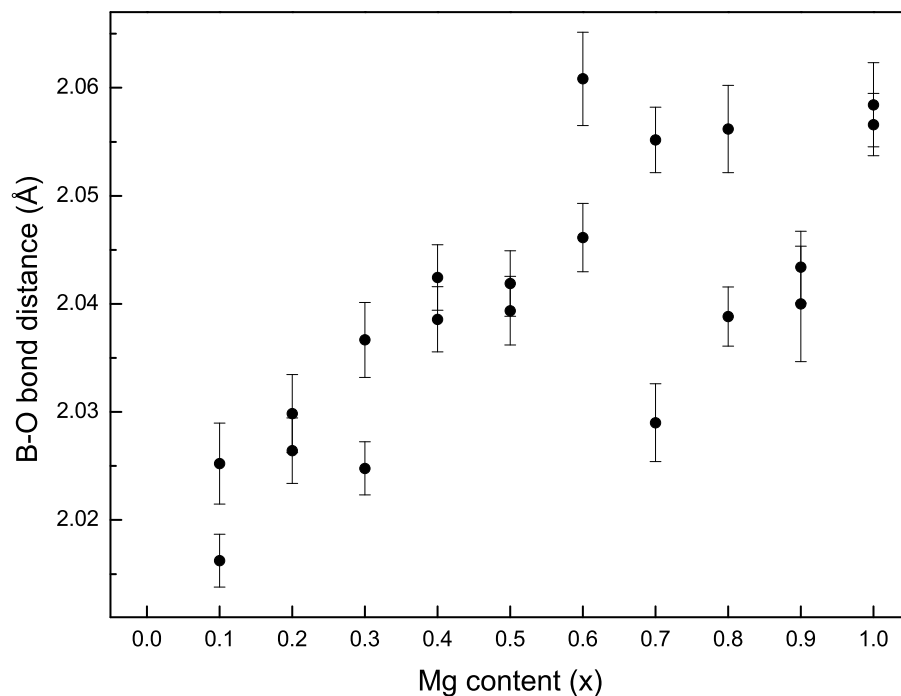


Figure 39. The B-O bond distance of  $\text{Mg}_x\text{Ni}_{1-x}\text{Cr}_2\text{O}_4$ .

at  $429\text{ cm}^{-1}$ . Because the IR data is limited to a lowest frequency of  $375\text{ cm}^{-1}$ , this peak is not completely visible. However, because the high frequency side of the peak is visible, and in view of the general trend of the peak with increasing magnesium content, this data is consistent with other work at the pure  $\text{NiCr}_2\text{O}_4$  end. Using this assumption, the frequency of the  $\nu_3$  mode increases approximately 15%. This supports the common assignment of this mode as a vibration involving the tetrahedral cation [89], though Preudhomme et al. argue that this mode also depends upon the octahedral cation [88].

The two high frequency infrared bands,  $\nu_1$  and  $\nu_2$ , are relatively broad and are difficult to fit. These two bands are consistent with the values reported by Preudhomme et al. who report  $\nu_1$  and  $\nu_2$  frequencies of 625 (647) and 512 (525) for  $\text{NiCr}_2\text{O}_4$

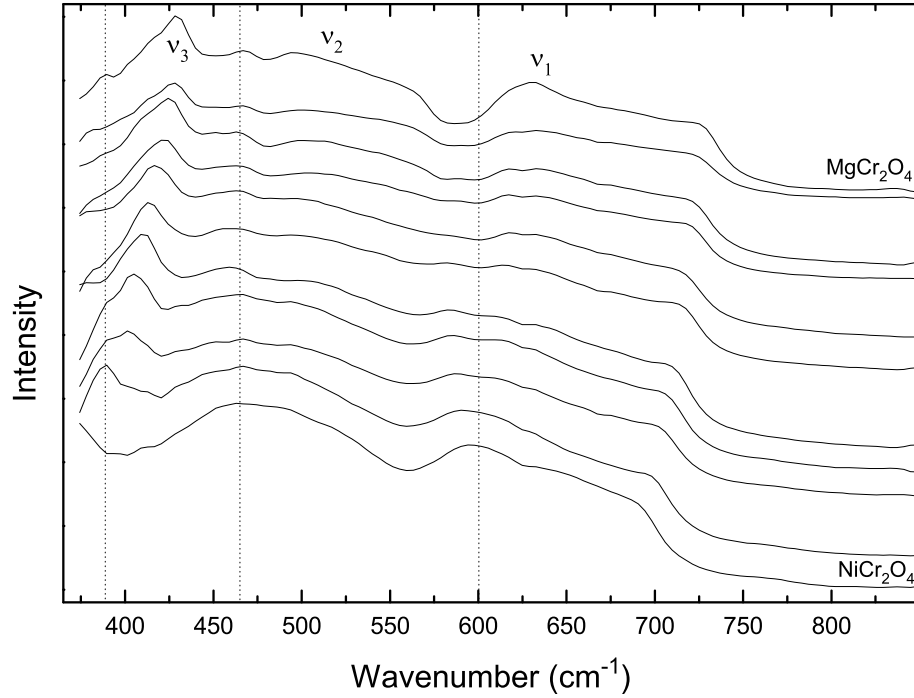


Figure 40. Infrared spectra of  $\text{Mg}_x\text{Ni}_{1-x}\text{Cr}_2\text{O}_4$ . The vertical lines are drawn as a guide to the eye.

( $\text{MgCr}_2\text{O}_4$ ), respectively [88]. There is a slight shift to higher wavenumber as the nickel is replaced with magnesium, similar to the Raman-active modes (Figure 40).



The  $\text{NiFe}_x\text{Cr}_{2-x}\text{O}_4$  system is interesting because  $\text{NiCr}_2\text{O}_4$  is a normal spinel and  $\text{NiFe}_2\text{O}_4$  is an inverse spinel [136]. Although the transition from  $\text{NiCr}_2\text{O}_4$  to  $\text{NiFe}_2\text{O}_4$  is complicated because of the cation inversion between the octahedral and tetrahedral sites, the inversion occurs during the initial substitution of iron,  $0 \leq x \leq 1$  [136–138]. Within this range, the entering trivalent iron has a lower preference for the octahedral sites than the divalent nickel, and thus the nickel occupies the octahedral sites [50]. This forces the entering iron to occupy the tetrahedral site instead. Once an iron

content of  $x = 1$  is reached, all tetrahedral sites are filled with the trivalent iron, and the substituting iron must occupy the remaining octahedral sites vacated by chromium.

This inversion during the initial iron substitution is supported by theoretical calculations and experimental data. Park et al. calculated the cation distribution of  $\text{NiFe}_x\text{Cr}_{2-x}\text{O}_4$ , and saw that at an iron content of  $x = 1$ , nearly all the nickel had been displaced from the tetrahedral sites [136]. Less than 2% of the nickel remained on the tetrahedral sites. The inversion follows linearly with the iron substitution from  $0 \leq x \leq 1$ . The same conclusion is reached by Allen et al. in their study of numerous nickel-chromium-iron spinels [137]. Rais et al. used XRD and Mössbauer spectroscopy to measure the cation inversion and show that the solid solution was completely inverse above  $x = 1$  [138]. Unfortunately, the researchers did not examine the high chromium content of  $x < 0.6$ .

Because the cation inversion occurs entirely within  $0 \leq x \leq 1$ , there are two distinct ranges of cation exchange to examine. For  $x \leq 1$ , the effect of inversion of the trivalent and divalent cations between the tetrahedral and octahedral sites can be studied. For  $x \geq 1$ , only the octahedral trivalent chromium is exchanged for the trivalent iron.

The two ranges can be observed from the behavior of the lattice parameter of the series. The lattice parameter of  $\text{NiFe}_x\text{Cr}_{2-x}\text{O}_4$  can be seen in Figure 41. This data agrees well with previous work, with the exception of an iron content of  $x = 1$  [127]. The lattice parameter decreases until an iron content of  $x = 1$  is reached, at which point it begins to increase linearly.

A temperature dependence study on cation inversion of  $\text{MgFe}_2\text{O}_4$  shows that the lattice parameter decreased as the inversion parameter increased [105]. For the  $\text{NiFe}_x\text{Cr}_{2-x}\text{O}_4$  series, the inversion parameter increases from 0 to 1 as the iron con-

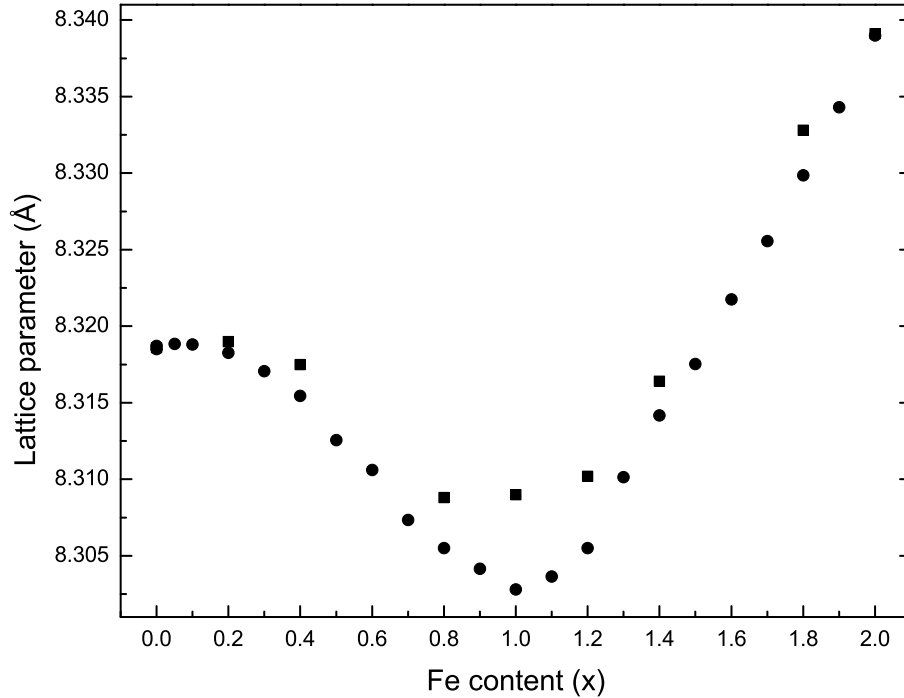


Figure 41. Lattice parameters of  $\text{NiFe}_x\text{Cr}_{2-x}\text{O}_4$ . The circles represent the data from the present work. Error bars are approximately the size of the points. Squares represent the data from Ziemniak et al. [127].

tent  $x$  increases from 0 to 1. Figure 41 also shows a decrease in the lattice parameter during the inversion of the  $\text{NiFe}_x\text{Cr}_{2-x}\text{O}_4$  spinel in the initial  $0 \leq x \leq 1$  iron content range. This could be a result of tetrahedrally coordinated  $\text{Fe}^{3+}$  having a smaller ionic radius (63 pm) than either  $\text{Ni}^{2+}$  (69 pm) or  $\text{Mg}^{2+}$  (71 pm) [111]. However, this does not explain why the lattice parameter increases above an iron content of  $x = 1$ , as the ionic radius of the substituting octahedrally coordinated  $\text{Fe}^{3+}$  is 69 pm while  $\text{Cr}^{3+}$  has an ionic radius of 76 pm [111].

The Raman spectra of the  $\text{NiFe}_x\text{Cr}_{2-x}\text{O}_4$  series can be seen in Figure 42. All five Raman-active modes are detected, although the  $F_{2g}(3)$  only becomes observable from the background above an iron content of  $x = 1$ . As iron is substituted into the system, the  $A_{1g}$ ,  $F_{2g}(2)$ , and  $F_{2g}(3)$  modes develop large shoulders. The  $F_{2g}(1)$  mode



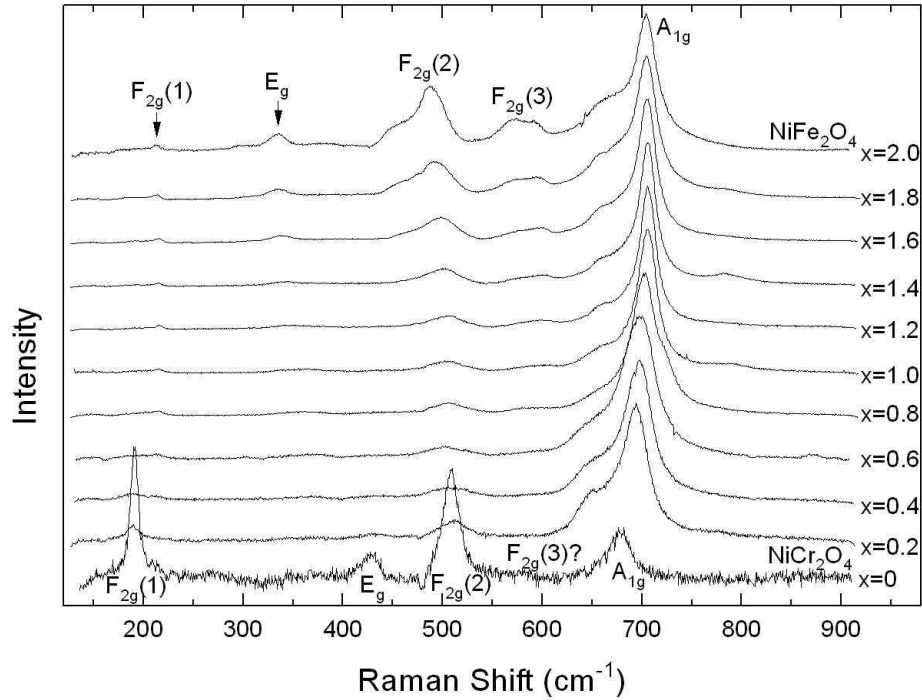


Figure 42. Raman spectra of a  $\text{NiFe}_x\text{Cr}_{2-x}\text{O}_4$ .

also develops a shoulder on the high frequency side of the mode, which becomes the more dominant feature in the spectrum as the iron content of the solid solution is increased.

The phonon frequencies of all modes and shoulders over the entire series are plotted in Figure 43. The  $A_{1g}$  is the only Raman-active mode that increases in wavenumber with increasing iron content. The wavenumbers of the  $F_{2g}(2)$  and  $E_g$  modes decrease. The  $F_{2g}(3)$  mode also decreases in wavenumber over the region of iron content that the mode is detected. The  $A_{1g}$  mode has the most dramatic change during the inversion range of  $0 \leq x \leq 1$ . Above  $x = 1$ , the position of this mode remains relatively constant. This suggests that the valency of the cation has a larger impact on the wavenumber of this mode than the small mass difference between iron and

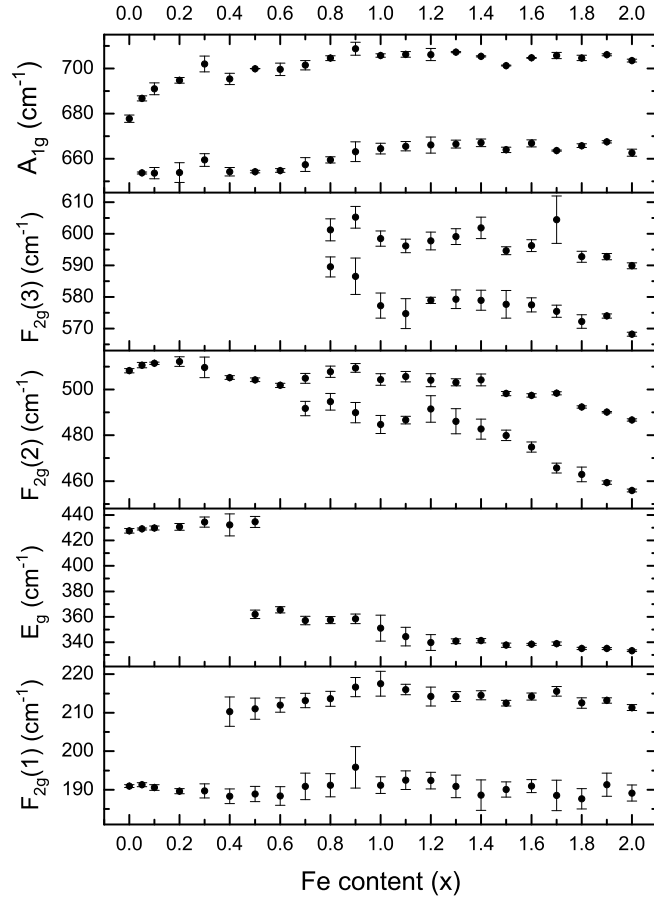


Figure 43. Raman peak positions of  $\text{NiFe}_x\text{Cr}_{2-x}\text{O}_4$ .

chromium. Above an iron content of  $x = 1$ , the  $\text{Fe}^{3+}$  is only replacing  $\text{Cr}^{3+}$  in the octahedral sites. However, there is very little change in the wavenumber of the mode during this range. This seems to contradict the view that the  $A_{1g}$  mode depends on the octahedral cation. Preudhomme et al. argue that the valency of similar cations is the most important factor for determining the vibrational frequencies [139]. This may be the main reason that the initial iron substitution exhibits a larger change in the wavenumber of this mode.

The  $A_{1g}$  mode develops a shoulder with the introduction of iron into the lattice.

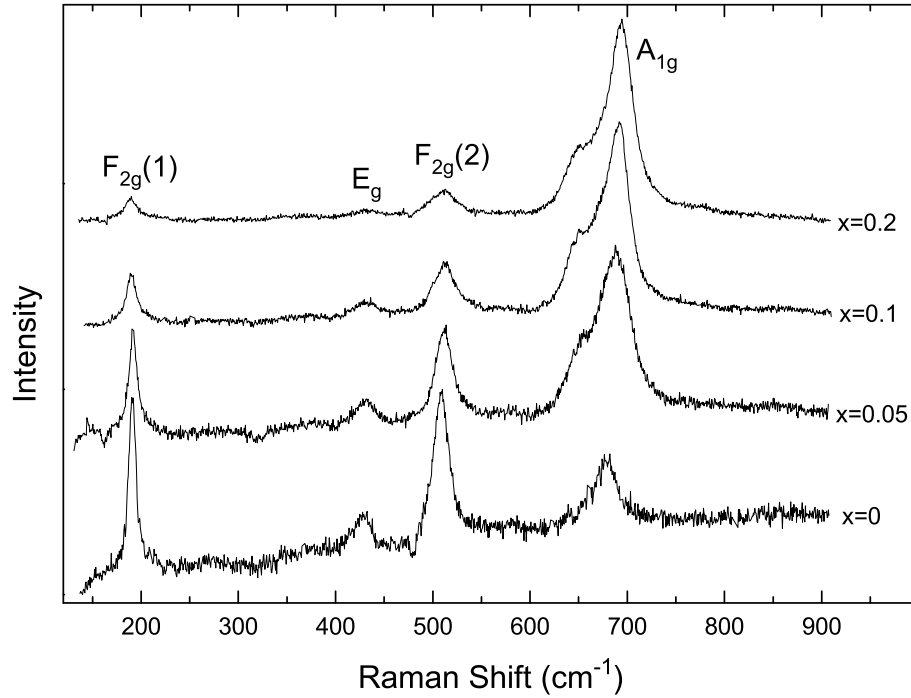


Figure 44. Raman spectra of  $\text{NiFe}_x\text{Cr}_{2-x}\text{O}_4$  having an iron content of  $0 \leq x \leq 0.2$ .

Interestingly, the intensity of the shoulder does not seem dependent upon the amount of iron in the lattice. Figure 44 shows that the shoulder appears with a significant intensity at only 5% iron substituted. As shown in Chapter 4, the lower frequency  $A_{1g}$  mode for the inverse  $\text{MgFe}_2\text{O}_4$  was consistent with it being due to a local mode of  $\text{FeO}_6$ . For the  $\text{NiFe}_x\text{Cr}_{2-x}\text{O}_4$  series, the shoulder is detected with only a modicum of iron substituted into the system, and the wavenumber of the shoulder remains relatively constant over the entire range of iron composition. This series shows that the shoulder cannot be assigned to the  $\text{FeO}_6$  unit, as no  $\text{FeO}_6$  exist in the  $0 \leq x \leq 1$  region of iron content, as iron occupies the tetrahedral site of the lattice in this region.

The  $F_{2g}(3)$  mode cannot be identified from the background at the low iron end of the series and is only detected above  $x = 0.9$ . Wang et al. report the mode at  $580 \text{ cm}^{-1}$  for pure  $\text{NiCr}_2\text{O}_4$  [47]. This mode is very broad when it becomes identifiable

and at the  $\text{NiFe}_2\text{O}_4$  end has been fitted with two peaks in the literature [64]. The wavenumbers of these modes decreases by 2 and 4% for the two different peaks as iron increases, as shown in Figure 43. Assuming  $580\text{ cm}^{-1}$  is the phonon frequency at  $x = 0$  for  $\text{NiFe}_x\text{Cr}_{2-x}\text{O}_4$ , there is the greatest change in the frequency of this mode from  $0 \leq x \leq 1$ , where it increases to  $600\text{ cm}^{-1}$ . Above  $x = 1$ , the mode decreases back down to  $590\text{ cm}^{-1}$ . This is an inverse relationship to the lattice parameter of the series, though unlike the change in lattice parameter, the greater change occurs in the  $0 \leq x \leq 1$  region.

The  $F_{2g}(2)$  mode is the only mode that has a uniform change over the entire iron content range. The wavenumber decreases linearly by approximately 4.4%. Above an iron content of  $x = 0.7$ , a lower frequency shoulder is detected. This  $F_{2g}(2)$  shoulder decreases in wavenumber by nearly 8%.

The behavior of the  $E_g$  mode shows strong evidence of two-mode behavior. The two distinct  $E_g$  modes have a large difference in the wavenumber of the vibration. This two-mode behavior occurs during the inversion of the lattice, indicating that this mode has a large dependence upon the valency of the cations occupying the tetrahedral site. From  $0 \leq x \leq 1$ , the wavenumber of the  $E_g$  mode of  $\text{NiCr}_2\text{O}_4$  varies little as chromium is substituted for iron. However, the intensity decreases, and at an iron content of  $x = 0.5$ , a lower-wavenumber mode at approximately  $362\text{ cm}^{-1}$  appears, which decreases slightly for  $x > 0.5$  until the wavenumber matches the  $E_g$  mode of  $\text{NiFe}_2\text{O}_4$ ,  $333\text{ cm}^{-1}$ . This lower-frequency  $E_g$  mode also increase in intensity as  $x$  increases. This strong dependence on the tetrahedral cation contradicts the calculations by Gupta et al., which showed a negligible dependence on the A-O force constant for the  $E_g$  mode [135].

In the iron content range of  $1 \leq x \leq 2$ , the  $E_g$  mode can be characterized by one-mode behavior and decreases in wavenumber by approximately 6%. This region

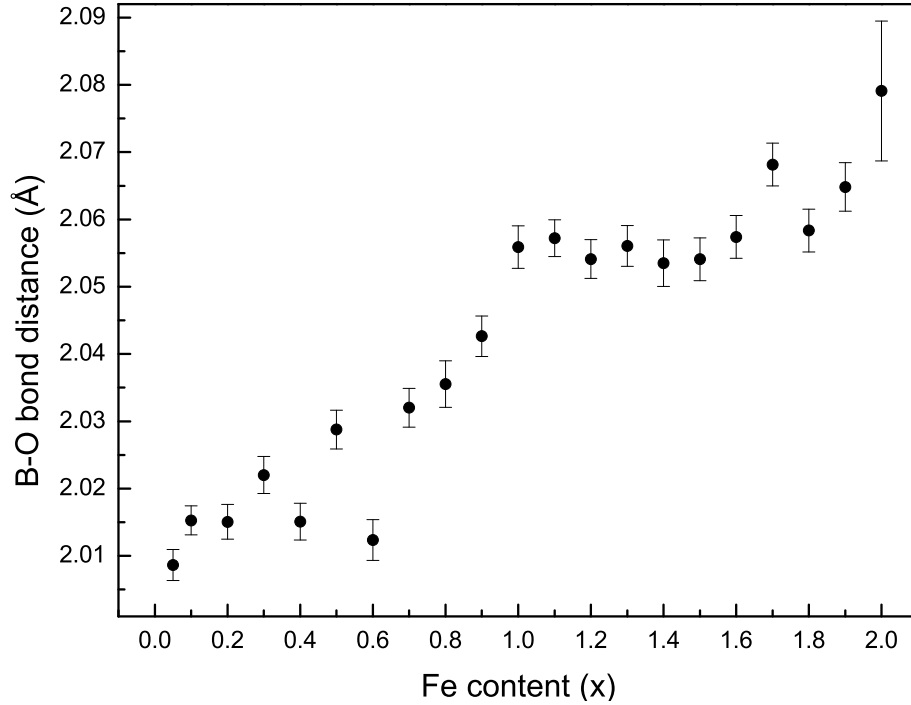


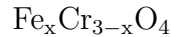
Figure 45. The B-O bond distance of  $\text{NiFe}_x\text{Cr}_{2-x}\text{O}_4$ .

only substitutes the octahedral cation, and has a slightly larger effect than the 4% change seen in this mode in the  $\text{Mg}_x\text{Ni}_{1-x}\text{Cr}_2\text{O}_4$  series, where only the tetrahedral cation was exchanged. This decrease in wavenumber is consistent with the change in mass of the octahedral unit, chromium is replaced by a slightly heavier iron cation.

As previously noted, Laguna-Bercero et al. argued that the wavenumber of the  $E_g$  mode was inversely proportional to the B-O bond distance [41]. This bond distance is shown in Figure 45 for the  $\text{NiFe}_x\text{Cr}_{2-x}\text{O}_4$  series. While the  $E_g$  mode decreases over the entire range of iron content as the B-O bond distance increases, the trends of each behave very differently. The large discontinuity at  $x = 0.4$  is not seen in the B-O bond distance. There is also an obvious discontinuity in the slope of the B-O bond distance at  $x = 1$ , which is not seen in the position of the  $E_g$  mode at the same iron

content.

The  $F_{2g}(1)$  mode develops a shoulder on the high-wavenumber side of this mode. The intensity of this shoulder increases to become the stronger of these two features. The wavenumbers of both of these modes does not vary significantly as the iron substitutes chromium. Similar to the  $A_{1g}$  mode, the inversion of the lattice seems to create the largest change in the Raman spectrum, with the development of the two distinct peaks, due to the presence of  $Fe^{3+}$  and  $Ni^{2+}$  occupying the octahedral sites of the lattice.



The  $Fe_xCr_{3-x}O_4$  system of spinels is the most relevant for application to corrosion of stainless steels, and it is surprising there exists little Raman work on the system in the literature [45]. The reduction process was not ideal for the synthesis of this series. The synthesis of samples having an iron composition below  $x = 1$  and above  $x = 2$  contained either corundum phase or metallic iron impurities. The XRD spectrum of the  $x = 2.4$  sample showed evidence of approximately 9% metallic iron along with the spinel phase. This has a small impact on the overall stoichiometry of the sample. Removing 10% of the iron from the stoichiometry of the spinel gives an iron to chromium ratio of

$$\frac{Fe}{Cr} = \frac{3 - z}{z} = \frac{2.2}{0.6}. \quad (8.1)$$

This leads to an iron content of only  $x = 3 - z = 2.36$  instead of the intended  $x = 2.40$ .

Most samples in the  $0.8 \leq x \leq 3$  iron composition range exhibited less than 3% corundum phase.  $Fe_xCr_{3-x}O_4$  samples were reduced multiple times if high amounts of corundum or metallic iron were present in the sample. The lattice parameters of samples with and without impurities were fairly consistent, though outside the uncertainties of the measurements. Full Rietveld refinement results, including the amount

of secondary phase present in each  $\text{Fe}_x\text{Cr}_{3-x}\text{O}_4$  sample, are shown in Appendix A. The largest difference in lattice parameter of samples containing impurities is the  $x = 1.0$  sample. However, the difference is still very small, with only 0.03% difference. These samples were reduced from the same as-synthesized batch, however. Some samples were synthesized twice however, and after reduction, even with negligible amounts of impurities, have a larger varying lattice parameter than samples with impurities reduced from the same as-synthesized batch. Two different samples of  $x = 1.6$  were reduced from two different as-combusted samples. The lattice parameter of these two samples is 8.3907(2) and 8.3985(1), a difference of 0.09%.

Due to the ratio of the synthesis reagents, the corundum phase likely has an iron to chromium ratio similar to the spinel phase. However, the most extreme scenario would be a corundum phase composed entirely of  $\alpha\text{-Fe}_2\text{O}_3$ . Similarly to Equation 8.1, this leads to an actual iron composition of  $x = 2.54$  instead of the intended  $x = 2.60$ .

Di Cerbo et al. report lattice parameters for the  $\alpha\text{-Fe}_2\text{O}_3\text{-Cr}_2\text{O}_3$  solid solution series, with  $a$  decreasing from 5.0343 Å for  $\alpha\text{-Fe}_2\text{O}_3$  to 4.9591 Å for  $\text{Cr}_2\text{O}_3$  [46]. The lattice parameters from the corundum phase component of the synthesized spinel powders fall within the range of lattice parameters of the  $\alpha\text{-Fe}_2\text{O}_3\text{-Cr}_2\text{O}_3$  series. Towards the iron end of the  $\text{Fe}_x\text{Cr}_{3-x}\text{O}_4$  series, the corundum phase lattice parameters approach the  $\alpha\text{-Fe}_2\text{O}_3$  values, while those closer to  $\text{FeCr}_2\text{O}_4$  exhibit lattice parameters closer to  $\text{Cr}_2\text{O}_3$ . The  $x = 2.6$  sample contained 8% corundum phase with an  $a$  lattice parameter equal to 5.0302 Å, which would place it on the iron end of the  $\alpha\text{-Fe}_2\text{O}_3\text{-Cr}_2\text{O}_3$  series. The corundum phase of the  $x = 0.8$  sample, making up 23% of the sample, had an  $a$  lattice parameter of 4.9656 Å, signifying the corundum phase contains mostly chromium.

There are numerous experimental data on the lattice parameter and cation distribution of  $\text{Fe}_x\text{Cr}_{3-x}\text{O}_4$  [23, 122, 123]. The literature examines the solid solution series

$\text{Fe}^{2+}\text{Fe}_y^{3+}\text{Cr}_{2-y}\text{O}_4$ , with  $0 \leq y \leq 2$ . Only the trivalent chromium is substituted for trivalent iron. The series transitions from the normal  $\text{FeCr}_2\text{O}_4$  spinel to the completely inverse  $\text{Fe}_3\text{O}_4$ . The site occupation of substituted iron in  $\text{Fe}_x\text{Cr}_{3-x}\text{O}_4$  is not as straightforward as the  $\text{NiFe}_x\text{Cr}_{2-x}\text{O}_4$  series. Robbins et al. define three regions for  $\text{Fe}_x\text{Cr}_{3-x}\text{O}_4$  in the iron content range of  $1 \leq x \leq 3$  [23]. In region 1,  $1 \leq x \leq 1.68$ , the substituted  $\text{Fe}^{3+}$  enters the octahedral sites of the lattice, replacing  $\text{Cr}^{3+}$ . The lattice parameter increases linearly during this region. This increase occurs despite octahedrally coordinated  $\text{Fe}^{3+}$  having a smaller ionic radius, 0.69 Å, than  $\text{Cr}^{3+}$ , 0.76 Å [111]. This increase is similar to the cation substitution in the  $\text{NiFe}_x\text{Cr}_{2-x}\text{O}_4$  series when  $\text{Fe}^{3+}$  replaces  $\text{Cr}^{3+}$  at the octahedral site. In region 2,  $1.68 \leq x \leq 2.38$ , the  $\text{Fe}^{3+}$  instead begins to occupy the tetrahedral sites, thus displacing the  $\text{Fe}^{2+}$  to octahedral sites. The lattice parameter decreases in this region. Above  $x = 2.38$ , region 3, the octahedral sites contain similar amounts of  $\text{Fe}^{2+}$  and  $\text{Fe}^{3+}$ , and the remaining  $\text{Fe}^{2+}$  cations are displaced from the tetrahedral site at  $x = 3$ . The lattice parameter again increases in this region.

Earlier work on the lattice parameter of the series by Yearian et al. and Francombe also show a similar behavior of the lattice parameter [122,123]. Unlike the three zones described by Robbins et al., these researchers divided the the final region of Robbins et al. into two regions where the lattice parameter stays relatively constant from  $x = 2.2$  to  $x = 2.6$ , and then increases above  $x = 2.6$  [23].

The lattice parameter of the  $\text{Fe}_x\text{Cr}_{3-x}\text{O}_4$  series synthesized in the present work, for an iron content of  $0.8 \leq x \leq 3.0$ , can be seen in Figure 46. This data suggests inconsistency of samples with the same iron content,  $x$ . The lattice parameter varied from sample to sample, greater than the uncertainty of each individual sample. The agreement with the literature values of the lattice parameters is fair [122, 123]. The three regions of behavior are also seen in the change in lattice parameter from the





the corundum phase in addition to the spinel phase. Stubican et al. report divalent chromium occupying the tetrahedral sites of the magnesium chromium spinel [140]. However, the synthesis occurred in a reducing environment with a temperature of 1800-2000°C. Pinch et al. reported divalent chromium on the octahedral sites of some indium substituted chalcogenide spinels [141]. From this data, it is difficult to discern whether or not  $\text{Fe}_{0.8}\text{Cr}_{2.2}\text{O}_4$  is created, with some form of chromium on the tetrahedral sites, or instead a mixture of  $\text{FeCr}_2\text{O}_4$  and  $\text{Cr}_2\text{O}_3$  is formed. In the present work, samples synthesized with iron contents less than  $x = 1$  were green after synthesis, suggesting the presence of  $\text{Cr}_2\text{O}_3$ , as powdered  $\text{Cr}_2\text{O}_3$  is green in color.

McCarty et al. studied the  $\text{Fe}_x\text{Cr}_{3-x}\text{O}_4$  series from  $\text{FeCr}_2\text{O}_4$  to  $\text{Fe}_3\text{O}_4$  with iron contents of  $x = 1, 1.4, 1.8, 2.2, 2.6, 3$  [45]. They claim that the  $A_{1g}$  mode is inversely proportional to the lattice parameter.

The Raman shifts of the  $A_{1g}$  and  $F_{2g}(3)$  modes for the  $\text{Fe}_x\text{Cr}_{3-x}\text{O}_4$  series are plotted as a function of iron content in Figure 47. Data acquired from the Alfa Aesar  $\text{Fe}_3\text{O}_4$  standard, as well as values reported by McCarty et al. are also included in the figure. The extrema of the  $A_{1g}$  mode do not completely correspond to the extrema of the lattice parameter for the same iron content. The lattice parameter has local extrema at iron contents of  $x = 1.8$  (maximum) and  $x = 2.4$  (minimum), whereas the  $A_{1g}$  mode has local extrema at iron contents of  $x = 1.6$  and  $x = 2.6$ .

$\text{Fe}_3\text{O}_4$  is an inverse spinel, and the inversion occurs in the iron content range  $1.7 \leq x \leq 2.4$ . The  $A_{1g}$  mode of the  $\text{NiFe}_x\text{Cr}_{2-x}\text{O}_4$  series develops a shoulder on the low wavenumber side after substituting just a small amount of iron for nickel. This shoulder remains over the entire compositional range of the series. A shoulder on the high wavenumber side of the  $A_{1g}$  mode was occasionally detected in the  $\text{Fe}_x\text{Cr}_{3-x}\text{O}_4$  series, but this shoulder was not consistent in all spectra acquired throughout the sample. Several spectra were acquired for all samples, with multiple spectra being

acquired at the same spot as a function of laser power. This allowed for potential heating damage to be examined, similar to what was seen in Chapter 6, with the conversion of  $\text{Fe}_3\text{O}_4$  to  $\gamma\text{-Fe}_2\text{O}_3$  and  $\alpha\text{-Fe}_2\text{O}_3$ . As laser power was increased on the sample, this shoulder would appear, if non-existent in the low power acquisition, or increase in intensity, if already detected in the low power spectrum. The shoulder remained present as the power was decreased to the original low power of 0.1 mW. This suggests that the peak is due to irreversible local heating damage of the sample.

The wavenumber of the  $A_{1g}$  mode has the largest change, though only a 1.1% decrease, in the iron content range  $1 \leq x \leq 1.6$ , which Robbins et al. report to be the range in which the substituting  $\text{Fe}^{3+}$  replaces  $\text{Cr}^{3+}$  at the octahedral site [23]. This supports the idea of the octahedral site being a significant factor in the determination of the  $A_{1g}$  phonon energy. However, this is very different from the  $\text{NiFe}_x\text{Cr}_{2-x}\text{O}_4$  series, for which the  $A_{1g}$  mode remained relatively constant above an iron content of  $x = 1$ , where  $\text{Fe}^{3+}$  also replaces  $\text{Cr}^{3+}$  at the octahedral site.

Beyond an iron content of  $x = 1.8$ , inversion begins to occur, with the trivalent iron occupying the tetrahedral sites and pushing the divalent iron to the octahedral sites. A very small shift in wavenumber occurs for the  $A_{1g}$  mode during the inversion of the lattice. Again, this is a departure from the behavior of the  $A_{1g}$  mode of the  $\text{NiFe}_x\text{Cr}_{2-x}\text{O}_4$  series, where the inversion of the lattice had a larger effect on the phonon energy.

The  $F_{2g}(3)$  mode was not consistently detected in all samples above an iron content of  $x = 1.8$ , and several of the plotted points for this mode represent only one or two detected peaks from the numerous acquired spectra. No obvious trend is observed from the behavior of this mode upon iron substitution.

The  $A_{1g}$  mode exhibits a drastic change from an iron content of  $x = 2.8$  to  $x = 3$ , decreasing from  $672 \text{ cm}^{-1}$  to  $665 \text{ cm}^{-1}$ , whereas the position of this mode from the

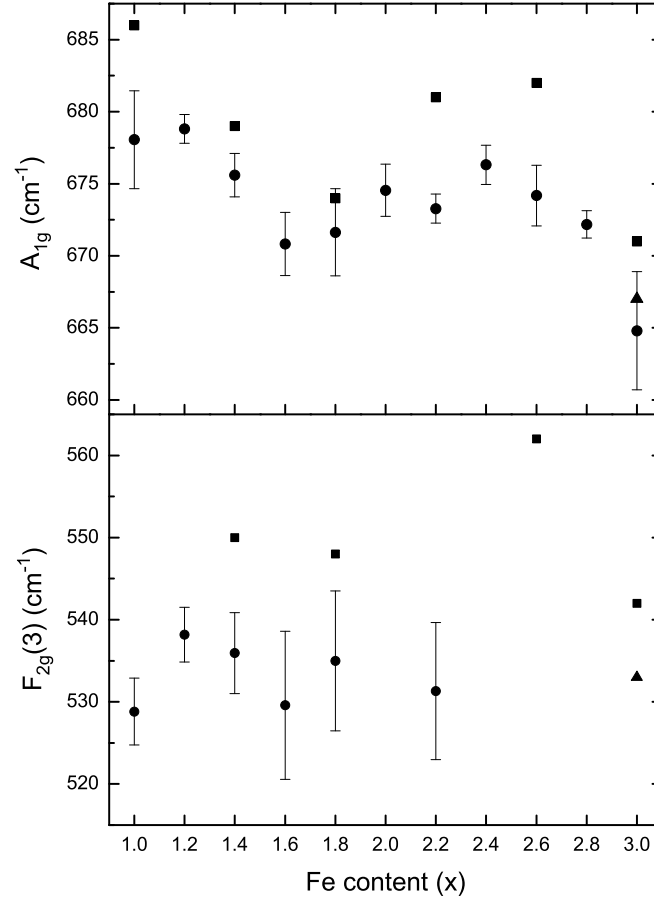


Figure 47. Raman shifts of the  $A_{1g}$  and  $F_{2g(3)}$  modes of  $Fe_xCr_{3-x}O_4$ . Data from this work is shown in solid circles, whereas data from McCarty et al. [45] is shown in solid squares. Data acquired on the Alfa Aesar  $Fe_3O_4$  standard is shown as a solid triangle at  $x = 3.0$ .

Alfa Aesar  $Fe_3O_4$  standard was  $667\text{ cm}^{-1}$ . The synthesized  $Fe_3O_4$  sample showed significant amounts of wüstite,  $FeO$ . The Raman spectrum of  $FeO$  is similar to  $Fe_3O_4$ , as shown by de Faria et al., but shifted towards a lower frequency of  $650\text{ cm}^{-1}$  [1].  $FeO$  impurities from the reduction process could explain the slightly lower wavenumber of the  $A_{1g}$  mode determined in the present work.

## Discussion on solid solutions

Examining the vibrations of the three spinel solid solutions studied here gives information regarding the cation dependency of the phonons. The data can also be used to check conclusions made by other researchers regarding the spinel phonons.

The increase in wavenumber of all the  $F_{2g}(2)$  and  $\nu_3$  vibrational modes of the  $Mg_xNi_{1-x}Cr_2O_4$  series as the lighter magnesium replaces nickel can be described sufficiently well by a simple mass on a spring inverse relationship of the vibrational frequencies on the mass of the cation. The  $A_{1g}$  mode is relatively unaffected by the large mass difference. The low-wavenumber  $E_g$  and  $F_{2g}(1)$  modes have a nonlinear response to the mass increase. This is difficult to test with the  $NiFe_xCr_{2-x}O_4$  and  $Fe_xCr_{3-x}O_4$  series as these two series substitute cations of similar mass. Inversion of the lattice also occurs for both series, which has a much larger effect on the vibrational modes.

As examined earlier in this work, high-pressure data on spinels shows that the energy of the spinel vibrational modes is inversely proportional to the lattice parameter. McCarty et al. observe this effect for the  $A_{1g}$  mode from the  $Fe_xCr_{3-x}O_4$  series [45] and the data from this work on  $Fe_xCr_{3-x}O_4$  supports that observation. From this work, the lattice parameter has extrema at an iron content of  $x = 1.8$  and  $x = 2.4$ , with the wavenumber of the  $A_{1g}$  mode having extrema at nearly the same iron content. However, data from the  $Mg_xNi_{1-x}Cr_2O_4$  and  $NiFe_xCr_{2-x}O_4$  series show that this relationship is not generally obeyed for all mixed spinel systems, or that there are other variables with larger effects on the vibrational energies. For the  $Mg_xNi_{1-x}Cr_2O_4$  series, the wavenumber of the  $A_{1g}$  mode increases slightly as the lattice parameter also increases. The increase in lattice parameter of this series is only 0.2% and the relatively large difference in mass of the Mg and Ni has the larger effect on the vibrational modes. The  $0 \leq x \leq 1$  region of the  $NiFe_xCr_{2-x}O_4$  series shows an

increase in the wavenumber of this mode as the lattice parameter decreases, but the mode remains constant above  $x = 1$ , when the lattice parameter increases linearly. The change above  $x = 1$  is larger than the decrease below  $x = 1$ .

The high-pressure data on various chromites indicate an inverse relationship of approximately 0.32 to 0.64  $\text{cm}^{-1}$  increase in wavenumber of the Raman-active modes per 0.1% decrease in unit cell volume of the chromite. Using the lattice parameters from the various series, the significance of this effect can be considered. The volume of the unit cell in the  $\text{Mg}_x\text{Ni}_{1-x}\text{Cr}_2\text{O}_4$  series changes by 0.5% as magnesium replaces nickel at the tetrahedral sites. From this contraction of the lattice, it should be expected that the Raman-active modes will increase by 1 to 4  $\text{cm}^{-1}$ , significantly less than any of the wavenumber changes in this series.

The  $\text{NiFe}_x\text{Cr}_{2-x}\text{O}_4$  series exhibits a similar change in unit cell volume in the  $0 \leq x \leq 1$  region. The volume in  $1 \leq x \leq 2$  region increases by a larger 1.3%, which corresponds to decreases in the Raman-active modes up to 8  $\text{cm}^{-1}$ . The  $E_g$ ,  $F_{2g}(2)$ , and  $F_{2g}(3)$  modes decreased in wavenumber in this range. The  $A_{1g}$  and  $F_{2g}(1)$  modes remained constant during this region.

The small changes in volumes of the solid solution series presented in this work suggest that the change in Raman-active modes due to the change in unit cell volume alone is small, and other factors are the main contributors to the large changes in Raman-active modes seen in these series.

Nakagomi et al. argued that the large mass difference between Fe and Mg and the coexistence of  $\text{FeO}_4$  and  $\text{MgO}_4$  tetrahedra leads to two distinct  $A_{1g}$  phonons of  $\text{Mg}_x\text{Fe}_{3-x}\text{O}_4$ , explaining the existence of the extra mode detected in the Raman spectrum [106]. The  $\text{Mg}_x\text{Ni}_{1-x}\text{Cr}_2\text{O}_4$  series substitutes Ni, slightly heavier than Fe, with the lighter Mg into the tetrahedral sites. All Raman-active modes of this series exhibit one-mode behavior and no extra modes are consistently found throughout the

entire range of composition. The large mass difference of Ni and Mg does not recreate the additional  $A_{1g}$  mode, as seen in the  $Mg_xFe_{3-x}O_4$  series. Only the inverse ferrites, with two different cations occupying the octahedral sites, exhibit shoulders on the  $A_{1g}$  mode. Ni and Fe are similar in mass, but Raman spectra of  $NiFe_2O_4$  exhibit an  $A_{1g}$  splitting similar to  $MgFe_2O_4$ , suggesting that the splitting is a result of two different valences occupying the octahedral site of the spinel lattice. All Raman-active modes of  $NiFe_xCr_{2-x}O_4$  exhibited shoulders.

It should also be noted that  $MgFe_2O_4$  has an inversion parameter of  $\xi = 0.90$  [105, 106], and significant amounts of  $Mg^{2+}$  would not enter the tetrahedral site in the  $Mg_xFe_{3-x}O_4$  series until  $x > 1$ . Above  $x = 1$ , the lattice would require oxygen vacancies to compensate to keep the stoichiometry correct, as Nakagomi et al. show in their study [106].

Nakagomi et al. also conclude that the larger ionic radius of tetrahedrally coordinated  $Mg^{2+}$  compared to  $Fe^{3+}$  leads to a decrease in frequency of the vibrational modes for the  $Mg_xFe_{3-x}O_4$  series [106]. Figure 9, a compilation of the Raman-active modes presented in the literature for various chromites, shows that the modes do not depend strongly upon the ionic radius of the tetrahedral cation. The  $Mg_xNi_{1-x}Cr_2O_4$  series presented here shows an opposite response of all vibrational modes, as the ionic radii of  $Ni^{2+}$  and  $Mg^{2+}$  are 0.69 and 0.71 Å, respectively [111]. All phonon frequencies increase as nickel is replaced by magnesium. For the  $NiFe_xCr_{2-x}O_4$  series in the  $1 \leq x \leq 1$  range, the Raman shifts of the  $E_g$ ,  $F_{2g}(2)$ , and  $F_{2g}(3)$  modes decrease, showing that no inverse relationship exists for the octahedral cation. The ionic radii of  $Cr^{3+}$  and  $Fe^{3+}$  is 0.76 and 0.69 Å, respectively.

From the results of the  $NiFe_xCr_{2-x}O_4$  series, changing the valency of the tetrahedral and octahedral sites has a greater effect on the  $A_{1g}$ ,  $E_g$ , and  $F_{2g}(1)$  modes. This is not surprising as phonon energies are dependent upon the force constants between

the cation and oxygens in the lattice. This force is most dramatically changed by changing the valency of the cation occupying a specific site. The wavenumber of the  $F_{2g}(2)$  mode decreases nearly linearly over the entire range of composition. The  $F_{2g}(3)$  mode was not detected from the background noise for the range of inversion. Iron is only slightly heavier than chromium, so the direct substitution should not strongly affect the frequencies for  $x > 1$ . The wavenumbers of the  $F_{2g}(1)$  and  $A_{1g}$  modes remain constant for  $x > 1$ . However, the wavenumbers of the  $E_g$ ,  $F_{2g}(2)$ , and  $F_{2g}(3)$  modes decrease in this same region. This may be a result of the increase in the lattice parameter in this region.

The  $E_g$  mode behaves differently for the  $Mg_xNi_{1-x}Cr_2O_4$  and  $NiFe_xCr_{2-x}O_4$  series. This mode, in the  $Mg_xNi_{1-x}Cr_2O_4$  series, follows one-mode behavior as it smoothly transitions from the wavenumber of  $NiCr_2O_4$  to the wavenumber of  $MgCr_2O_4$ . For  $NiFe_2O_4$ , the mode exhibits two-mode behavior, as there is a discontinuity located at an iron content of  $x = 0.5$ , and both modes coexist at this iron content. This mode shows a strong dependence on the nature of the tetrahedral cation, as the wavenumber was affected by both a change in mass of cation, and the valency of the tetrahedral cation. From the results on  $Mg_xNi_{1-x}Cr_2O_4$  and  $NiFe_xCr_{2-x}O_4$ , the  $E_g$  mode does not seem related to the B-O bond distance as argued by Laguna-Bercero et al. [41].

The question of whether the two-mode behavior of the  $E_g$  mode occurs due to the presence of distinct octahedral and tetrahedral units within the spinel lattice, or because very small crystals of one pure end-member coexisting with crystals of the other end-member is not conclusively resolved from the  $NiFe_xCr_{2-x}O_4$  data.

The additional shoulders appearing in the spectra of the  $NiFe_xCr_{2-x}O_4$  series could be due to local symmetry breaking of the system, which would not appear in x-ray diffraction patterns. The lowering of the symmetry could split the degeneracy of the  $E_g$  and  $F_{2g}$  modes, which would explain the shoulders observed on all the modes.



The  $A_{1g}$  mode is not degenerate, however polarization studies were not performed on a single crystal, and the shoulder appearing on the low-wavenumber side of the  $A_{1g}$  mode is not conclusively of the  $A_{1g}$  species.

## CHAPTER 9

### LBE-CORRODED STAINLESS STEELS

Three types of stainless steel, exposed to lead-bismuth eutectic (LBE) in a high-temperature, oxygen-controlled environment, develop corrosion layers as previously stated in Chapter 1 [58–60, 142]. Characterization of the corrosion layers developed on the stainless steel is needed, and micro-Raman is a potential tool for that purpose.

Raman spectra of the corrosion layer on 316L, D9, and HT9 stainless steel samples exposed to LBE at high temperature for 3000 hours show strong evidence for the presence of spinel oxide layers. SEM images show that a multiple layer oxide is formed [57, 60, 142]. One layer grows outwards from the original steel surface while the other grows inwards into the bulk of the steel. Raman spectra from these two layers of HT9 stainless steel, exposed to LBE for 2000 hrs at 550°C, are shown in Figure 48, and are characteristic of the Raman spectra from all LBE-exposed stainless steel samples. The largest peak of these spectra, located around 670  $\text{cm}^{-1}$ , is strong evidence of  $\text{Fe}_3\text{O}_4$  or a solid solution close to the composition of  $\text{Fe}_3\text{O}_4$ .

Work by Hosemann et al. on HT9 stainless steel shows an outer magnetite layer and an inner chromium enriched layer, which they suggest may be  $\text{Cr}_2\text{O}_3$  or  $\text{FeCr}_2\text{O}_4$  [57]. Raman spectroscopy can easily differentiate between  $\text{Cr}_2\text{O}_3$  and  $\text{FeCr}_2\text{O}_4$ . Raman spectra from this inner layer, shown in Figure 48(a), signifies that the layer is a chromium-rich spinel. The amount of chromium depends upon the exact positions of the Raman-active modes. These positions can be compared to results from the  $\text{Fe}_x\text{Cr}_{3-x}\text{O}_4$  series, and the wavenumber position of the  $A_{1g}$  mode can be used for a

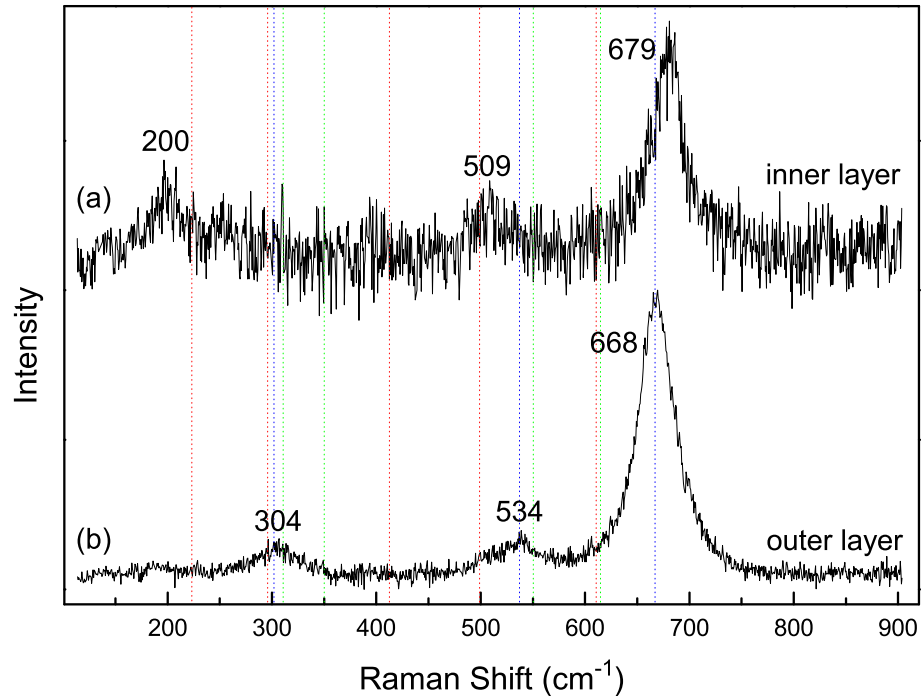


Figure 48. Raman spectra of the (a) inner and (b) outer corrosion layers of HT9 stainless steels exposed to LBE for 2000 hrs at 550°C, show characteristic peaks of the iron-chromium spinels.

identification of the oxidation layer.

Raman spectra were also collected with the 514.5 nm argon laser source to test for the presence of  $\text{Cr}_2\text{O}_3$ , as  $\text{Cr}_2\text{O}_3$  gives a much more intense signal with the 514.5 nm excitation than the 647.1 nm wavelength of the krypton laser. All acquired spectra from the corroded stainless steels show no evidence of  $\text{Cr}_2\text{O}_3$  Raman-active modes, indicating that no significant amounts of  $\text{Cr}_2\text{O}_3$  exist within the corrosion layers.

The Raman spectra of the outer corrosion layer from all three stainless steel samples are shown in Figure 49. Previous work showed that the outer corrosion layer contained only iron and oxygen [59], suggesting the presence of  $\text{Fe}_3\text{O}_4$ . The  $A_{1g}$  mode, located at approximately  $668\text{ cm}^{-1}$  for all LBE-exposed steels, agrees very

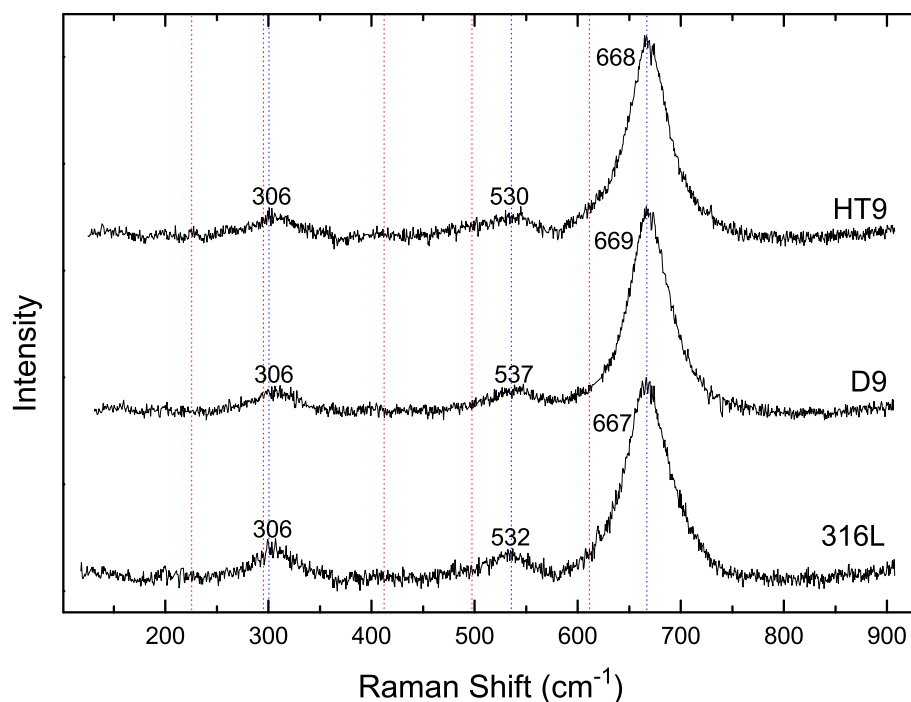


Figure 49. The outer corrosion layer of the 316L, D9, and HT9 stainless steels exposed to LBE for 3000 hrs at 550 °C share similar Raman spectra that are very representative of  $\text{Fe}_3\text{O}_4$ , indicated by the blue lines. Red lines indicate positions of the Raman-active modes of  $\alpha\text{-Fe}_2\text{O}_3$ .

well with the  $A_{1g}$  mode of  $\text{Fe}_3\text{O}_4$ . A mode located at  $306\text{ cm}^{-1}$  exists for all samples, which is also in good agreement with the  $E_g$  mode in  $\text{Fe}_3\text{O}_4$ . The  $F_{2g}(3)$  modes of the three corroded steels has a small amount of variance, with wavenumbers of  $532\text{ cm}^{-1}$  for 316L,  $530\text{ cm}^{-1}$  for HT9, and  $537\text{ cm}^{-1}$  for D9. These are all in good agreement with the same mode in magnetite located at 533 in  $\text{Fe}_3\text{O}_4$ .

The inner oxide layer presents a more complicated scenario. The inner layer has a weaker Raman signal than the outer corrosion layer, and thus the lower-wavenumber Raman-active modes are not distinguishable from the background. Spectra are similar to the outer layer, but a slight shift in the wavenumber of the main  $A_{1g}$  Raman peak, shown in Figure 50, suggests a difference from pure  $\text{Fe}_3\text{O}_4$  in the oxide layer.

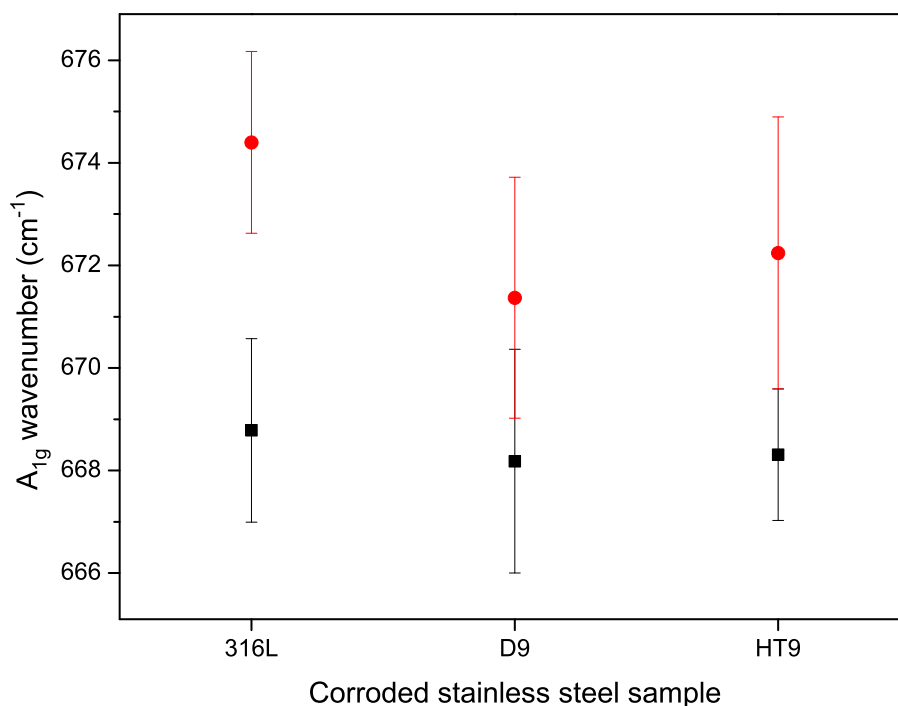


Figure 50. The wavenumber of the  $A_{1g}$  mode for the inner corrosion exhibits shifted to a slightly larger value than the povalue of the outer corrosion layer.

It is known that iron and oxygen are present in this inner oxide layer. However, other elements are also present within the inner corrosion layer. XPS and EDS show that oxidized chromium exists within the inner layer, as shown in Figure 5 [60]. A spinel belonging to the  $Fe_xCr_{3-x}O_4$  series is thus a likely candidate. As the results on  $Fe_xCr_{3-x}O_4$  have shown, substituting chromium into  $Fe_3O_4$  slightly increases the frequency of the intense  $A_{1g}$  mode.

The Raman spectrum of a spot focused on the inner corrosion layer of the the steel samples exposed to LBE at  $550^\circ\text{C}$  for 3000 hrs is shown in Figure 51. The  $A_{1g}$  mode is located at  $676\text{ cm}^{-1}$ . This peak has a shoulder located at  $631\text{ cm}^{-1}$ . This same peak is located at  $672$  and  $671\text{ cm}^{-1}$  for the D9 and HT9 stainless steels exposed to LBE at  $550^\circ\text{C}$  for 3000 hrs. Referring to Figure 47, the position of this  $A_{1g}$  mode

for 316L indicates a  $\text{Fe}_x\text{Cr}_{3-x}\text{O}_4$  spinel with  $2.0 \leq x \leq 2.4$ . The  $x = 1.4$  is also a good fit for the position of the  $A_{1g}$  mode. Data from Koury shows that there is only a slight enhancement of chromium in the inner oxide layer of the D9 sample [60]. The  $A_{1g}$  mode of the D9 and HT9 samples exposed for 3000 hrs at  $550^\circ\text{C}$  have a smaller wavenumber of 672 and  $671\text{ cm}^{-1}$ . Weight percents of the inner corrosion layer measured by Koury suggests that the iron to chromium ratio is consistent with this layer being  $\text{Fe}_{2.2}\text{Cr}_{0.8}\text{O}_4$  in the D9 sample [60]. This assumes that the layer is composed entirely of the Fe-Cr spinel, and assumes the absence of  $\text{Cr}_2\text{O}_3$ , which is not detected in any Raman spectra of the samples. Hosemann et al. also studied D9 samples exposed for 1000 and 2000 hrs, and found slightly higher chromium contents that would correspond to an iron content of approximately  $x = 2$  [142]. They also report a chromium enriched inner oxide layer for HT9 samples cut from the same tube studied in the present work [57].

Even though nickel is enhanced in the inner corrosion layer, there is no evidence of  $\text{NiCr}_2\text{O}_4$  or  $\text{NiFe}_2\text{O}_4$  modes in any of the Raman spectra from this layer of any of the steel samples. The most intense peak of  $\text{NiFe}_2\text{O}_4$  is located at  $706\text{ cm}^{-1}$ , above the position of the  $A_{1g}$  mode in all the corrosion layers. The intense peaks of  $\text{NiCr}_2\text{O}_4$  at 190 and  $508\text{ cm}^{-1}$  are also not present in any of the corrosion layers. This supports earlier conclusions from XPS studies that found only metallic nickel in the inner corrosion layer [60]. Raman spectra of the corroded D9 and HT9 steels are very similar despite the large difference in nickel compositions, 13.6% and 0.5%, respectively, indicating that no solid solution of nickel is formed.

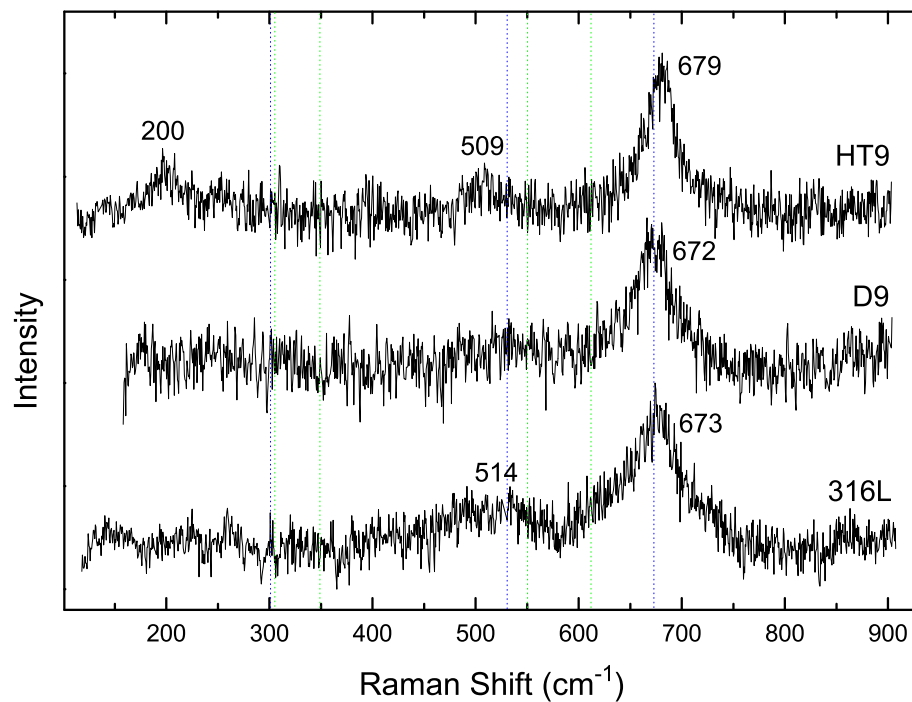


Figure 51. The Raman spectrum of the inner corrosion layer of the 316L, D9, and HT9 stainless steels exposed to LBE. The spectra are much less consistent than the outer corrosion layer. The wavenumber of the  $A_{1g}$  mode is indicative of an iron-chromium spinel from the  $Fe_xCr_{3-x}O_4$  series.

## CHAPTER 10

### CONCLUSIONS

The solid solution spinel oxides  $\text{Mg}_x\text{Ni}_{1-x}\text{Cr}_2\text{O}_4$ ,  $\text{NiFe}_x\text{Cr}_{2-x}\text{O}_4$ , and  $\text{Fe}_x\text{Cr}_{3-x}\text{O}_4$  were synthesized, and then characterized using Raman and x-ray diffraction. Vibrational data from the end members of these series agree well with the literature. Raman data of the  $\text{Mg}_x\text{Ni}_{1-x}\text{Cr}_2\text{O}_4$  and  $\text{NiFe}_x\text{Cr}_{2-x}\text{O}_4$  spinels are reported for the first time. Raman data on  $\text{Fe}_x\text{Cr}_{3-x}\text{O}_4$  agree with the literature and completes gaps in the compositional range discussed in the literature.

The vibrational modes do not necessarily change linearly as one cation is exchanged with another. Cunha et al. made this assumption for their identification of a  $\text{Ni}_x\text{Fe}_{3-x}\text{O}_4$  oxide [24]. This signifies the importance of having solid solution data before attempting to make identifications of solid solutions from vibrational data such as Raman and infrared.

A review of the literature on spinels has demonstrated that the vibrational spectra of this structure is not completely understood. The literature is inconsistent in assigning the vibrational modes to the octahedral or tetrahedral units within the lattice. Phonon dependence on the octahedral and tetrahedral bonds is complicated. However, some of the Raman-active modes of spinel display greater influence from either the tetrahedral or octahedral lattice sites.

The  $A_{1g}$  mode is mostly independent of the divalent metal occupying the tetrahedral site. All of the chromites have a similar  $A_{1g}$  wavenumber. The aluminates with the normal spinel structure,  $\text{MgAl}_2\text{O}_4$ ,  $\text{NiAl}_2\text{O}_4$ , and  $\text{CoAl}_2\text{O}_4$  also have similar  $A_{1g}$



features, located in the 755 to 772  $\text{cm}^{-1}$  range. Exchanging the octahedral cation has a much greater effect upon the wavenumber of this mode than exchanging the tetrahedral cation.

In addition, inversion of the spinel lattice, with a trivalent cation occupying the tetrahedral site, has a large impact upon the position of this mode. The two different valences of the cations occupying the octahedral site of the inverse lattice create two distinct  $A_{1g}$  modes.

The  $E_g$  mode depends upon both the octahedral and tetrahedral cations. This disagrees with the expression given by Gupta et al. that shows a negligible dependence upon the A-O force constant [135]. The mode is also seemingly independent of the B-O bond distance, as argued by Laguna-Bercero et al. [41], as the wavenumbers of this mode in the  $\text{Mg}_x\text{Ni}_{1-x}\text{Cr}_2\text{O}_4$  and  $\text{NiFe}_x\text{Cr}_{2-x}\text{O}_4$  systems increase when the B-O distances increase.

In agreement with much of the literature on spinels, the data in the present work supports the argument that the  $F_{2g}(1)$  mode is strongly dependent upon the tetrahedral cation, as both the  $\text{Mg}_x\text{Ni}_{1-x}\text{Cr}_2\text{O}_4$  and  $\text{NiFe}_x\text{Cr}_{2-x}\text{O}_4$  series show a large change in this mode upon tetrahedral cation exchange. This mode showed relatively little change in the  $\text{NiFe}_x\text{Cr}_{2-x}\text{O}_4$  series for  $x > 1$ , where only the octahedral cation was exchanged from chromium to iron.

Analysis of 316L, D9, and HT9 stainless steels corroded in a high temperature, oxygen controlled LBE environment was performed by comparing the Raman spectra from the different corrosion layers of the steel samples to the Raman spectra of the solid solution spinel series  $\text{Fe}_x\text{Cr}_{3-x}\text{O}_4$ . The frequency of the strong  $A_{1g}$  mode of the Raman spectra can be used to estimate the amount of chromium within the iron-chromium spinel. This identifies an outer corrosion layer of  $\text{Fe}_3\text{O}_4$  and an inner corrosion layer comprised of an iron chromium spinel,  $\text{Fe}_x\text{Cr}_{3-x}\text{O}_4$ , having an iron

content of approximately  $x = 2.2$ . This indicates an enhancement of the chromium over the amount of chromium within the bulk steel, which is in agreement with results from other methods by other researchers [57, 60, 142].

The application of micro-Raman spectroscopy to corrosion research is very useful. The  $3.5 \mu\text{m}$  spot size gives capability of obtaining spatial resolution to differentiate compositions of complex oxide layers. Subtle differences between Raman spectra can be exploited to gain information regarding the composition of complex corrosion layers. The most common assignment of corrosion products has been pure, one- or two-element oxides, such as  $\alpha\text{-Fe}_2\text{O}_3$ ,  $\text{Fe}_3\text{O}_4$ , or  $\text{FeCr}_2\text{O}_4$ . However, the complicated composition of different stainless steels suggests that mixed spinels could be formed. The techniques presented in the present work will lead to better identifications of such mixed oxide systems. Knowing the specific composition and structure of the corrosion layers can lead to the development of steels with more resistance to corroding conditions.

The methods and analysis detailed within this study are applicable to the numerous spinels existing with varying cations and anions occupying the tetrahedral and octahedral sites.  $\text{ZnFe}_x\text{Cr}_{2-x}\text{O}_4$  would be a good candidate to study the effect of substitution of just the octahedral cation of the spinel lattice, as both  $\text{ZnCr}_2\text{O}_4$  and  $\text{ZnFe}_2\text{O}_4$  are normal spinels.  $\text{Zn}_x\text{Ni}_{1-x}\text{Cr}_2\text{O}_4$  and  $\text{MgFe}_x\text{Cr}_{2-x}\text{O}_4$  are similar spinel series as  $\text{Mg}_x\text{Ni}_{1-x}\text{Cr}_2\text{O}_4$  and  $\text{NiFe}_x\text{Cr}_{2-x}\text{O}_4$ , respectively, and may provide similar results for the behaviors of the Raman-active vibrational modes.

Theoretical models of the spinel vibrations must be checked against experimental data. The data contained in the present study may encourage further theoretical and experimental exploration on the interesting spinel crystal system.

## APPENDIX A

### RIETVELD REFINEMENT RESULTS

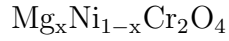
The results from the Rietveld refinements are presented in the following tables for every spinel sample synthesized in the present work. The  $R_{wp}$  and  $\chi^2$  for each sample are listed. Most samples contained small amounts of a secondary phase, which are also listed in the following tables. Corundum, space group  $R\bar{3}c$ , and metallic iron, space group  $Im\bar{3}m$ , were the most common secondary phases present with the spinel powders. The  $Fe_3O_4$  sample also contained significant amounts of  $FeO$  as an additional phase.

The tables list the lattice parameter  $a$  and oxygen parameter  $u$  for all of the synthesized samples. Table 17 also lists the lattice parameters of the tetragonal phase present in the  $NiCr_2O_4$  samples. The oxygen parameter  $u$  for the spinel phase was not refined, and instead set at  $u = 0.386$  for all  $NiCr_2O_4$  samples. Many samples of identical  $x$  were synthesized for some of the series, and are all listed in the following tables.

NiCr<sub>2</sub>O<sub>4</sub>

NiCr <sub>2</sub> O <sub>4</sub> preparation	secondary phase	Lattice parameters (Å)		R <sub>wp</sub>	χ <sup>2</sup>
		spinel	tetragonal		
as-synthesized	1.4% $R\bar{3}c$	$a = 8.3185(3)$	$a = 5.8415(8)$ $c = 8.4265(1)$	3.42	1.21
as-synthesized	4.3% $R\bar{3}c$	$a = 8.3178(3)$	$a = 5.8412(2)$ $c = 8.4275(4)$	3.43	1.24
as-synthesized	3.7% $R\bar{3}c$	$a = 8.3181(2)$	$a = 5.8443(6)$ $c = 8.4185(9)$	3.27	1.22
as-synthesized	2.2% $R\bar{3}c$	$a = 8.3187(3)$	$a = 5.8467(5)$ $c = 8.4119(8)$	3.19	1.55
as-synthesized	< 0.1% $R\bar{3}c$	$a = 8.3183(3)$	$a = 5.8388(2)$ $c = 8.4365(4)$	3.38	1.25
as-synthesized	< 0.1% $R\bar{3}c$	$a = 8.3191(2)$	$a = 5.8406(3)$ $c = 8.4329(5)$	3.37	1.25
-10°C in air	< 0.1% $R\bar{3}c$	$a = 8.3185(3)$	$a = 5.8405(2)$ $c = 8.4329(4)$	3.54	1.28
400°C in air	1.2% $R\bar{3}c$	$a = 8.3188(3)$	$a = 5.8395(3)$ $c = 8.4337(5)$	3.43	1.23
700°C in air	1.1% $R\bar{3}c$	$a = 8.3184(3)$	$a = 5.8379(2)$ $c = 8.4405(3)$	3.87	1.37
400°C in 2%H/Ar	< 0.1% $R\bar{3}c$	$a = 8.3189(3)$	$a = 5.8414(3)$ $c = 8.4290(5)$	3.66	1.33

Table 17. Rietveld refinements for as-synthesized NiCr<sub>2</sub>O<sub>4</sub> samples and NiCr<sub>2</sub>O<sub>4</sub> samples that recieved additional treatment after the combustion synthesis. The fits contain both spinel and tetragonal phases.



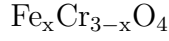
Magnesium content $x$	secondary phase	Lattice parameter $a(\text{\AA})$	oxygen parameter $u(\text{\AA})$	$R_{\text{wp}}$	$\chi^2$
0.0	See Table 17				
0.1	2.8% $R\bar{3}c$	8.3209(1)	0.3818(3)	3.34	1.20
0.1	2.1% $R\bar{3}c$	8.3209(1)	0.3830(2)	3.15	1.13
0.2	3.4% $R\bar{3}c$	8.3224(2)	0.3813(3)	3.16	1.14
0.2	1.8% $R\bar{3}c$	8.3229(1)	0.3817(2)	3.21	1.12
0.3	3.6% $R\bar{3}c$	8.3244(1)	0.3805(2)	3.07	1.09
0.3	1.6% $R\bar{3}c$	8.3246(1)	0.3820(2)	2.96	1.12
0.4	1.7% $R\bar{3}c$	8.3262(1)	0.3798(2)	3.08	1.10
0.4	1.9% $R\bar{3}c$	8.3260(1)	0.3803(2)	2.95	1.13
0.5	5.4% $R\bar{3}c$	8.3282(1)	0.3799(2)	3.05	1.11
0.5	2.3% $R\bar{3}c$	8.3276(2)	0.3802(2)	3.02	1.10
0.6	3.1% $R\bar{3}c$	8.3293(2)	0.3776(2)	3.11	1.15
0.6	3.0% $R\bar{3}c$	8.3292(1)	0.3794(2)	3.00	1.08
0.7	3.7% $R\bar{3}c$	8.3308(4)	0.3784(2)	2.94	1.14
0.7	1.8% $R\bar{3}c$	8.3306(2)	0.3816(3)	3.23	1.11
0.8	2.5% $R\bar{3}c$	8.3319(2)	0.3783(3)	2.96	1.14
0.8	1.9% $R\bar{3}c$	8.3319(1)	0.3804(2)	2.55	1.10
0.9	3.6% $R\bar{3}c$	8.3335(3)	0.3803(4)	3.46	1.14
0.9	2.2% $R\bar{3}c$	8.3333(2)	0.3799(2)	2.71	1.08
1.0	2.4% $R\bar{3}c$	8.3341(3)	0.3781(3)	2.83	1.11
1.0	2.0% $R\bar{3}c$	8.3346(2)	0.3783(2)	2.90	1.10

Table 18. Rietveld refinements for  $\text{Mg}_x\text{Ni}_{1-x}\text{Cr}_2\text{O}_4$ .

$$\text{NiFe}_x\text{Cr}_{2-x}\text{O}_4$$

Magnesium content $x$	secondary phase	Lattice parameter $a(\text{\AA})$	oxygen parameter $u(\text{\AA})$	$R_{\text{wp}}$	$\chi^2$
0.0	See Table 17				
0.05	2.2% $R\bar{3}c$	8.3188(1)	0.3839(2)	2.70	1.17
0.1	< 0.1% $R\bar{3}c$	8.3188(1)	0.3830(2)	3.29	1.16
0.2	< 0.1% $R\bar{3}c$	8.3182(1)	0.3830(2)	3.00	1.17
0.3	< 0.1% $R\bar{3}c$	8.3171(1)	0.3821(2)	3.05	1.17
0.4	1.3% $R\bar{3}c$	8.3154(1)	0.3829(2)	2.81	1.16
0.5	< 0.1% $R\bar{3}c$	8.3126(1)	0.3811(2)	3.02	1.18
0.6	< 0.1% $R\bar{3}c$	8.3106(1)	0.3831(2)	2.77	1.19
0.7	< 0.1% $R\bar{3}c$	8.3074(1)	0.3805(2)	2.81	1.17
0.8	< 0.1% $R\bar{3}c$	8.3055(2)	0.3800(2)	2.72	1.17
0.9	< 0.1% $R\bar{3}c$	8.3042(2)	0.3791(2)	2.66	1.15
1.0	< 0.1% $R\bar{3}c$	8.3028(2)	0.3774(2)	2.73	1.14
1.1	< 0.1% $R\bar{3}c$	8.3036(1)	0.3773(2)	2.50	1.11
1.2	< 0.1% $R\bar{3}c$	8.3055(1)	0.3777(2)	2.32	1.12
1.3	14.9% $R\bar{3}c$	8.3101(1)	0.3776(2)	2.58	1.13
1.4	2.0% $R\bar{3}c$	8.3142(2)	0.3781(2)	2.36	1.13
1.5	1.5% $R\bar{3}c$	8.3175(2)	0.3781(2)	2.25	1.11
1.6	1.7% $R\bar{3}c$	8.3218(2)	0.3778(2)	2.22	1.15
1.7	6.2% $R\bar{3}c$	8.3256(1)	0.3767(2)	2.15	1.10
1.8	3.1% $R\bar{3}c$	8.3299(1)	0.3779(2)	2.09	1.11
1.9	2.7% $R\bar{3}c$	8.3343(1)	0.3773(3)	2.02	1.12
2.0	8.4% $R\bar{3}c$	8.3390(3)	0.3757(7)	2.09	1.11

Table 19. Rietveld refinements for  $\text{NiFe}_x\text{Cr}_{2-x}\text{O}_4$ .



Magnesium content $x$	secondary phase	Lattice parameter $a(\text{\AA})$	oxygen parameter $u(\text{\AA})$	$R_{\text{wp}}$	$\chi^2$
0.6	62.6% $R\bar{3}c$	8.3729(4)	0.386(fixed)	3.11	1.23
0.8	22.6% $R\bar{3}c$	8.3742(4)	0.3864(4)	2.43	1.23
0.8	51.3% $R\bar{3}c$	8.3800(2)	0.3865(4)	1.62	1.19
0.8	47.9% $R\bar{3}c$	8.3789(1)	0.3849(3)	1.68	1.19
1.0	33.1% $R\bar{3}c$	8.3784(3)	0.3849(5)	2.35	1.13
1.0	33.8% $R\bar{3}c$	8.3832(5)	0.3832(5)	2.44	1.10
1.0	36.2% $R\bar{3}c$	8.3798(3)	0.3862(2)	1.54	1.16
1.0	15.0% $R\bar{3}c$	8.3772(2)	0.3844(2)	1.47	1.11
1.2	< 0.1% $R\bar{3}c$	8.3818(2)	0.3851(3)	2.30	1.08
1.4	1.3% $R\bar{3}c$	8.3904(1)	0.3839(2)	1.36	1.11
1.6	1.3% $R\bar{3}c$	8.3907(2)	0.3831(2)	1.56	1.27
1.6	2.3% $Im\bar{3}m$	8.3985(1)	0.3801(2)	1.39	1.15
1.8	3.7% $Im\bar{3}m$	8.3946(2)	0.3836(3)	2.50	1.69
1.8	5.0% $Im\bar{3}m$	8.3979(1)	0.3806(2)	1.48	1.17
2.0	3.9% $Im\bar{3}m$	8.3977(6)	0.3799(1)	1.32	1.17
2.0	5.9% $Im\bar{3}m$	8.3911(1)	0.3792(2)	1.39	1.10
2.2	< 0.1% $R\bar{3}c$	8.3919(1)	0.3791(3)	1.64	1.06
2.4	11.0% $Im\bar{3}m$	8.3864(1)	0.3787(2)	1.29	1.19
2.4	23.9% $Im\bar{3}m$	8.3860(2)	0.3795(4)	1.89	1.08
2.6	8.0% $R\bar{3}c$	8.3880(1)	0.3801(4)	1.68	1.54
2.8	26.8% $Im\bar{3}m$	8.3888(1)	0.3780(3)	1.47	1.35
2.8	33.1% $Im\bar{3}m$	8.3881(1)	0.3783(4)	1.40	1.36
2.8	12.6% $Im\bar{3}m$	8.3885(7)	0.3774(3)	1.33	1.24
3.0	22.7% $Im\bar{3}m$	8.3908(4)	0.3792(2)	2.11	1.55
	40.5% FeO				

Table 20. Rietveld refinements for  $\text{NiFe}_x\text{Cr}_{2-x}\text{O}_4$ .

## REFERENCES

- [1] D. L. A. de Faria, S. Venâncio Silva and M. T. de Oliveira. *Raman microspectroscopy of some iron oxides and oxyhydroxides*. Journal of Raman Spectroscopy **28**, 873–878 (1997).
- [2] A. Chopelas and A. M. Hofmeister. *Vibrational spectroscopy of aluminite spinels at 1 atm and of  $MgAl_2O_4$  to over 200 kbar*. Physics and Chemistry of Minerals **18**, 279–293 (1991).
- [3] Sarah P. Slotznick and Sang-Heon Shim. *In situ Raman spectroscopy measurements of  $MgAl_2O_4$  spinel up to 1400°C*. American Mineralogist **93**, 470–476 (2008).
- [4] B. Jagannadha Reddy and Ray L. Frost. *Spectroscopic characterization of chromite from the Moa-Baracoa Ophiolitic Massif, Cuba*. Spectrochimica Acta Part A **61**, 1721–1728 (2005).
- [5] A. E. Ringwood and A. Major. *The system  $Mg_2SiO_4$ - $Fe_2SiO_4$  at high pressures and temperatures*. Physics of the Earth and Planetary Interiors **3**, 89–108 (1970).
- [6] Lin-Gun Liu, T. P. Mernagh and T. Irifunes. *High pressure Raman spectra of  $\beta$ - $Mg_2SiO_4$ ,  $\gamma$ - $Mg_2SiO_4$ ,  $MgSiO_3$ -ilmeneite and  $MgSiO_3$ -preovskite*. Journal of Physics and Chemistry of Solids **55** (2), 185–193 (1994).
- [7] H. Cynn, S. K. Sharma, T. F. Cooney and M. Nicol. *High-temperature Raman investigation of order-disorder behavior in the  $MgAl_2O_4$  spinel*. Physical Review B **45** (1), 500–502 (1992).
- [8] Takamitsu Yamanaka and Motohiko Ishii. *Raman scattering and lattice vibrations of  $Ni_2SiO_4$  spinel at elevated temperature*. Physics and Chemistry of Minerals **13**, 156–160 (1986).
- [9] Alian Wang, Karla E. Kuebler, Bradley L. Jolliff and Larry A. Haskin. *Raman spectroscopy of Fe-Ti-Cr oxides, case study: Martian meteorite EETA79001*. American Mineralogist **89**, 665–680 (2004).
- [10] Yongjae Yu and Jeff S. Gee. *Spinel in Martian meteorite SaU 008: Implications for Martian magnetism*. Earth and Planetary Science Letters **232**, 287–294 (2005).



- [11] I. Ganesh, S. Bhattacharjee, B. P. Saha, R. Johnson, K. Rajeshwari, R. Sen-gupta and Y. R. Mahajan Ramana Rao, M. V. Mahajan. *An efficient  $MgAl_2O_4$  spinel additive for improved slag erosion and penetration resistance of high- $Al_2O_3$  and  $MgO-C$  refractories*. *Ceramics International* **28**, 245–253 (2002).
- [12] Yong-Yue Deng, Hou-Zhi Wang and Hui-Zhong Zhao. *Influence of chrome-bearing sols vacuum impregnation on the properties of magnesia-chrome refractory*. *Ceramics International* **34**, 573–580 (2008).
- [13] A. Ghosh, M. K. Haldar and S. K. Das. *Effect of  $MgO$  and  $ZrO_2$  additions on the properties of magnesite-chrome composite refractory*. *Ceramics International* **33**, 821–825 (2007).
- [14] C. M. Julien and M. Massot. *Lattice vibrations of materials for lithium rechargeable batteries I. lithium manganese oxide spinel*. *Materials Science and Engineering B* **97**, 217–230 (2003).
- [15] Yingjin Wei, Kyung Wan Nam, Kwang Bum Kim and Gang Chen. *Spectroscopy studies of the structural properties of Ni substituted spinel  $LiMn_2O_4$* . *Solid State Ionics* **177**, 29–35 (2006).
- [16] Kaoru Dokko, Naomi Anzue, Mohamed Mohamedi, Takashi Itoh and Isamu Uchida. *Raman spectro-electrochemistry of  $LiCo_xMn_{2-x}O_4$  thin film electrodes for 5 V lithium batteries*. *Electrochemistry Communications* **6**, 384–388 (2004).
- [17] L. Gama, E. P. Hernandez, D. R. Cornejo, A. A. Costa, S. M. Rezende, R. H. G. A. Kiminami and A. C. F. M. Costa. *Magnetic and structural properties of nanosize Ni-Zn-Cr ferrite particles synthesized by combustion reaction*. *Journal of Magnetism and Magnetic Materials* **317**, 29–33 (2007).
- [18] T. Kamiyama, K. Haneda, T. Sato, S. Ikeda and H. Asano. *Cation distribution in  $ZnFe_2O_4$  fine particles studied by neutron powder diffraction*. *Solid State Communications* **81** (7), 563–566 (1992).
- [19] Ming Chen, Jinfu Shu, Xiande Xie and Ho-kwang Mao. *Natural  $CaTi_2O_4$ -structured  $FeCr_2O_4$  polymorph in the Suizhou meteorite and its significance in mantle mineralogy*. *Geochimica et Cosmochimica Acta* **67** (20), 3937–3942 (2003).
- [20] Mona Mouallem-Bahout, Sarah Bertrand and Octavio Peña. *Synthesis and characterization of  $Zn_{1-x}Ni_xFe_2O_4$  spinels prepared by a citrate precursor*. *Journal of Solid State Chemistry* **178**, 1080–1086 (2005).
- [21] F. Bræstrup and K. K. Hansen.  *$NiCr_xFe_{2-x}O_4$  as cathode materials for electrochemical reduction of  $NO_x$* . *Journal of Solid State Electrochemistry* **14**, 157–166 (2010).

- [22] Tachiro Tsushima. *Magnetic properties of ferrite-chromite series of nickel and cobalt*. Journal of the Physical Society of Japan **18** (8), 1162–1166 (1963).
- [23] M. Robbins, G. K. Wertheim, R. C. Sherwood and D. N. E. Buchanan. *Magnetic properties and site distributions in the system  $FeCr_2O_4 - Fe_3O_4(Fe^{2+}Cr_{2-x}Fe_x^{3+}O_4)$* . Journal of Physics and Chemistry of Solids **32**, 717–729 (1971).
- [24] M. Da Cunha Belo, M. Walls, N. E. Hakiki, J. Corset, E. Picquenard, G. Sagon and D. Noël. *Composition, structure and properties of the oxide films formed on the stainless steel 316L in a primary type PWR environment*. Corrosion Science **40**, 447–463 (1998).
- [25] Derek J. Gardiner, C. John Littleton, K. Mark Thomas and Kenneth N. Stratford. *Distribution and characterization of high temperature air corrosion products on iron-chromium alloys by Raman microscopy*. Oxidation of Metals **27**, 57–72 (1987).
- [26] R Hühne, A. Kursumovic, R. I. Tomov, B. A. Glowacki, B Holzapfel and J. E. Evetts. *Texture and microstructure analysis of epitaxial oxide layers prepared on textured Ni-12wt%Cr tapes*. Journal of Physics D: Applied Physics **36**, 1053–1057 (2003).
- [27] H. Singh, D. Puri, S. Prakash and Rabindranath Maiti. *Characterization of oxide scales to evaluate high temperature oxidation behavior of Ni-20Cr coated superalloys*. Materials Science and Engineering A **464**, 110–116 (2007).
- [28] Mingcheng Sun, Xinqiang Wu, Zhaoen Zhang and En-Hou Han. *Analyses of oxide films grown on Alloy 625 in oxidizing supercritical water*. Journal of Supercritical Fluids **47**, 309–317 (2008).
- [29] W. A. England, M. J. Bennett, D. A. Greenhalgh, S. N. Jenny and C. F. Knights. *The characterization by Raman spectroscopy of oxide scales formed on a 20Cr-25Ni-Nb stabilized stainless steel*. Corrosion Science **26** (7), 537–545 (1986).
- [30] Pu Jian, Li Jian, Hua Bing and Guangyuan Xie. *Oxidation kinetics and phase evolution of a Fe-16Cr alloy in simulated SOFC cathode atmosphere*. Journal of Power Sources **158**, 354–360 (2006).
- [31] Yukio Hemmi, Nagayoshi Ichikawa, Norihisa Saito and Takahisa Masuda. *Protective oxide film on alloy X750 formed in air at 973 K*. Journal of Nuclear Science and Technology **31** (6), 552–561 (1994).
- [32] Fujio Abe, Hiroshi Araki, Heitaro Yoshida and Masatoshi Okada. *Corrosion behavior of nickel base heat resisting alloys for nuclear steelmaking system in high-temperature steam*. Transactions of the Iron and Steel Institute of Japan **25**, 424–432 (1985).

- [33] Gregory J. Van Tuyle and R. Bruce Matthews. *Addressing the nuclear waste issue*. Technical Report LALP-01-227, Los Alamos National Laboratory 2001.
- [34] E. Bright Wilson, J. C. Decius and Paul C. Cross. *Molecular Vibrations - The Theory of Infrared and Raman Vibrational Spectra*. Dover Publications, Inc., New York, NY 1980.
- [35] John R. Ferraro and Kazuo Nakamoto. *Introductory Raman Spectroscopy*. Academic Press, San Diego, CA 1994.
- [36] S. Califano. *Vibrational States*. John Wiley & Sons, New York, NY 1976.
- [37] S. Bhagavantam and T. Venkatarayudu. *Raman effect in relation to crystal structure*. Proceedings - Indian Academy of Science, Section A **9**, 224–258 (1939).
- [38] W. B. White and B. A. DeAngelis. *Interpretation of the vibrational spectra of spinels*. Spectrochimica Acta **23A**, 985–995 (1967).
- [39] Michael P. Marder. *Condensed Matter Physics*. John Wiley & Sons, Inc., New York, NY 2000.
- [40] Nguyen Van Minh and In-Sang Yang. *A Raman study of cation-disorder transition temperature of natural  $MgAl_2O_4$  spinel*. Vibrational Spectroscopy **35**, 93–96 (2004).
- [41] M. A. Laguna-Bercero, M. L. Sanjuán and R. I. Merino. *Raman spectroscopic study of cation disorder in poly- and single crystals of the nickel aluminate spinel*. Journal of Physics: Condensed Matter **19**, 1–10 (2007).
- [42] Roderick J. Hill, James R. Craig and G. V. Gibbs. *Systematics of the spinel structure type*. Physics and Chemistry of Minerals **4**, 317–339 (1979).
- [43] Sang-Heon Shim and Thomas S. Duffy. *Raman spectroscopy of  $Fe_2O_3$  to 62 GPa*. American Mineralogist **87**, 318–326 (2002).
- [44] J. Mougín, T. Le Bihan and G. Lucazeau. *High-pressure study of  $Cr_2O_3$  obtained by high-temperature oxidation by x-ray diffraction and Raman spectroscopy*. Journal of Physics and Chemistry of Solids **62**, 553–563 (2001).
- [45] K.F. McCarty and D.R. Boehme. *A Raman study of the systems  $Fe_{3-x}Cr_xO_4$  and  $Fe_{2-x}Cr_xO_3$* . Journal of Solid State Chemistry **79**, 19–27 (1989).
- [46] R. K. Di Cerbo and A. U. Seybolt. *Lattice parameters of the  $\alpha$ - $Fe_2O_3$ - $Cr_2O_3$  solid solution*. Journal of the American Ceramic Society **42** (9), 430–431 (1959).

- [47] Zhongwu Wang, S. K. Saxena, Peter Lazor and H.S.C. O’Neil. *An in situ Raman spectroscopy study of the pressure induced dissociation of spinel  $NiCr_2O_4$* . Journal of Physics and Chemistry of Solids **64**, 425–431 (2003).
- [48] Z. Wang, H. S. C. O’Neill, P. Lazor and S. K. Saxena. *High pressure Raman spectroscopic study of spinel  $MgCr_2O_4$* . Journal of Physics and Chemistry of Solids **63**, 2057–2061 (2002).
- [49] H. Perron, T. Mellier, C. Domain, J. Roques, E. Simoni, R. Drot and H. Catalette. *Structural investigation and electronic properties of the nickel ferrite  $NiFe_2O_4$ : a periodic density functional theory approach*. Journal of Physics: Condensed Matter **19**, 346219 (2007).
- [50] J. D. Dunitz and L. E. Orgel. *Electronic properties of transition-metal oxides - II cation distribution amongst octahedral and tetrahedral sites*. Journal of Physics and Chemistry of Solids **3**, 318–323 (1957).
- [51] Olga N. Shebanova and Peter Lazor. *Raman spectroscopy study of magnetite ( $FeFe_2O_4$ ): A new assignment for the vibration spectrum*. Journal of Solid State Chemistry **174**, 424–430 (2003).
- [52] D. Lenaz, H. Skogby, F. Princivalle and U. Hålenius. *Structural changes and valence states in the  $MgCr_2O_4$ - $FeCr_2O_4$  solid solution series*. Physics and Chemistry of Minerals **31**, 633–642 (2004).
- [53] H. A. Jahn and E. Teller. *Stability of polyatomic molecules in degenerate electronic states. I. orbital degeneracy*. Proceedings of the Royal Society of London. Series A, Mathematical and Physical Sciences **161** (905), 220–235 (1937).
- [54] J. D. Dunitz and L. E. Orgel. *Electronic properties of transition-metal oxides - I distortions from cubic symmetry*. Journal of Physics and Chemistry of Solids **3**, 20–29 (1957).
- [55] H. M. Rietveld. *A profile refinement method for nuclear and magnetic structures*. Journal of Applied Crystallography **2**, 65–71 (1969).
- [56] C.V. Raman and K.S. Krishnan. *A new type of secondary radiation*. Nature **121**, 501 (1928).
- [57] P. Hosemann, M. E. Hawley, D. Koury, J. Welch, A. L. Johnson, G. Mori, N. Li and S. A. Maloy. *Nanoscale characterization of HT-9 exposed to lead bismuth eutectic at 550°C for 3000 h*. Journal of Nuclear Materials **381**, 211–215 (2008).
- [58] Allen L. Johnson, Eric P. Loewen, Thao T. Ho, Dan Koury, Brian Hosterman, Umar Yuonas, Jenny Welch and John W. Farley. *Spectroscopy and microscopic study of the corrosion of iron-silicon steel by lead-bismuth eutectic (LBE) at elevated temperatures*. Journal of Nuclear Materials **350**, 221–231 (2006).

- [59] Allen L. Johnson, Denise Parsons, Julie Manzerova, Dale L. Perry, Dan Koury, Brian Hosterman and John W. Farley. *Spectroscopic and microscopic investigation of the corrosion of 316/316L stainless steel by lead-bismuth eutectic (LBE) at elevated temperatures: Importance of surface preparation*. Journal of Nuclear Materials **328**, 88–94 (2004).
- [60] Daniel Koury. *Characterization of the Mechanism of Bi-Layer Oxide Growth on Austenitic Stainless Steels 316L and D9 in Oxygen-Controlled Lead-Bismuth Eutectic (LBE)*. PhD thesis University of Nevada, Las Vegas December 2008.
- [61] S. C. Tjong. *Laser Raman spectroscopy studies of the surface oxides formed on iron chromium alloys at elevated temperatures*. Materials Research Bulletin **18**, 157–165 (1983).
- [62] Ph. Colomban, S. Cherifi and G. Despert. *Raman identification of corrosion products on automotive galvanized steel sheets*. Journal of Raman Spectroscopy **39**, 881–886 (2008).
- [63] Delphine Neff, Solenn Reguer, Ludovic Bellot-Gurlet, Philippe Dillmann and Régis Bertholon. *Structural characterization of corrosion products on archaeological iron: an integrated analytical approach to establish corrosion forms*. Journal of Raman Spectroscopy **35**, 739–745 (2004).
- [64] Ji Hyun Kim and Il Soon Hwang. *Development of an in situ Raman spectroscopy system for surface oxide films on metals and alloys in high temperature water*. Nuclear Engineering and Design **235**, 1029–1040 (2005).
- [65] R. L. Farrow, R. E. Benner, A. S. Nagelberg and P. L. Mattern. *Characterization of surface oxides by Raman spectroscopy*. Thin Solid Films **73**, 353–358 (1980).
- [66] D. Rensch, B. Veal, K. Natesan and M. Grimsditch. *Transient oxidation in Fe-Cr-Ni alloys: A Raman-scattering study*. Oxidation of Metals **46**, 365–381 (1996).
- [67] N. Boucherit, A. Hugot-Le Goff and S. Joiret. *Raman studies of corrosion films grown on Fe and Fe-6Mo in pitting conditions*. Corrosion Science **32** (5/6), 497–507 (1991).
- [68] Xuejin Zheng and Robert A. Rapp. *Chloridation-oxidation of Fe-Cr and Ni-Cr alloys at 800°C*. Oxidation of Metals **48** (5/6), 527–551 (1997).
- [69] P. R. Wilson and Z. Chen. *The effect of manganese and chromium on surface oxidation products formed during batch annealing of low carbon steel strip*. Corrosion Science **49**, 1305–1320 (2007).
- [70] H. A. Lauwers and M. A. Herman. *Force field of some AB<sub>2</sub>C<sub>4</sub> spinel compounds*. Journal of Physics and Chemistry of Solids **41**, 223–230 (1980).

- [71] M. E. Striefler and G. R. Barsch. *Lattice dynamics at zero wave vector and elastic constants of spinel in the rigid ion approximation*. Journal of Physics and Chemistry of Solids **33**, 2229–2250 (1972).
- [72] A. K. Kushwaha. *Lattice dynamics at zone-center of sulphide and selenide spinels*. Communications in Theoretical Physics **50**, 1422–1426 (2008).
- [73] H. C. Gupta, Geeta Sood, Arvind Parashar and B. B. Tripathi. *Long wavelength optical lattice vibrations in mixed chalcogenide spinels  $Zn_{1-x}Cd_xS_4$  and  $CdCr_2(S_{1-x}Se_x)_4$* . Journal of Physics and Chemistry of Solids **50** (9), 925–929 (1989).
- [74] H. C. Gupta, M. M. Sinha, K. B. Chand and Balram. *Zone-centre phonon frequency calculation of the spinel structure compounds  $MnCr_2O_4$  and  $FeCr_2S_4$* . Physica status solidi B **169**, K65–K68 (1992).
- [75] H. C. Gupta, Arvind Parashar, V. B. Gupta and B. B. Tripathi. *Study of interaction forces and phonons in some spinels and mixed systems*. Physica B **167**, 175–181 (1990).
- [76] Yongjun Chen, Zongwen Liu, Simon P. Ringer, Zhangfa Tong, Xuemin Cui and Ying Chen. *Selective oxidation synthesis of  $MnCr_2O_4$  spinel nanowires from commercial stainless steel foil*. Crystal Growth and Design **7** (11), 2279–2281 (2007).
- [77] M. M. Sinha. *Vibrational analysis of optical phonons in mixed chromite spinels*. Nuclear Instruments and Methods in Physics Research B: Beam Interactions with Materials and Atoms **153**, 183–185 (1999).
- [78] R. D. Waldron. *Infrared spectra of ferrites*. Physical Review **99** (6), 1727–1735 (1955).
- [79] J. Larry Verble. *Temperature-dependent light-scattering studies of the Verwey transition and electronic disorder in magnetite*. Physical Review B **9** (12), 5236–5248 (1974).
- [80] H. C. Gupta, M. M. Sinha, Balram and B. B. Tripathi. *A study of the interatomic interaction in oxide spinel  $MnCr_2O_4$* . Physica B **192**, 343–344 (1993).
- [81] A. K. Kushwaha. *Study of interatomic interactions in chromite spinel  $CoCr_2O_4$* . Chinese Journal of Physics **47** (3), 355–360 (2009).
- [82] A. K. Kushwaha and S. S. Kushwaha. *Zone-centre phonon frequencies of oxide spinels*. Chinese Journal of Physics **45** (3), 363–373 (2007).
- [83] M. M. Sinha and Jin-Seung Kim. *Analysis of vibrational modes and phonon density of states of aluminate spinels*. Journal of the Korean Physical Society **43** (2), 237–241 (2003).

- [84] Kunio Wakamura, Hidetoshi Iwatani and Kenichi Takarabe. *Vibrational properties of one- and two-mode behavior in spinel type mixed systems  $Zn_{1-x}Cd_xCr_2S_4$* . Journal of Physics and Chemistry of Solids **48** (9), 857–867 (1987).
- [85] C. Pernechele, M. Solzi, M. Ghidini, E. Arisi, I. Bergenti and V. Dediu. *Magnetic behaviour of hybrid magnetite/organic semiconductor bilayers*. Journal of Physics D: Applied Physics **41**, 134013 (2008).
- [86] P. Brüesch and F. D’Ambrogio. *Lattice dynamics and magnetic ordering in the chalcogenide spinels  $CdCr_2S_4$  and  $CdCr_2Se_4$* . Physica Status Solidi B **50**, 513–526 (1972).
- [87] M. P. O’Horo, A. L. Frisillo and W. B. White. *Lattice vibrations of  $MgAl_2O_4$  spinel*. Journal of Physics and Chemistry of Solids **34**, 23–28 (1973).
- [88] J. Preudhomme and P. Tarte. *Infrared studies of spinels III: The normal II-III spinels*. Spectrochimica Acta **27A**, 1817–1835 (1971).
- [89] Z. V. Marinković Stanojević, N. Romčević and B. Stojanović. *Spectroscopic study of spinel  $ZnCr_2O_4$  obtained from mechanically activated  $ZnO-Cr_2O_3$  mixtures*. Journal of the European Ceramic Society **27**, 903–907 (2007).
- [90] Seong-Ju Hwang, Dae-Hoon Park, Jin-Ho Choy and Guy Campet. *Effect of chromium substitution on the lattice vibration of spinel lithium manganate: a new interpretation of the Raman spectrum of  $LiMn_2O_4$* . Journal of Physical Chemistry B **108**, 12713–12717 (2004).
- [91] J. Preudhomme and P. Tarte. *Infrared studies of spinels II: The experimental bases for solving the assignment problem*. Spectrochimica Acta **27A**, 845–851 (1971).
- [92] I. F. Chang and S. S. Mitra. *Long wavelength optical phonons in mixed crystals*. Advances in Physics **20**, 359–404 (1971).
- [93] C. Kant, J. Deisenhofer, T. Rudolf, F. Mayr, F. Schrettle, A. Loidl, V. Cnezdilov, D. Wulferding, P. Lemmens and V. Tsurkan. *Optical phonons, spin correlations, and spin-phonon coupling in the frustrated pyrochlore magnets  $CdCr_2O_4$  and  $ZnCr_2O_4$* . Physical Review B **80**, 214417 (2009).
- [94] A. A. Khasin, T. M. Yur’eva, L. M. Plyasova, G. N. Kustova, H. Jovic, A. Ivanov, Y. A. Chesalov, V. I. Zaikovskii, A. V. Khasin, L. P. Davydova and V. N. Parmon. *Mechanistic features of reduction of copper chromite and state of absorbed hydrogen in the structure of reduced copper chromite*. Russian Journal of General Chemistry **78** (11), 2203–2213 (2008).
- [95] Zhongwu Wang, Peter Lazor, S. K. Saxena and Gilberto Artioli. *High pressure Raman spectroscopic study of spinel  $ZnCr_2O_4$* . Journal of Solid State Chemistry **165**, 165–170 (2002).

- [96] P. Chandramohan, M. P. Srinivasan, S. Velmurugan and S. V. Narasimhan. *Cation distribution and particle size effect on Raman spectrum of  $\text{CoFe}_2\text{O}_4$* . Journal of Solid State Chemistry **184**, 89–96 (2011).
- [97] Zhongwu Wang, P. Lazor, S. K. Saxena and Hugh S. C. O’Neil. *High pressure Raman spectroscopy of ferrite  $\text{MgFe}_2\text{O}_4$* . Materials Research Bulletin **37**, 1589–1602 (2002).
- [98] Zhongwu Wang, David Schiferl, Yusheng Zhao and O’Neill H. S. C. *High pressure Raman spectroscopy of spinel-type ferrite  $\text{ZnFe}_2\text{O}_4$* . Journal of Physics and Chemistry of Solids **64**, 2517–2523 (2003).
- [99] Hiroshi Shirai, Yoshiyuki Morioka and Ichiro Nakagawa. *Infrared and Raman spectra and lattice vibrations of some oxide spinels*. Journal of the Physical Society of Japan **51** (2), 592–597 (1982).
- [100] S. López-Moreno, P. Rodríguez-Hernández, A. Muñoz, A. H. Romero, F. J. Manjón, D. Errandonea, E. Rusu and V. V. Ursaki. *Lattice dynamics of  $\text{ZnAl}_2\text{O}_4$  and  $\text{ZnGa}_2\text{O}_4$  under high pressure*. Annalen der Physik (Berlin) **523** (1-2), 157–167 (2011).
- [101] V. G. Hadjiev, M. N. Iliev and I. V. Vergilov. *The Raman spectra of  $\text{Co}_3\text{O}_4$* . Journal of Physics C: Solid State Physics **21**, L199–L201 (1988).
- [102] G. G. P. Van Gorkom, J. H. Haanstra and H. v. d. Boom. *Infrared and raman spectra of the spinel  $\text{ZnGa}_2\text{O}_4$* . Journal of Raman Spectroscopy **1**, 513–519 (1973).
- [103] Roger G. Burns. *Crystal field effects in chromium and its partitioning in the mantle*. Geochimica et Cosmochimica Acta **39**, 857–864 (1975).
- [104] Sonal Singhal and Kailash Chandra. *Cation distribution and magnetic properties in chromium-substituted nickel ferrites prepared using aerosol route*. Journal of Solid State Chemistry **180**, 296–300 (2007).
- [105] H. S. C. O’Neill, H. Annerstein and D. Virgo. *The temperature dependence of the cation distribution in magnesioferrite ( $\text{MgFe}_2\text{O}_4$ ) from powder XRD structural refinements and Mössbauer spectroscopy*. American Mineralogist **77**, 725–740 (1992).
- [106] F. Nakagomi, S. W. da Silva, V. K. Garg, A. C. Oliveira, P. C. Morais and A. Franco Jr. *Influence of the Mg-content on the cation distribution in cubic  $\text{Mg}_x\text{Fe}_{3-x}\text{O}_4$  nanoparticles*. Journal of Solid State Chemistry **182**, 2423–2429 (2009).
- [107] J. Z. Jiang, P. Wynn, S. Mørup, T. Okada and F. J. Berry. *Magnetic structure evolution in mechanically milled nanostructured  $\text{ZnFe}_2\text{O}_4$  particles*. Nanostructured Materials **12**, 737–740 (1999).



- [108] Lorenzo Malavasi, Pietro Galinetto, Maria C. Mozzati, Carlo B. Azzoni and Giorgio Flor. *Raman spectroscopy of  $AMn_2O_4$  ( $A = Mn, Mg$  and  $Zn$ ) spinels*. Physical Chemistry Chemical Physics **4**, 3876–3880 (2002).
- [109] P. R. Graves, C. Johnston and J. J. Campaniello. *Raman scattering in spinel structured ferrites*. Materials Research Bulletin **23**, 1651–1660 (1988).
- [110] Lev Gasparov, Andrew Rush, Thomas Pekarek, Nirmal Patel and Helmuth Berger. *Raman studies of doped magnetite above and below the Verwey transition*. Journal of Applied Physics **105**, 07E109 (2009).
- [111] R. D. Shannon. *Revised effective ionic radii and systematic studies of interatomic distances in halides and chalcogenides*. Acta Crystallographica Section A **32** (5), 751–767 (1976).
- [112] A. Sawaoka, S. Saito, K. Inoue and Asada T. *Effect of high pressure on the lattice constants of chromites having the spinel structure*. Materials Research Bulletin **6**, 97–102 (1971).
- [113] D. Basak and J. Ghose. *Infrared studies on some substituted copper chromite spinels*. Spectrochimica Acta **50A** (4), 713–718 (1994).
- [114] J. Himmrich and H. D. Lutz. *Normal coordinate analyses and lattice dynamical calculations of spinel-type  $ZnCr_2O_4$* . Solid State Communications **79** (5), 447–452 (1991).
- [115] Naoufal Bahlawane, Patrick Herve Tchoua Ngamou, Vincent Vannier, Tilman Kottke, Joachim Heberle and Katharina Kohse-Höinghaus. *Tailoring the properties and the reactivity of the spinel cobalt oxide*. Physical Chemistry Chemical Physics **11**, 9224–9232 (2009).
- [116] J. M. Malézieux, J. Barbillat, B. Cervelle, J. P. Coutures, M. Couzi and B. Piriou. *Étude de spinelles de synthèse de la série  $MgCr_xAl_{2-x}O_4$  et de chromites naturelles par microsonde Raman-laser*. Tshermaks Mineralogische und Petrographische Mitteilungen **32**, 171–185 (1983).
- [117] C. David, B. K. Panigrahi, S. Balaji, A. K. Balamurugan, K. G. M. Nair, G. Amarendra, C. S. Sundar and Baldev Raj. *A study of the effect of titanium on the void swelling behavior of D9 steels by ion beam simulation*. Journal of Nuclear Materials **383**, 132–136 (2008).
- [118] S. Sundar Manoharan and Kashinath C. Patil. *Combustion synthesis of metal chromite powders*. Journal of the American Ceramic Society **75**, 1012–1015 (1992).
- [119] Adolfo Franco Júnior, Emília Celma de Oliveira Lima, Miguel A. Novak and Paulo R. Wells Jr. *Synthesis of nanoparticles of  $Co_xFe_{(3-x)}O_4$  by combustion*

- reaction method*. Journal of Magnetism and Magnetic Materials **308**, 198–202 (2007).
- [120] M. A. F. Ramalho, L. Gama, S. G. Antonio, C. O. Paiva-Santos, E. J. Miola, R. H. G. A. Kiminami and A. C. F. M. Costa. *X-Ray diffraction and Mössbauer spectra of nickel ferrite prepared by combustion reaction*. Journal of Materials Science **42**, 3603–3606 (2007).
- [121] Olga N. Shebanova and Peter Lazor. *Raman study of magnetite ( $Fe_3O_4$ ): Laser-induced thermal effects and oxidation*. Journal of Raman Spectroscopy **34**, 845–852 (2003).
- [122] H. J. Yearian, J. M. Kortright and R. H. Langenheim. *Lattice parameters of the  $FeFe_{2-x}Cr_xO_4$  spinel system*. Journal of Chemical Physics **22** (7), 1196–1198 (1954).
- [123] M. H. Francombe. *Lattice changes in spinel-type iron chromites*. Journal of Physics and Chemistry of Solids **3**, 37–43 (1957).
- [124] H. J. Levinstein, M. Robbins and C. Capiro. *A crystallographic study of the system  $FeCr_2O_4$ - $Fe_3O_4$  ( $Fe^{2+}Fe_x^{3+}Cr_{2-x}O_4$ )*. Materials Research Bulletin **7**, 27–34 (1972).
- [125] David R. Black, Donald Windover, Albert Henins, David Gil, James Filliben and James P. Cline. *Certification of NIST standard reference material 640d*. Powder Diffraction **25** (2), 187–190 (2010).
- [126] H. St. C. O’Neill and W. A. Dollase. *Crystal structures and cation distributions in simple spinels from powder XRD structural refinements:  $MgCr_2O_4$ ,  $ZnCr_2O_4$ ,  $Fe_3O_4$  and the temperature dependence of the cation distribution in  $ZnAl_2O_4$* . Physics and Chemistry of Minerals **20**, 541–555 (1994).
- [127] S. E. Ziemniak, A. R. Gaddipati and P. C. Sander. *Immiscibility in the  $NiFe_2O_4$ - $NiCr_2O_4$  spinel binary*. Journal of Physics and Chemistry of Solids **66**, 1112–1121 (2005).
- [128] J. E. Sansonetti, W. C. Martin and S. L. Young. *Handbook of basic atomic spectroscopic data*. <http://physics.nist.gov/PhysRefData/Handbook/index.html> (version 1.1.2). National Institute of Standards and Technology, Gaithersburg, MD (2005).
- [129] Aaron M. Jubb and Heather C. Allen. *Vibrational spectroscopy characterization of hematite, maghemite, and magnetite thin films produced by vapor deposition*. Applied Materials and Interfaces **2** (10), 2804–2812 (2010).
- [130] Ricardo Grau-Crespo, Asmaa Y Al-Baitai, Iman Saadoune and Nora H. De Leeuw. *Vacancy ordering and electronic structure of  $\gamma$ - $Fe_2O_3$  (maghemite)*:

- a theoretical investigation.* Journal of Physics: Condensed Matter **22**, 255401 (2010).
- [131] Reto Strobel and Sotiris E. Pratsinis. *Direct synthesis of maghemite, magnetite and wustite nanoparticles by flame spray pyrolysis.* Advanced Powder Technology **20**, 190–194 (2009).
- [132] Olivier Crottaz, Frank Kubel and Hans Schmid. *Jumping crystals of the spinels  $NiCr_2O_4$  and  $CuCr_2O_4$ .* Journal of Materials Chemistry **7** (1), 143–146 (1997).
- [133] S. Klemme and J. C. van Miltenburg. *Thermodynamic properties of nickel chromite ( $NiCr_2O_4$ ) based on adiabatic calorimetry at low temperatures.* Physics and Chemistry of Minerals **29**, 663–667 (2002).
- [134] Peter J. Wojtowicz. *Theoretical model for tetragonal-to-cubic phase transformations in transition metal spinels.* Physical Review **116** (1), 32–45 (1959).
- [135] H. C. Gupta, Arvind Parashar, V. B. Gupta and B. B. Tripathi. *Lattice vibrations in spinel-type compounds  $CdCr_2S_4$  and  $CdCr_2Se_4$ .* Physica status solidi B **160**, K19–K24 (1990).
- [136] Bong-Hoon Park and Dong-Su Kim. *Thermodynamic properties of  $NiCr_2O_4$ - $NiFe_2O_4$  spinel solid solution.* Bulletin of the Korean Chemical Society **20** (8), 939–942 (1999).
- [137] Geoffrey C. Allen, Josephine A. Jutson and Paul A. Tempest. *Characterization of nickel-chromium-iron spinel type oxides.* Journal of Nuclear Materials **158**, 96–107 (1988).
- [138] A. Rais, A. M. Gismelseed and I. A. Al-Omari. *Cation distribution and magnetic properties of nickel-chromium ferrites  $NiCr_xFe_{2-x}O_4$  ( $0 \leq x \leq 1.4$ ).* Physica Status Solidi B **242** (7), 1497–1503 (2005).
- [139] J. Preudhomme and P. Tarte. *Infrared studies of spinels I: A critical discussion of the actual interpretations.* Spectrochimica Acta **27A**, 961–968 (1971).
- [140] V. S. Stubican and C. Greskovich. *Trivalent and divalent chromium ions in spinels.* Geochimica et Cosmochimica Acta **39**, 875–881 (1975).
- [141] H. L. Pinch and S. B. Berger. *The effects of non-stoichiometry on the magnetic properties of cadmium chromium chalcogenide spinels.* Journal of Physics and Chemistry of Solids **29**, 2091–2099 (1968).
- [142] P. Hosemann, M. Hawley, D. Koury, J. G. Swadener, J. Welch, A. L. Johnson, G. Mori and N. Li. *Characterization of oxide layers grown on D9 austenitic stainless steel in lead bismuth eutectic.* Journal of Nuclear Materials **375**, 323–330 (2008).

VITA

Graduate College  
University of Nevada, Las Vegas

Brian D. Hosterman

Local Address:

4050 Pacific Harbors Dr. Unit 141  
Las Vegas, NV 89121

Degree:

Masters of Science, Physics, 2006  
University of Nevada - Las Vegas, Las Vegas, NV

Bachelor of Science, Physics, 2001  
Denison University, Granville, OH

Dissertation Title: Raman Spectroscopic Study of Solid Solution Spinel Oxides

Thesis Committee:

Chairperson, Dr. John Farley  
Committee Member, Dr. Allen Johnson  
Committee Member, Dr. Michael Pravica  
Committee Member, Dr. Oliver Tschauner  
Graduate Faculty Representative, Dr. rer. nat. Clemens Heske